Material selection and process design for adsorptive CO_2 capture

by

ASHWIN KUMAR RAJAGOPALAN

A thesis submitted in partial fulfillment of the requirements for the degree of

Master of Science

in

CHEMICAL ENGINEERING

Department of Chemical and Materials Engineering

University of Alberta

Abstract

Carbon dioxide capture using adsorption based separation processes has shown promise but has not been exploited to full potential to be implemented on a commercial scale. This thesis examines two key stages in the development of adsorption based carbon dioxide capture processes, namely adsorbent selection and process design.

The first part of the thesis lays the foundation for screening and ranking adsorbents for CO_2 capture using process optimization techniques. Recent interest in carbon dioxide capture has led to the development of hundreds of adsorbents. The selection of the adsorbents and the analysis of their performance for a given process is a challenging task. Usually, the expected performances of these adsorbents are evaluated by inspecting the isotherms and using simple adsorbent metrics (selectivities, working capacities, figures of merit). A process optimization based approach to screen adsorbents for post-combustion CO_2 capture using vacuum swing adsorption is presented. Four different adsorbents (Mg-MOF-74, Zeolite 13X, UTSA-16 and activated carbon) were chosen as test materials and were subjected to process-scale studies on a 4-step PSA cycle with light product pressurization (LPP). The study highlights that most commonly used metrics do not correctly rank the performance of these processes. A systematic study to evaluate the process performance for hypothetical adsorbents to understand the effect of adsorption equilibria is presented. A graphical method to illustrate the non-linearity of CO_2 and N_2 isotherms along with the purity-recovery contours for the hypothetical adsorbents is put forward. It was shown that process performance is more sensitive to the affinity of N_2 than that of CO_2 adsorption capacity.

The second part of the thesis deals with CO_2 capture from an integrated gasification combined cycle (IGCC) based power plants. The IGCC based power plants is attractive as it provides better conditions for CO_2 capture (high operation pressure of $\approx$ 35 bar and CO_2 composition of 30-40 %). Adsorption equilibria for CO_2 on an activated carbon based adsorbent were described

using an empirical model and was used to design pressure swing adsorption cycles to concentrate the CO_2 in excess of 95% with a recovery of 90%.

Keywords: Adsorption, Carbon dioxide capture, Pressure/vacuum swing adsorption, Pre-combustion, Post-combustion, Optimization, Screening, Metrics

எண் பெற்றோருக்கு

To my parents

மகத்தானவர்கள் காணும் மகத்தான கனவுகள் எப்போதுமே நனவாகின்றன

"*Great dreams of great dreamers are always transcended.*"

— Avul Pakir Jainulabdeen Abdul Kalam
(15 October, 1931 - 27 July, 2015)

Acknowledgements

Thanks to Prof. Arvind Rajendran for guiding and providing me the opportunity to pursue my research under his supervision. He has been a great teacher, mentor and source of inspiration. Interacting with him over the years has refined me as a person. It was because of his support and encouragement; I was able to work on different projects without feeling stressed. The innumerable discussions we had during our individual and group meetings have certainly helped me broaden my knowledge on adsorption. Thank you Arvind.

My colleague Adolfo has played a major role in my projects. His expertise on adsorption and the intense discussions we had on breakthrough experiments and methods to screen adsorbents contributed significantly in understanding the basics during the initial stages of the project. And thank you Adolfo for taking me around Denver during our visit to TDA Research Inc.,

I have thoroughly enjoyed the company of my friends and colleagues Ali, Behnam, Johan, Libardo and Parinaz. We worked on many problems in the last couple of years and I have gained immense knowledge from the brainstorming sessions we used to have. The every day 'Tim Hortons' coffee break was the time we would discuss about our cultures. Libardo, my Spanish tutor, colleague and friend was someone whom I could always approach when personal issues were interfering my day to day activities. *Muchas gracias señor.*

Thanks to my former teachers Dr. Anantharaman, Dr. Radhakrishnan, Dr. Bakthavatsalam and Dr. Sundarrajan for their support over the years and for making chemical engineering interesting during my undergraduate years. Dr. Anubha has been an excellent mentor and friend who was always present at the right moment and place to guide me both in my academic and personal life.

I am grateful to Dr. Ambalavanan Jayaraman from TDA Research Inc., for the experimental data that he provided for my pre-combustion CO_2 capture project and inviting me to visit his research facilities in Colorado.

I acknowledge the funding from National Sciences and Engineering Research Council of Canada, National Energy Technology Laboratory, United States Department of Energy Office of Fossil Energy and University of Alberta. I would also like to thank the industrial partner TDA Research Inc.,

Amresh, Arvind, Bhuvanesh, Bharadwaj, Fasil, Hari, Harish and Shri Ram, my friends from NIT Trichy have provided great support over the years. Thank you Ashwath for making the summer of 2015 unforgettable and for the weekly discussions on movies, music and science.

Rohit, Tarun, Geetesh, Abhishek and Rahul have been great roommates and have made my stay in Edmonton enjoyable.

My best friends Gautham, Vivek, Dhamo even though far away have never failed to make me feel comfortable during the last two years.

Finally, I thank my grandparents and parents for their unbroken trust and encouragement for all that I have done till date.

Ashwin Kumar RAJAGOPALAN

Edmonton 2015

Contents

List of Figures

List of Tables

Nomenclature

Greek symbols

α	Selectivity, page 37	[-]
α_{p}	Rate of pressurization/depressurization	[s^{-1}]
β	Working capacity, page 37	[-]
ΔH	Heat of adsorption	[J mol^{-1}]
ϵ	Bed voidage	[-]
ϵ_{MBE}	Mass balance error	[%]
ϵ_{p}	Particle voidage	[-]
η	Compression/evacuation efficiency	[-]
γ	Adiabatic constant, page 49	[-]
γ_i	Figure of merit, page 37	
λ	Penalty function	[-]
μ	Fluid viscosity	[kg m^{-1} s^{-1}]
ϕ	Flux limiter function	
π	Spreading pressure	
ψ	Penalty function	[-]
ρ	Density	[kg m^{-3}]
θ	Working capacity ratio, page 55	[-]

Roman symbols

A	Cross-sectional area	[m^2]
b	Adsorption equilibrium constant for site 1	[Pa^{-1}]
c	Fluid phase concentration	[mol m^3]
C_p	Specific heat capacity	[J kg^{-1} K^{-1}]
d	Adsorption equilibrium constant for site 2	[Pa^{-1}]
D_m	Molecular diffusivity	[m^2 s^{-1}]
En	Energy	[kWh (tonne CO_2 cap.)$^{-1}$]
f	Flux	
h	Heat transfer coefficient	[J m^{-2} K^{-1} s^{-1}]
K	Adsorption equilibrium constant in Freundlich isotherm	[mol kg^{-1} $Pa^{-\frac{1}{n}}$]
k	Adsorption equilibrium constant in Sips isotherm	[Pa^{-1}]
K_w	Effective wall thermal conductivity	[J m^{-1} K^{-1} s^{-1}]
K_z	Effective gas thermal conductivity	[J m^{-1} K^{-1} s^{-1}]
L	Length of the column	[m]
n_i	Number of moles	[mol]
n_{comp}	Number of components	
P	Pressure	[Pa]
p	Partial pressure of a gas	[Pa]
P^0	Equilibrium gas-phase spreading pressure	
Pr	Productivity	[mol CO_2 (m^3 ads. s)$^{-1}$]
Pu	Purity	[%]
q	Solid phase concentration	[mol m^{-3}]
R	Universal gas constant	[Pa m^3 mol^{-1} K^{-1}]
r	Solution smoothness	
Re	Recovery	[%]
s	Heterogeneity parameter in Sips isotherm	[-]

T	Temperature	[K]
t	Time	[m^s]
V	Volume	
v	Interstitial velocity	[m s^{-1}]
x	Solid phase mole fraction	[-]
y	Fluid phase mole fraction	[-]
r	Radius of the column	[m]

Abbreviations, subscripts and superscripts

*	Equilibrium state
1	Low pressure state, page 18
2	High pressure state, page 18
A	Ackley, page 37
a	Ambient
ADS	Adsorption step
b	First site in DSL isotherm model
BLO	Blowdown step
C	Competitive, page 37
CnBLO	Counter-current blowdown step
CoBLO	Co-current blowdown step
d	Second site in DSL isotherm model
EVAC	Evacuation step
feed	Feed condition
g	Gas, page 17
H	Henry, page 37
H	High

i	Component
in	Inner, page 17
INT	Intermediate
L	Low
LPP	Light product pressurization step
N	Notaro, page 37
out	Outer, page 17
P	Pure, page 37
p	Particle, page 17
PREQ_D	Pressure equalization donor step
PREQ_R	Pressure equalization receiver step
PRESS	Feed pressurization step
PUR	Purge step
pur	Purge
ref	Reference
s	Saturation, page 14
s	Solid adsorbent, page 17
step	Step
W	Wiersum, page 37
w	Wall
Y	Yang, page 37

Acronyms

CCS	Carbon capture and storage
CSS	Cyclic steady state
DCB	Dynamic column breakthrough

DSL	Dual site Langmuir
FOM	Figure of merit
FVM	Finite volume method
GHG	Greenhouse gas
IAST	Ideal adsorbed solution theory
IGCC	Integrated gasification combined cycle
LDF	Linear driving force
LPP	Light product pressurization
MOF	Metal organic framework
ODE	Ordinary differential equation
PDE	Partial differential equation
PE	Pressure equalization
PSA	Pressure swing adsorption
SSL	Single site Langmuir
SSL	Upwind difference scheme
TSA	Temperature swing adsorption
TVD	Total variation diminishing
VSA	Vacuum swing adsorption
WCR	Working capacity ratio

Chapter 1

Introduction

1.1 General introduction

At the turn of the 21st century, the global CO_2 concentration was increasing in an alarming rate. The CO_2 level was inching closer to the 400 parts per million (ppm) mark which would be the highest recorded atmospheric CO_2 levels in the last 800,000 years [1, 2]. The steam engine was one of the most important inventions that steered the entire globe towards an industrial revolution. With the booming industrial sector, the consumption of fossil fuels especially coal increased and led to the addition of significant amount of greenhouse gases (GHGs) into the atmosphere. As shown in Figure 1.1, at the beginning of the industrial revolution in the 1700s, the average CO_2 concentration was $\approx$ 260 ppm and by late 2014, the global average was 400 ppm, which was a 50% increase in the span of 300 years.

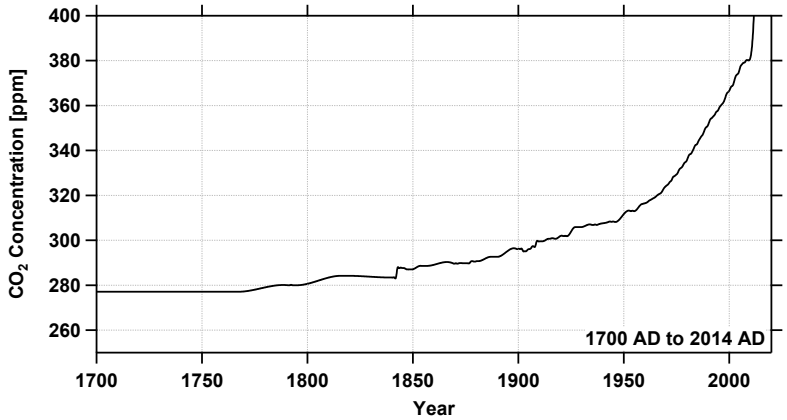

Figure 1.1: Global atmospheric concentrations of CO_2 over the last 300 years. Source: United States Environmental Protection Agency [1, 2].

A direct correlation between the CO_2 and the global temperature rise has been observed. Since

1901, the global average temperature has increased on an average by 0.08°C every decade [4]. The major sources of GHG emissions include power generation; industrial processes such as production of oil, iron, steel, cement; and emissions from cars, airplanes, ships to name a few. The majority ($\approx 80\%$) of the greenhouse emissions came from Asia, Europe and United States [5, 6]. The energy sector (power generation and fuel used to power vehicles) contributed to nearly 70% of the total greenhouse gas emissions in 2010 and currently, $\approx 45\%$ of the electricity demands in United States is met by coal-based power plants. Due to the widespread acceptance that anthropogenic gases, mainly CO_2 is the prime cause of global warming, and coal-based power plants being the chief source of CO_2, carbon capture and storage (CCS) has been taken seriously by nations across the world. Studies have shown that even if the entire GHG emissions were to cease completely, the global climate patterns have already been affected severely that it would take years to stabilize the climate change. In the 16th session of Conference of the Parties (COP16) to the United Nations Framework Convention on Climate Change (UNFCC), it was agreed upon that countries around the world would take sincere efforts to keep the global average temperature rise to less than 2°C. Carbon dioxide from gas streams in various industrial process have been captured over the years, but in most of the cases the CO_2 has been vented out to the atmosphere. Capturing CO_2 from fossil fuel based power plants and storing it is a challenging task due to the stringent sequestration targets set by the U.S. Department of Energy and other regulatory bodies. Significant developments in the field of carbon capture over the last few years have resulted in development of new processes and materials to capture CO_2. The global CCS institute has identified 16 carbon capture and storage (CCS) projects around the world currently operational or in the execution phase. Four of these projects are based in Canada and these CCS units are expected to capture 5 million tonnes per annum (MTPA) once fully operational [7]. In October 2014, SaskPower opened the first commercial scale, coal-fired power plant equipped with a carbon capture and storage technology in Saskatchewan, Canada. The power plant is expected to product 110 MW of power and capture 1 million tonnes of CO_2 every year which will be transported to oil fields by pipelines for enhanced oil recovery (EOR). Based on these developments it is clear that global warming is indeed an important issue that needs to be addressed in near future and there is a huge scope to understand and improve the existing technologies to capture CO_2 from power plants, the largest contributor of GHG emissions.

1.2 Carbon capture from coal fired power plants

Carbon capture technologies available currently have the potential to capture around 85-90% CO_2 processed in a power plant. The captured CO_2 would then have to be compressed and transported for storage. A power-plant equipped with a CCS system would require 10-40% more energy than a plant without a CCS system to capture the CO_2. Existing CO_2 capture

technologies can be broadly classified under three categories post-combustion, pre-combustion and oxy-combustion and are shown in Figure 1.2. These technologies can be chosen based on the concentration, pressure and temperature of the CO_2 gas stream. A post-combustion capture system can be used to capture CO_2 from a flue gas stream after the complete combustion of the fossil fuel. The flue gas stream typically is a dilute stream with CO_2 concentrations close to 3-15% and available at near atmospheric conditions. This is a mature technology which has been showing promising results for absorption and adsorption based separation systems. Unlike post-combustion capture system where a CCS unit can be added downstream in existing power plants, for a pre-combustion CO_2 capture, the coal-based fuel has to undergo several conversion steps which adds to the cost for separation. But, the higher CO_2 concentration ($\approx$ 15-60%) and feed pressure ($\geq$ 20 bar) make the separation easier. Pre-combustion capture system can be used at power plants employing an integrated gasification combined cycle (IGCC). Among the carbon capture technologies, post-combustion and pre-combustion capture are economically feasible under certain operating conditions, while oxy-combustion is currently in the demonstration phase [3].

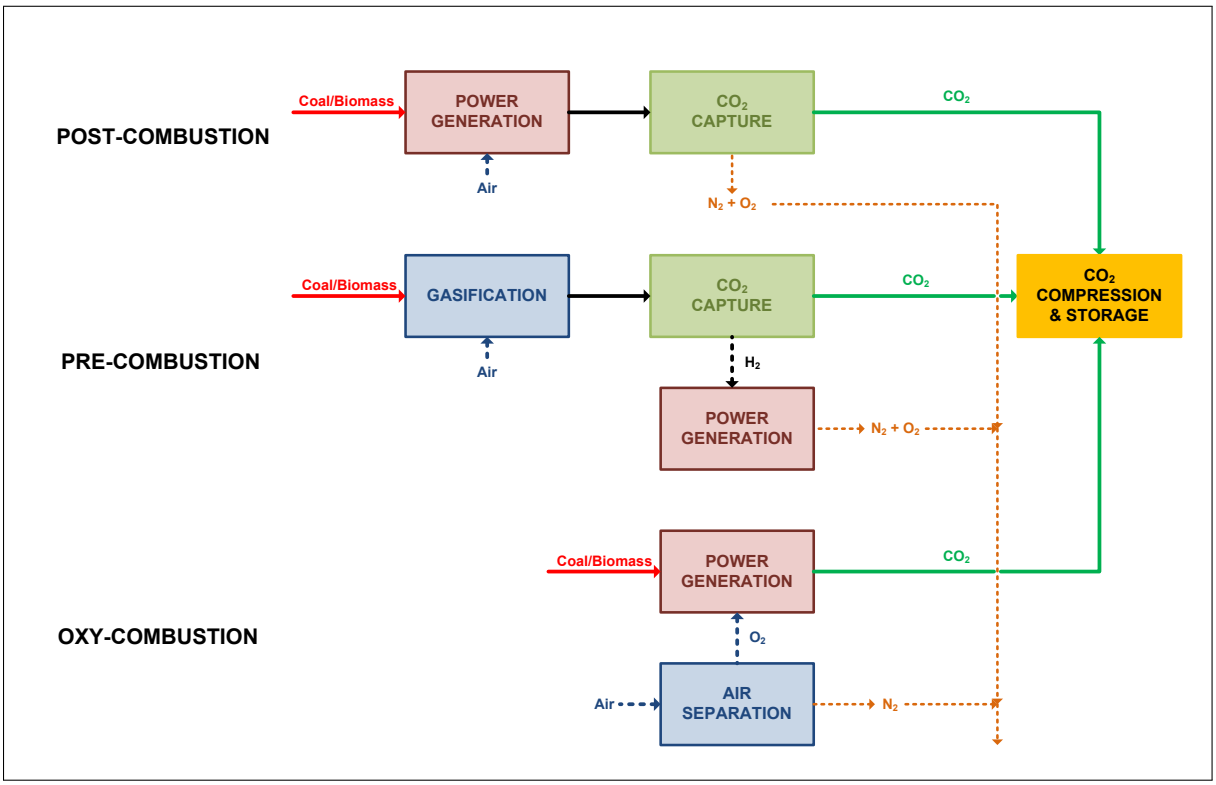

Figure 1.2: Existing CO_2 capture technologies (Adapted from [3])

The separation CO_2 from a gas stream of N_2, H_2 or other impurities can be carried out using solvents, cryogenic separation, solid sorbents or membranes. The choice of the technology is decided by the process conditions under which they operate. Chemical solvents are used to

remove CO_2 from syngas at partial pressures less than 15 bar. The most commonly used solvents being monoethanolamine (MEA) tertiary amine methyldiethanolamine (MDEA). While physical solvent processes are used to capture CO_2 available at a higher partial pressure. The physical solvents have the ability to achieve a higher solubility for acidic gases, without corrosion problems or adding extra heat for stripping the gases [8]. Adsorption based processes involve the use of solid sorbents which can be used in a wide of operating conditions and process configurations. Adsorption based processes have been used over the years for air separation, drying, and hydrogen purification [9, 10]. These processes are cyclic in nature and they have two constitutive steps, adsorption and desorption. In the adsorption step, the most selective species is preferentially removed from the feed gas stream. While in desorption, the sorbent is regenerated by utilizing the differences in affinity at a lower and higher temperature or pressure. Depending on the process configuration useful products can be obtained in both the adsorption and desorption steps. For a sorbent to be suitable for a CO_2 capture process, the sorbent must posses a high CO_2 selectivity, CO_2 capacity at the feed conditions, hydrophobic characterstics and fast adsorption/desorption kinetics [11]. CO_2 capture using adsorption based separation processes can be either pressure/vacuum swing adsorption (P/VSA) or temperature swing adsorption (TSA). PSA based capture technology enjoys faster cycle times when compared to a TSA based capture technology. Zeolites and carbonaceous materials have been explored at different process conditions and configurations. Novel materials like the metal organic frameworks (MOFs) and amine impregnated sorbents have caught recent attention for carbon capture. Various research groups forecast CO_2 using membranes would be extremely beneficial in carbon capture due to the absence of phase changes unlike solvent or sorbent based separation, steady-state operation and ease in scaling up the process [12, 13].

Chemical-looping combustion (CLC) is a process to separate CO_2 using metal oxides [14]. In a typical CLC process, the CO_2 is separated from other flue gas components. The process uses two different reactors, namely, air and fuel reactor. The fuel gas, liquids or solids, such as natural gas, heavy oils is introduced into the fuel reactor with a metal oxide material. The metal oxide is reduced due to the reaction between the fuel gas and the metal oxide material and produces a gas stream composed of CO_2 and H_2O. In the air reactor, the metal oxide is regenerated and produces a flue gas composed primarily of N_2. The major advantage of using a CLC technology for carbon dioxide capture is that, CO_2 is not diluted in a stream of N_2 and hence the need for a separation technology is eliminated and avoids large energy penalties associated with the CO_2 capture. Various CLC based operational combustors are presented have shown promise [13]. CLC has shown to be capable of capturing 100% CO_2 using gaseous fuels, while for solid fuels, the technology is still immature to be implemented in a large scale.

Even with the recent advancements in the field of carbon capture, the interplay between the capture materials and CO_2 capture processes is not well understood. As a result of this short-

coming, a considerable portion of this thesis is devoted to the understanding of the behavior of carbon capture materials on a process scale, while the other is devoted to the designing of CO_2 capture processes based on adsorption techniques that would meet sequestration targets.

1.3 Adsorption based CO_2 capture

Very few adsorption based separation processes have reached commercial stage for CO_2 capture. The major challenge in carbon capture using adsorption processes is the scale of the capture process. The inherent problem stems from the fact that working capacity of CO_2 on the adsorbent represented as Δq in Figure 1.3, defined as the amount of processed CO_2 by a pressure/temperature swing is generally low for the operating pressures or temperatures. Hence, the process requires large quantities of adsorbent. It has been shown that for a 1GW coal fired power plant emitting 800 tons of CO_2/h, at least 16,000 tons of adsorbents materials is necessary corresponding to a volume of $\approx$ 23,000 m^3 for the adsorption units [13]. The working capacity and the amount of adsorbent used for the capture process would ultimately determine the cost, volume of the adsorption units and the energy penalty.

As shown in Figure 1.3, adsorption based separation processes can be carried out using a pressure or temperature swing. In a PSA based capture technology, the heavy component (CO_2 in the current case) is captured at a high pressure (P_{ADS}) because at this condition, the adsorbent is highly selective towards the heavy component and has a higher adsorption capacity. The less selective or less strongly adsorbing component (light component) is rejected out from column in the adsorption step. In order to regenerate the adsorbent, the differences in the affinity of the adsorbent towards the adsorbate at the high and low pressure is utilized and typically, at a pressure (P_{DES}) lower than the feed pressure, the affinity of a gaseous species towards the adsorbent is low. The lower affinity weakens the attractive forces between the adsorbent and the adsorbate, and depending on the light component affinity, a concentrated heavy product stream is obtained. In a TSA based capture technology, the heavy component is capture at a low temperature (T_{ADS}) because of the higher affinity on the adsorbent and to desorb the adsorbed species, the temperature (T_{ADS}) is increased and the differences in the equilibrium capacities at different temperatures is exploited. In Figure 1.3, Δq_{PSA} and Δq_{TSA} represents the difference in the solid phase concentrations by doing a pressure swing or temperature swing, respectively. The adsorption process is cyclic in nature due to the presence of two steps at different process conditions. The mass transfer operation driven by the adsorbent selectivity/affinity towards a particular can be driven by thermodynamic or kinetic effects. When the affinity for the components in the gas mixture at equilibrium is different for the two states between which an adsorption process operates, thermodynamics is rate controlling. While, when there exists a significant difference in the adsorption/desorption rates for the different components, kinetics

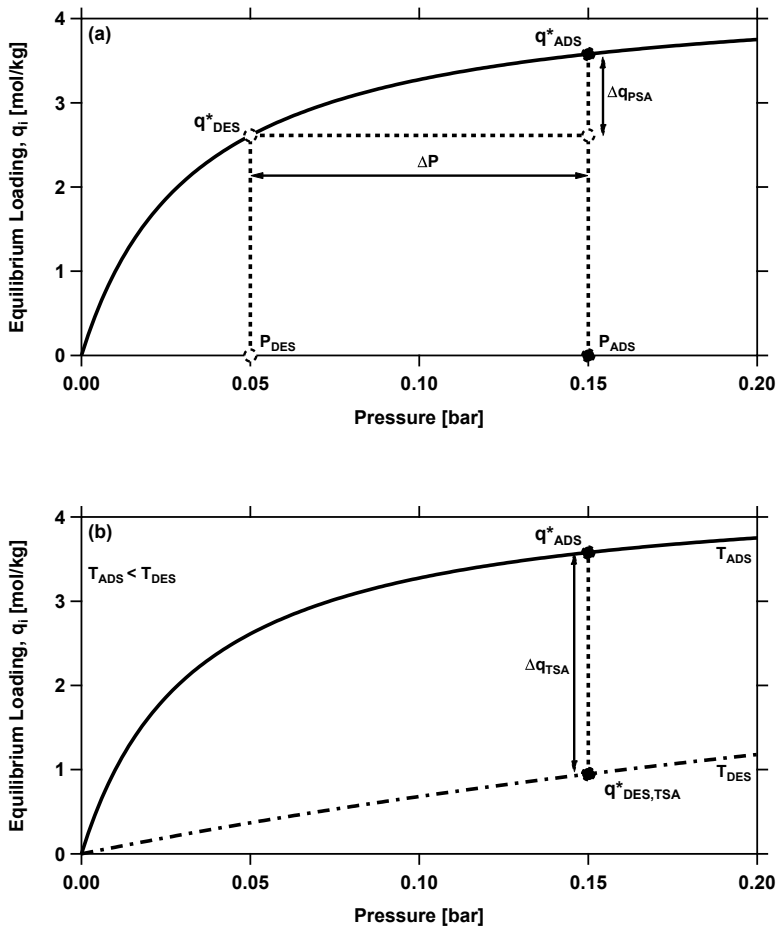

Figure 1.3: Description of (a) pressure swing adsorption (PSA) and (b) temperature swing adsorption (TSA).

is rate controlling. The pressure swing adsorption process in which the desorption pressure is close to atmospheric conditions is referred to as a PSA process in this work and the processes in which the desorption step occurs at sub-atmospheric conditions are referred to as a vacuum swing adsorption (VSA) process.

The major advantage of a P/VSA over a TSA process is that the pressure can be changed much more rapidly than temperature. Hence, the P/VSA cycles generally have shorter cycle times and results in a larger productivity than TSA cycle, i.e., amount of feed processed in a given time is more from a P/VSA cycle than a TSA cycle. If the one of the components have a very high adsorption affinity on the adsorbent, desorbing becomes a challenging task as the process has to be operated at near vacuum conditions to desorb the adsorbed species [10]. For the above mentioned reasons a P/VSA process was chosen in this work, and the performances

were evaluated for two different carbon capture technologies, namely pre-combustion and post-combustion carbon capture. The P/VSA processes operate under transient conditions, while other separation processes like distillation, absorption, etc., operate at steady-state conditions. which adds complexity to an adsorption based separation process. In order to evaluate the process performance mathematically using the constitutive transport equations, coupled non-linear partial differential equations have to be solved over the space and time domain, instead of ordinary differential equations, which are solved only over the space domain for a steady-state process. Despite the complexities of the process, PSA processes have been in commercial use for H_2 recovery from fuel gas and air separation [15, 16].

1.4 Adsorbents for CO_2 capture

Selective adsorption of CO_2 on solid adsorbents via adsorption based separation processes are well known [9, 17]. The adsorption mechanism on these adsorbents are either through weak physical adsorption or strong chemical interactions. Classical materials like Zeolite 13X, activated carbon, hydrotalcites and supported amines are used extensively for carbon capture, while a new class of novel material, the metal organic framework (MOF) is currently emerging. Adsorption affinity, selectivity towards the CO_2, fast adsorption/desorption kinetics determine the efficacy of an adsorbent towards carbon capture. Depending on the operation pressure, temperature, concentration of CO_2, and tolerance towards moisture and impurities, the adsorbent can be used for post- or pre-combustion capture. Merits and demerits of some of the adsorbents used in this work are discussed in the following sub-sections.

1.4.1 Zeolites

Zeolite are porous crystalline aluminosilicates which consists of a periodic arrangement of SiO_4 and AlO_4 tetrahedra joined together through shared oxygen atoms. The Zeolite structure is an open crystal lattice with pores into which molecules can penetrate depending on their molecular size. Zeolite falls under the physical adsorption based class of materials and over 170 different Zeolites are known to have been synthesized [18]. Among the different types of Zeolites, namely X, Y, L and ZSM, Zeolite 13X was reported to have the highest CO_2 capacity [19] and it is the current benchmark adsorbent for post-combustion CO_2 capture. For Zeolite 13X, the CO_2 uptake is drastically reduced in the presence of moisture in the feed gas and the increase in CO_2 adsorption capacity beyond atmospheric conditions is generally lower than what is observed at sub-atmospheric conditions, which limits the application of Zeolite 13X to processes with a dry flue gas stream at atmospheric conditions.

1.4.2 Activated carbon

Activated carbon is a well studied class of adsorbents which has been used over the years for gas separation and purification. Activated carbon can be produced from coal, petroleum, biomass, etc., and due to the wide availability of carbonaceous sources for the synthesis of activated carbon, they can be produced commercially at a very low-cost [20]. Depending on the source for the synthesis of activated carbon, the pore structure and hence the properties might differ between the different activated carbon based adsorbents. The equilibrium measurements on activated carbon at atmospheric conditions indicate a low CO_2 adsorption capacity, while at higher pressures the CO_2 adsorption capacity of activated carbon can be higher than zeolites. Most of the activated carbons are hydrophobic in nature which aids in processing flue gas streams with moisture. Unlike Zeolite 13X, the activated carbon can be used for capturing CO_2 from a wet flue gas stream over a wide range of pressures, and due to these advantages an activated carbon based adsorbent is used for a pre-combustion CO_2 capture system presented in this thesis.

1.4.3 Metal-organic frameworks

Metal-organic frameworks (MOFs) is an emerging class of crystalline adsorbent material and recently they been investigated for capturing CO_2. The first MOF materials were synthesized by Yaghi and co-workers [21] and they reported a large pore volume and surface area for these adsorbents. The MOF materials are hydrophilic in nature, hence the MOFs show a strong affinity towards and in cases when the affinity is very strong, defects are generated in the crytal lattice framework of the MOF material. The MOF materials are found to have strong affinity towards CO_2 and are accompanied by a CO_2 very high adsorption capacity. For most of the MOFs at low pressures, a small change in pressure results in a large change in the adsorption capacity. Few MOFs have been reported in the literature which show interesting behavior at low pressures. MOFs like MOF-177 [22], at low pressures show small changes in the adsorption capacity by a small change in the pressures, but there exists a critical pressure, beyond which there is a sharp increase in the adsorption capacity, which then follows a Langmuir isotherm like behavior. The initial observations with MOFs have caught attention of both chemists and process engineers to modify and design materials and processes which could eventually utilize the potential of these materials.

The three different classes of adsorbents discussed above are used for two different capture technologies presented in this thesis. Due to the ability of activated carbon to operate over a wide range of pressure, a pre-combustion CO_2 capture process is designed with a surface modified activated carbon as a solid sorbent in chapter 5. Zeolite 13X, being the most widely studied solid

adsorbent for post-combustion CO_2 capture, it is chosen as the base adsorbent in the studies presented in chapter 3 and 4. The unavailability of prior performance analysis for MOFs led to selection of two different materials which are compared with Zeolite 13X based on their ability to reach the targets with the least energy consumption.

1.5 Thesis objectives and outline

The central focus of this thesis is to screen and rank adsorbent materials and design processes for CO_2 capture that would meet the sequestration targets set by various regulatory bodies. Pressure swing adsorption (PSA) based processes have caught recent interest and have shown promising results for CO_2 capture. Two capture technologies, namely pre-combustion and post-combustion CO_2 processes are studied extensively in this work. Post-combustion CO_2 processes have been studied in detail over the last few years. This has led to the development of new adsorbent materials that differ in adsorption capacities, stability and tolerance towards moisture. The selection of an adsorbent is crucial in process design and selecting or discarding an adsorbent has to be undertaken cautiously. The first part of the thesis provides a new approach to screen adsorbents using full-scale process optimization studies. Owing to the fact that pre-combustion CO_2 capture is a less mature technology, different process cycle configurations are developed and their merits and demerits are evaluated.

The key points addressed in this work are:

- To revisit simple adsorbent screening metrics and answer a key question as to whether these metrics can reliably be used to screen adsorbents.
- To provide directions for chemists to synthesize adsorbent materials with desired isotherms and properties that would consume least energy meeting the CO_2 capture sequestration targets.
- To develop cycles for a pre-combustion CO_2 capture process that satisfies DOE targets for CO_2 purity and recovery using an activated carbon based adsorbent.

Chapter 2 deals with modeling and optimization of a PSA cycle. Different empirical models that are used to define single and competitive adsorption equilibria on adsorbents are discussed. A detailed description and validation of a non-isothermal, non-isobaric mathematical model for a PSA cycle is presented. A detailed workflow of the process optimization based on genetic algorithm, which would form the core of Chapters 3 and 4 is put forth.

Chapter 3 provides a key insight into adsorbent screening using adsorbent metrics. The efficacy of adsorbent metrics are evaluated by performing process optimization studies on four different materials, two metal organic frameworks (MOFs), namely, Mg-MOF-74 and UTSA-16; Zeolite

13X, the current benchmark for CO_2 capture; and an activated carbon. The purity-recovery and energy-productivity pareto curves from rigorous optimization routines are used to rank adsorbents and obtain operating conditions that maximize their performances.

Chapter 4 provides a detailed case study on providing directions to chemists towards synthesizing new adsorbents with favorable isotherms that could achieve the purity-recovery targets with the least energy consumption for the PSA cycle configuration considered. A graphical approach (referred as non-linearity plot) to differentiate adsorbents based on the non-linearity of the isotherms is proposed. Hypothetical adsorbents are subjected to a purity-recovery and energy-productivity optimization to assess the effect of adsorbent selectivity and shape of isotherms. The non-linearity plot would be a handy tool for screening adsorbents, which could be used to do a quick check on the adsorbent efficacy towards carbon capture.

Chapter 5 addresses the process design for pre-combustion CO_2 using TDA-AMS-19, an activated carbon based adsorbent. Five different PSA cycle configurations, with pressure equalization steps and steam purge are evaluated to meet 95-90% purity-recovery targets set by United States Department of Energy (U. S. DoE). Effect of gas flow direction and number of pressure equalization steps in the process are studied by performing process simulations for a feed gas of 40% CO_2 and 60% H_2.

Chapter 6 discusses the conclusions of this work and provides recommendations and outlook for future work.

Chapter 2

Modeling and process optimization of a pressure swing adsorption (PSA) cycle

2.1 Introduction

The design and process optimization of pressure/vacuum swing adsorption cycles (P/VSA) studied in this work, required detailed full-cycle models, using fast and robust numerical techniques. The model used for the process design must be capable of handling the complexities associated with a typical P/VSA process which arises from the wave dynamics; the pressure, temperature and concentration gradients along the adsorption column. The key stages in the design of an adsorption based separation process system involves the accurately describing the equilibrium data in the solid adsorbent using empirical isotherm models, accounting for the mass and heat transfer effects using transport equations with the necessary boundary conditions for the constitutive steps of the process and framing the optimization problem to maximize the performance of the process. In this chapter the above mentioned stages in the design process is presented along with a detailed analysis of the different isotherm models and numerical techniques based on the volume finite method.

2.2 Modeling of equilibria for an adsorption process

Adsorption equilibrium data is a key requirement for the analysis and design of an adsorption process. Description of adsorption equilibrium involves fitting the experimental equilibrium measurements for a given adsorbent obtained at different temperatures over a wide range of pressure. The accurate description of adsorption equilibria gives us an insight on the adsorption

capacities of a given adsorbent for different components in a gas mixture. Different models have been proposed in the literature over the years to describe the equilibrium measurements [9].

2.2.1 Single component adsorption equilibria

Langmuir isotherm model

The simplest model to describe the adsorption equilibrium is the Langmuir model [23]. The Langmuir model assumes that molecules are adsorbed at a fixed number of sites with identical energies. The assumption also states that each site accommodates only a single molecule and the interaction between molecules adsorbed on neighboring sites are absent. The Langmuir model is simple kinetic model which is derived considering the exchange of molecules between the solid and the fluid phases. The Langmuir isotherm model is given as follows:

$$\boldsymbol{q_i^* = \frac{q_{s,i} b_i p_i}{1 + b_i p_i}} \tag{2.1}$$

where, q_i^* is the equilibrium solid phase concentration at a given temperature and pressure, $q_{s,i}$ is the saturation solid phase concentration of the given component i and b_i is the adsorption equilibrium constant which follows an Arrhenius type temperature dependence given by

$$b_i = b_{0,i} e^{-\frac{\Delta H_i}{RT}} \tag{2.2}$$

where, ΔH_i is the heat of adsorption, which is independent of the coverage in the adsorbent as the model assumes an adsorbent with identical sites without interactions between neighboring sites.

Dual-site Langmuir isotherm model

The major drawback of Langmuir model comes in from the assumption of a homogeneous surface, i.e., all the sites have identical energies. The simple Langmuir model is modified to accommodate sites with two different energies to give rise to the dual-site Langmuir (DSL) isotherm model. The dual-site Langmuir model has a higher degree of heterogeneity when compared to a simple Langmuir model [24]. The single component dual-site Langmuir model is given by the following relation:

$$\boldsymbol{q_i^* = \frac{q_{sb,i} b_i p_i}{1 + b_i p_i} + \frac{q_{sd,i} d_i p_i}{1 + d_i p_i}} \tag{2.3}$$

where, $q_{\mathrm{sb},i}$ and $q_{\mathrm{sd},i}$ are the saturation solid phase concentration of the given component i for the two energetically different sites, b and d. b_i and d_i are the adsorption equilibrium constants which follows an Arrhenius type temperature dependence given by

$$b_i = b_{0,i} e^{-\frac{\Delta H_{b,i}}{RT}} \tag{2.4a}$$

$$d_i = d_{0,i} e^{-\frac{\Delta H_{d,i}}{RT}} \tag{2.4b}$$

The model assumes that the site b has a higher affinity than the site d. The total saturation capacity and the mean adsorption equilibrium constants are given by the following equations

$$q_{\mathrm{s},i} = q_{\mathrm{sb},i} + q_{\mathrm{sd},i} \tag{2.5a}$$

$$bd_i = \frac{q_{\mathrm{sb},i} b_i + q_{\mathrm{sd},i} d_i}{q_{\mathrm{sb},i} + q_{\mathrm{sd},i}} \tag{2.5b}$$

Sips isotherm model

Apart from the Langmuir isotherm model, the other frequently used model is the Freundlich isotherm model [25]. The Freundlich isotherm model assumes that the surface is heterogeneous and the sites with identical energies form a patch and patches with different energies form the entire surface of an adsorbent. Interaction between the different patches are assumed to be absent. The model also assumes that the Langmuir model is applicable to describe the local equilibria for each patch. The Freundlich isotherm model is given as

$$\boldsymbol{q_i^* = K p^{\frac{1}{n}}} \tag{2.6}$$

where, K and n are temperature dependent parameters in the isotherm model. The parameter n quantifies the isotherm sharpness. The isotherm model reduces to a simple linear isotherm when the parameter n is unity and as the value of n increases, the isotherm deviates from the simple linear isotherm.

According to the Freundlich isotherm given by the equation 2.6, the amount of gas adsorbed by the solid adsorbent, q_i^* increases indefinitely with the pressure. This would mean that the solid adsorbent has infinitely many sites for adsorbing the gas, but physically for very high pressures, the adsorbent surface is saturated with the gas. Hence, the Freundlich isotherm model is modified

to account for the saturation of the adsorbent at high pressures such that the equilibrium loading asymptotically tends to the saturation solid phase concentration, $q_{s,i}$. The modified Freundlich isotherm, referred to as the Langmuir-Freundlich or Sips isotherm model [26] is given by

$$\boldsymbol{q_i^* = \frac{q_{s,i}(k_i p_i)^{s_i}}{1 + (k_i p_i)^{s_i}}} \tag{2.7}$$

$$q_{s,i} = \omega_i e^{-\frac{\varphi_i}{RT}} \tag{2.8a}$$

$$k_i = \theta_i e^{-\frac{\phi_i}{RT}} \tag{2.8b}$$

$$s_i = s_{1,i}\, atan(s_{2,i}(T - T_{ref}) + s_{ref,i}) \tag{2.8c}$$

where, $q_{s,i}$ is the temperature dependent saturation solid phase concentration, k_i is the adsorption equilibrium constant and s_i is a parameter which describes the homogeneity of the surface. The parameter s_i can take values between 0 and 1. As the parameter s_i approaches unity, the Sips isotherm model takes the form of a simple Langmuir isotherm model.

2.2.2 Description of competitive adsorption equilibria

Often an adsorption process involves more than a single component, and therefore competition between the mixture species needs to be accounted for in the design of adsorption separation process. To accurately describe the multi-component adsorption equilibria, equilibrium data measurements needs to be conducted using mixtures. When the multi-component equilibrium measurements are not available, the adsorption equilibria is described using the IAS theory [27–29] or the simpler extensions of single-component models.

Ideal adsorbed solution theory

The IAS theory is analogous to Raoult's law for vapor-liquid equilibrium given by

$$P_i = P_i^0\,(\pi_i)\, x_i \tag{2.9}$$

where, π_i and x_i are the spreading pressure and mole fraction of component i in the adsorbed phase, respectively. The mole fraction of component i in the adsorbed phase is defined as

$$x_i = \frac{q_i}{\sum_{i=1}^{n_{comp}} q_i} \tag{2.10}$$

At equilibrium conditions, the reduced pressures for each individual component are the same. The spreading pressure for each component is given as follows:

$$\pi_i^* = \frac{\pi_i}{RT} = \int_0^{P_i^0} \frac{n_i^0\left(P\right)}{P} dP \tag{2.11a}$$

$$\pi_1^* = \pi_2^* = \pi_3^* = ... = \pi^* \tag{2.11b}$$

where, n_i^0 is the pure component equilibrium adsorption capacity and P_i^0 is the equilibrium gas-phase spreading pressure corresponding to the spreading pressure of the mixture. An ideal adsorbed solution which does not have an enthalpy or area change upon mixing is assumed. The total amount adsorbed is calculated as

$$\frac{1}{n_t} = \sum_{i=1}^{n_{\text{comp}}} \left[\frac{x_i}{n_i^0\left(P_i^0\right)}\right] \tag{2.12a}$$

$$\sum_{i=1}^{n_{\text{comp}}} x_i = 1 \tag{2.12b}$$

The unknowns in this model are P_i^0, π, n_i^0, x_i and q_i; and the model equations cannot be solved analytically for most of the pure component isotherm models. Hence, for integrating equation 2.11a and solving equations 2.9 - 2.12 simultaneously, iterative methods need to be employed. The determination of multi-component adsorption equilibria using IAST method is not straightforward, and therefore very often, extensions of the isotherm models are used to describe competitive adsorption.

Extended single-component isotherm model

The extended isotherm models for multi-component systems corresponding to the single component isotherm models discussed in section 2.2.1 are given as follows

- **Extended Langmuir isotherm model**

$$q_i^* = \frac{q_{\text{s},i} b_i p_i}{1 + \sum\limits_{i=1}^{n_{\text{comp}}} b_i p_i} \tag{2.13}$$

- **Extended dual-site Langmuir model**

$$q_i^* = \frac{q_{\text{sb},i} b_i p_i}{1 + \sum\limits_{i=1}^{n_{\text{comp}}} b_i p_i} + \frac{q_{\text{sd},i} d_i p_i}{1 + \sum\limits_{i=1}^{n_{\text{comp}}} d_i p_i} \tag{2.14}$$

- **Extended Sips isotherm model**

$$q_i^* = \frac{q_{s,i}(k_i p_i)^{s_i}}{1 + \sum_{i=1}^{n_{comp}} (k_i p_i)^{s_i}} \tag{2.15}$$

In the equations 2.13 - 2.15, as a result of the additional term present in the denominator when compared to the single component isotherm model described in section 2.2.1, the solid phase concentration decreases due to the competition between the n_{comp} species in the system being considered. The assumptions associated with the extended single component models are the same as the corresponding single component models. These assumptions cannot be applied to practical systems and cannot accurately capture the competitive effects in a multi-component adsorption system. Nevertheless, this approach of using the extended single component model is computationally less intensive and for the systems discussed in this work, it has been assumed that the extensions of the single-component isotherm models can reliably predict the multi-component behavior for the given conditions.

2.3 Process design of a pressure swing adsorption (PSA) cycle

2.3.1 Model equations

A column packed with solid adsorbent of length L shown in Figure 2.2 was used in this study. The adsorption dynamics in the column was described using a one-dimensional mathematical model. The mass and energy balance equations were written considering the following assumptions:

- Axially dispersed plug flow model is used to represent the gas flow through the fixed-bed
- The gas phase is described by the ideal gas law
- The mass transfer resistance is assumed to be controlled by macropore diffusion and it is described by the linear driving force (LDF) model
- There is no concentration, temperature and pressure gradient in the radial direction
- The system is considered to be adiabatic
- The adsorbent properties and bed voidage are uniform across the column
- The pressure drop through the packed bed is described by the Darcys law

Component mass balance

$$\frac{\partial y_i}{\partial t} + \frac{y_i}{T}\frac{\partial P}{\partial t} - \frac{y_i}{P}\frac{\partial T}{\partial t} = \frac{T}{P}D_{\mathrm{L}}\frac{\partial}{\partial z}\left(\frac{P}{T}\frac{\partial y_i}{\partial z}\right) - \frac{T}{P}\frac{\partial}{\partial z}\left(\frac{y_i P}{T}v\right) - \frac{RT}{P}\frac{1-\epsilon}{\epsilon}\frac{\partial q_i}{\partial t} \tag{2.16}$$

Overall mass balance

$$\frac{1}{P}\frac{\partial P}{\partial t} - \frac{1}{T}\frac{\partial T}{\partial t} = -\frac{T}{P}\frac{\partial}{\partial z}\left(\frac{P}{T}v\right) - \frac{RT}{P}\frac{1-\epsilon}{\epsilon}\sum_{i=1}^{n_{\mathrm{comp}}}\frac{\partial q_i}{\partial t} \tag{2.17}$$

Solid phase mass transfer rate

$$\frac{\partial q_i}{\partial t} = \alpha_i\left(q_i^* - q_i\right) \tag{2.18}$$

Column energy balance

$$\left[\frac{1-\epsilon}{\epsilon}\left(\rho_{\mathrm{s}}C_{\mathrm{p,s}} + C_{\mathrm{p,a}}\sum_{i=1}^{n_{\mathrm{comp}}}q_i\right)\right]\frac{\partial T}{\partial t} = \frac{K_{\mathrm{z}}}{\epsilon}\frac{\partial^2 T}{\partial z^2} - \frac{C_{\mathrm{p,g}}}{R}\frac{\partial P}{\partial t} - \frac{C_{\mathrm{p,g}}}{R}\frac{\partial}{\partial z}\left(vP\right) - \frac{1-\epsilon}{\epsilon}C_{\mathrm{p,a}}T\sum_{i=1}^{n_{\mathrm{comp}}}\frac{\partial q_i}{\partial t} + \frac{1-\epsilon}{\epsilon}\sum_{i=1}^{n_{\mathrm{comp}}}\left(\left(-\Delta H\right)\frac{\partial q_i}{\partial t}\right) - \frac{2h_{\mathrm{in}}}{\epsilon r_{\mathrm{in}}}\left(T - T_{\mathrm{w}}\right) \tag{2.19}$$

Column wall energy balance

$$\rho_{\mathrm{w}}C_{\mathrm{p,w}}\frac{\partial T_{\mathrm{w}}}{\partial t} = K_{\mathrm{w}}\frac{\partial^2 T_{\mathrm{w}}}{\partial z^2} + \frac{2r_{\mathrm{in}}h_{\mathrm{in}}}{r_{\mathrm{out}}^2 - r_{\mathrm{in}}^2}\left(T - T_{\mathrm{w}}\right) - \frac{2r_{\mathrm{out}}h_{\mathrm{out}}}{r_{\mathrm{out}}^2 - r_{\mathrm{in}}^2}\left(T_{\mathrm{w}} - T_{\mathrm{a}}\right) \tag{2.20}$$

Pressure drop

$$v = \frac{4}{150\mu}\left(\frac{\epsilon}{1-\epsilon}\right)^2 r_{\mathrm{p}}^2\left(-\frac{\partial P}{\partial z}\right) \tag{2.21}$$

Table 2.1: Mathematical model equations for mass, momentum and energy transport used in the process simulations.

The transport equations obtainable using the above mentioned assumptions are described in Table 2.1. However, in the PSA cycle simulations discussed in Part I and II, the non-dimensional form of the equations were used.

2.3.2 Initial and boundary conditions

To solve the model equations given in Table 2.1, the initial and boundary conditions were defined. In the simulations performed, the bed was always assumed to be saturated with the weakly adsorbed species at the feed pressure and temperature. For the full cycle PSA simulations, the final condition of each step was taken as the initial condition of the subsequent step. The constitutive steps in a PSA cycle are a combination of the three possible configurations depending on the flow direction of the gas, namely Open-Open, Open-Closed and Closed-Open, shown in Figure 2.1. For the component mass balance, the Danckwert's boundary conditions for a dispersed plug flow system were applied and the analogy between mass and heat was used to obtain the boundary conditions for the energy balance. For an Open-Open step, the pressure

at the exit boundary was used as a boundary condition and the pressure at the inlet was calculated using Darcy's Law, as the inlet velocity was known a priori. On the other hand, for an Open-Closed and Closed-Open steps, the pressure at the open boundary was defined using an exponential pressure profile given by equations 2.22, and the pressure at the closed end was calculated from the Darcy's Law as the velocity at the closed end was 0.

$$P = P_2 + (P_1 - P_2)e^{-\alpha_p t} \tag{2.22a}$$

$$P = P_1 + (P_2 - P_1)e^{-\alpha_p t} \tag{2.22b}$$

where, the pressurization profile in the column in given by equation 2.22a and the de-pressurization profile in the column is given by equation 2.22b. α_p is the rate of pressurization/depressurization in the column, which was tuned to match the experimental pressure profile [30] and the constant was set as $0.5s^{-1}$ in the PSA cycle simulations discussed in further chapters.

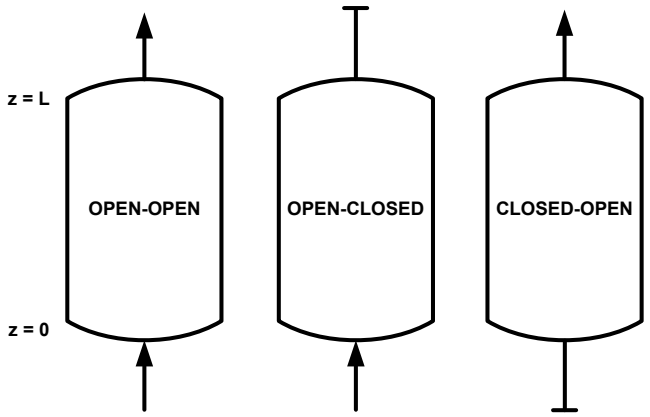

Figure 2.1: Typical configurations of a step in a PSA cycle based on the flow direction of the gas.

	z = 0	**z = L**
Open-Open	$D_{\mathrm{L}}\frac{\partial y_i}{\partial z}\big\vert_{\mathrm{z=0}} = -v\big\vert_{\mathrm{z=0}}\left(y_{i,\mathrm{feed}} - y_i\big\vert_{\mathrm{z=0}}\right)$	$\frac{\partial y_i}{\partial z}\big\vert_{\mathrm{z=L}} = 0$
	$\frac{\partial T}{\partial z}\big\vert_{\mathrm{z=0}} = -\epsilon\rho_{\mathrm{g}}C_{\mathrm{p,g}}v\big\vert_{\mathrm{z=0}}\left(T_{\mathrm{feed}} - T\vert_{\mathrm{z=0}}\right)$	$\frac{\partial T}{\partial z}\big\vert_{\mathrm{z=L}} = 0$
	$T_{\mathrm{w}}\big\vert_{\mathrm{z=0}} = T_{\mathrm{a}}$	$T_{\mathrm{w}}\big\vert_{\mathrm{z=L}} = T_{\mathrm{a}}$
	$v\big\vert_{\mathrm{z=0}} = v_{\mathrm{feed}}$	$P\big\vert_{\mathrm{z=L}} = P_{\mathrm{H}}$
Open-Closed	$D_{\mathrm{L}}\frac{\partial y_i}{\partial z}\big\vert_{\mathrm{z=0}} = -v\big\vert_{\mathrm{z=0}}\left(y_{i,\mathrm{feed}} - y_i\big\vert_{\mathrm{z=0}}\right)$	$\frac{\partial y_i}{\partial z}\big\vert_{\mathrm{z=L}} = 0$
	$\frac{\partial T}{\partial z}\big\vert_{\mathrm{z=0}} = -\epsilon\rho_{\mathrm{g}}C_{\mathrm{p,g}}v\big\vert_{\mathrm{z=0}}\left(T_{\mathrm{feed}} - T\vert_{\mathrm{z=0}}\right)$	$\frac{\partial T}{\partial z}\big\vert_{\mathrm{z=L}} = 0$
	$T_{\mathrm{w}}\big\vert_{\mathrm{z=0}} = T_{\mathrm{a}}$	$T_{\mathrm{w}}\big\vert_{\mathrm{z=L}} = T_{\mathrm{a}}$
	$P\big\vert_{\mathrm{z=0}} = f\left(P_1, P_2, t\right)$	$v\big\vert_{\mathrm{z=L}} = 0$
Closed-Open	$\frac{\partial y_i}{\partial z}\big\vert_{\mathrm{z=0}} = 0$	$\frac{\partial y_i}{\partial z}\big\vert_{\mathrm{z=L}} = 0$
	$\frac{\partial T}{\partial z}\big\vert_{\mathrm{z=0}} = 0$	$\frac{\partial T}{\partial z}\big\vert_{\mathrm{z=L}} = 0$
	$T_{\mathrm{w}}\big\vert_{\mathrm{z=0}} = T_{\mathrm{a}}$	$T_{\mathrm{w}}\big\vert_{\mathrm{z=L}} = T_{\mathrm{a}}$
	$v\big\vert_{\mathrm{z=0}} = 0$	$P\big\vert_{\mathrm{z=L}} = f\left(P_1, P_2, t\right)$

Table 2.2: Boundary conditions for the three possible configurations for the steps in a PSA cycle shown in Figure 2.1.

2.3.3 Finite volume based solution methodology for a PSA cycle

The adsorption process involves a set of transport equations described in Table 2.1 and these non-linear differential equations needs to be solved both in the spatial and temporal domains. Different numerical methods can be employed to solve the model equations and many of these methods based on approximation of the derivatives based on finite difference [31], orthogonal collocation [32], finite element [33] and final volume methods [34–36] have been studied extensively over the years. Solutions to the hyperbolic problems like the one discussed in this work are not smooth, but they have discontinuities in their solutions such as the concentration and temperature shock waves and hence the solution technique chosen must deal with the discontinuities numerically and computationally. Among these methods, numerical solution obtained based

on the finite volume method was found to be robust, computationally less intensive, captured the shock waves and predicted the performance of a PSA cycle accurately [30, 34]. A detailed description of the finite volume method and its implementation in this work is described in the following subsections.

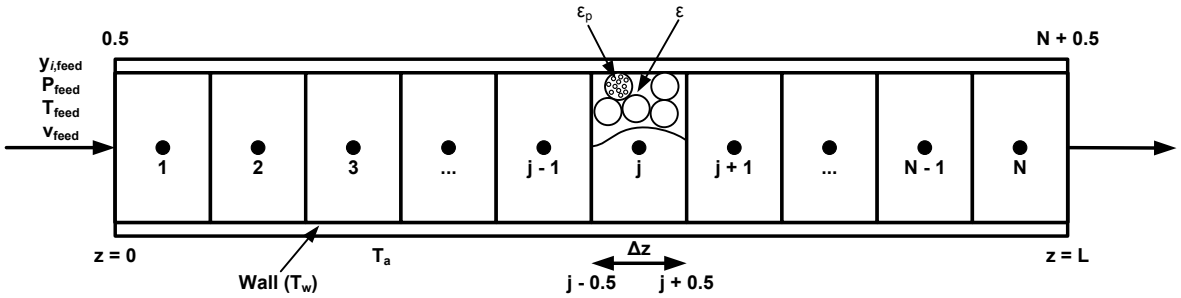

Figure 2.2: Schematic of an adsorption column and spatial discretization for the finite volume scheme

Formulation of the finite volume scheme

In a finite volume method (FVM), the spatial domain in an one-dimensional model is discretized into finite volumes or grid cells and the integral approximation of the conserved quantity given by equation 2.23, f_j is tracked over each of the finite volume. The advantage of using a finite volume method is that the flux is conserved within each control volume as the flux leaving the control volume j shown in Figure 2.2 is identical to the flux entering the subsequent control volume, $j+1$. The finite volume scheme is obtained by integrating the differential form of the governing equation corresponding to a flux which satisfies the law of conservation locally at every grid point. And, as the differential form is integrated over a control volume, the law of conservation holds good in that given control volume and when the boundary conditions are provided correctly, the flux is conserved over the entire domain. This also ensures that the finite volume scheme, in its integral form still holds good at the discontinuities present in the model.

$$f_j(t) = \frac{1}{\Delta V} \int_{V_j} f(t)\, dV \tag{2.23}$$

The spatial derivatives in the model equations given in Table 2.1 are converted to algebraic equations by integrating over each cell, j with boundaries $j - 0.5$ and $j + 0.5$.

Numerical flux limiters for the finite volume scheme

In a process with coupled differential equations there are waves which propagate with different speeds. Hence, the flux numerical limiters needs to be defined such that the solution is accurate

and don't produce any non-physical oscillations. Upwind difference scheme (UDS) is a flux limiter in which the flux entering the edge of a cell, $j + 0.5$ is entirely determined by the flux at the preceding cell, j and is given as follows,

$$f_{j+0.5} = f_j \tag{2.24}$$

The finite volume method reduces to a simple finite difference method with the implementation of a upwind difference scheme flux limiter. The UDS flux limiter is non-oscillatory and can be easily implemented but it produces numerical dispersion which leads to lower accuracy [34].

The numerical dispersion can be overcome by implementing a total variation diminishing (TVD) based flux limiter which also has a higher order accuracy for the solution. In a TVD based flux limiter, the oscillation in the solution is defined using total variation defined as

$$TV = |f_i - f_{i-1}| \tag{2.25}$$

Using the concept of total variation, various flux limiters have been proposed [36]. The flux limiters come into effect when there are sharp wave fronts present in the solution. The smoothness of the solution, $r_{j+0.5}$ is represented by the ratio of successive gradients on the finite volume domain, i.e.,

$$r_{j+0.5} = \frac{f_j - f_{j-1} + \delta}{f_{j+1} - f_j + \delta} \tag{2.26}$$

where, δ is a constant with a very small value, typically 10^{-10}. When the solution is smooth, the value of $r_{j+0.5} \approx 1$ and near any discontinuity in the solution the value of $r_{j+0.5}$ is far away from 1. For a TVD based flux limiter, the flux entering the edge of the cell $j + 0.5$ is given as

$$f_{j+0.5} = f_j + \frac{1}{2}\phi\left(r_{j+0.5}\right)\left(f_{j+1} - f_j\right) \tag{2.27}$$

where, $\phi\left(r_{j+0.5}\right)$ is the flux limiter function. The flux limiter function limits the jumps in the solution given by $r_{j+0.5}$ and thereby limiting the numerical dispersion near discontinuities. Based on the value of successive slope ratio, the flux limiter function switches between a high resolution (smooth function) and a lower resolution scheme (discontinuities). Van-Leer [37] and Superbee flux limiters defined in equation 2.28 fall under the TVD scheme.

van Leer:

$$\phi\left(r_{j+0.5}\right) = \frac{r_{j+0.5} + |r_{j+0.5}|}{1 + |r_{j+0.5}|} \tag{2.28a}$$

Superbee:

$$\phi\left(r_{j+0.5}\right) = max\left[0, min(2r_{j+0.5}, 1), min(2r_{j+0.5}, 2)\right] \tag{2.28b}$$

The calculation of the conserved variable at a cell $j+0.5$ requires the value at $j-1$ and $j+1$. The values of the conserved variable at cell edges ($j = 0.5$ and $j = N+0.5$) are given by the relevant boundary conditions depending upon the PSA step configurations used for a given process. The variable can be calculated for all the control volumes except for the control volume at the inlet of the column, i.e., $j = 1$ as it requires the value at $j = 0$. Hence, a half-cell approximation is made for $j = 0$ and it is assumed that the change in variable from $j = 0.5$ to $j = 1$ is same as the change in the variable from $j = 0$ to $j = 0.5$, i.e.,

$$f_1 - f_0 = 2\,(f_1 - f_{0.5}) \tag{2.29}$$

For the processes described in this work, a TVD finite volume method was implemented to discretize the spatial domain into 30 control volumes. The van Leer flux limiter was found to perform better than Superbee flux limiter both in terms of convergence and computational time [34]. The ordinary differential equations (ODE) on the temporal domain, thus obtained by discretizing the partial differential equations on the spatial domain were integrated using an in-house PSA cycle model in MATLAB. ode23s an inbuilt stiff ODE solver in MATLAB was used to obtain the solution from the set of coupled ordinary differential equations.

2.3.4 Constitutive steps: Basic 4-step PSA cycle

A number of PSA cycle configurations for different separation processes have been explored and are reported in the literature [10]. Most PSA cycles consist of four major constitutive steps, viz., feed pressurization, adsorption, co-current blowdown and a counter-current blowdown step. The cycles discussed in the subsequent chapters are modifications of the basic 4-step PSA cycle. The key features of these steps with respect to cycle described in Figure 2.3 are explained below:

Adsorption

Feed gas is introduced at z=0 at feed pressure (P_{H}) and temperature (T_{feed}). The strongly adsorbing component is adsorbed preferentially over the weakly adsorbing component in this step. The end, z=L is kept open and the weakly adsorbed component is collected at this end, while the bed gets saturated with the feed.

Co-current blowdown

The feed end of the column (z=0) is closed and the column is depressurized from high pressure (P_{H}) to an intermediate pressure (P_{INT}) from the z=L end. This step removes the weakly adsorbed component from the solid and the gas phase and is primarily a light product step,

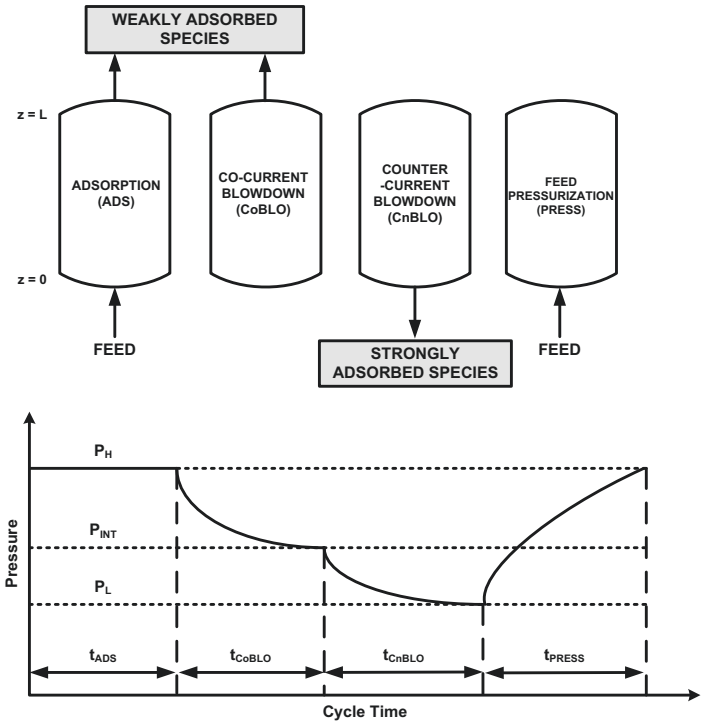

Figure 2.3: Basic 4-step pressure swing adsorption (PSA) cycle with adsorption (ADS), co-current (CoBLO) and counter-current (CnBLO) blowdown and feed pressurization (PRESS) steps.

thereby increasing the concentration of the strongly adsorbed component in the column. Due to depressurization, small amount of the strongly adsorbed component could be lost from the product end.

Counter-current blowdown

The end, z=0 is concentrated with the strongly adsorbed component and in order to remove the from the bed, the column is closed at the end, z=L and is depressurized from an intermediate pressure (P_{INT}) to a low pressure (P_{L}). This is typically the strongly adsorbed product step and depending on the low pressures attained during this step, the bed can be regenerated completely or a significant amount of the strongly adsorbed species could remain in the solid phase.

Feed pressurization

The column at the end of counter-current blowdown step is at a low pressure (P_{L}). The column is pressurized from z=0 end using feed gas while the other end (z=L) is closed. The feed is introduced into the column at a high pressure (P_{H}) and feed temperature. The pressurization

and depressurization in the column follows a pre-defined exponential pressure profile.

2.4 Model validation

Adsorption unlike a distillation process does not have a static steady state, but has a cyclic steady state (CSS). Due to the dynamic nature of the adsorption process, the process is said to be in CSS, when concentration, temperature and pressure profiles across the column does not change with increasing number of cycles; and when the mass balance is closed for the process being considered. The P/VSA process attains CSS after undergoing multiple cycles characterized by a decreasing a mass balance error (ϵ_{MBE}). Overall and component mass balances were defined for the whole cycle and the system was considered to have attained CSS, if ϵ_{MBE} for five consecutive cycles was less than 0.5%. A maximum of 2000 cycles was set for each combination of operating conditions to attain CSS. The mass balance error was calculated at the end of every cycle and was defined as

$$\epsilon_{\text{MBE}} = \frac{|\text{moles in - moles out}|}{\text{moles in}} \times 100 \tag{2.30}$$

The moles in and out of the column are calculated using simple mass balances for the solid and fluid phases. The mass balance for a component in the column was defined as follows:

$$\text{moles in} = \text{moles out} + \text{moles accumulated} \tag{2.31a}$$

$$\text{moles in} = A\epsilon \int_0^{t_{\text{step}}} \left[\frac{P_{\text{in}}(t)\, y_{\text{in}}(t)}{RT_{\text{in}}(t)} v_{\text{in}}(t) \right] dt \tag{2.31b}$$

$$\text{moles out} = A\epsilon \int_0^{t_{\text{step}}} \left[\frac{P_{\text{out}}(t)\, y_{\text{out}}(t)}{RT_{\text{out}}(t)} v_{\text{out}}(t) \right] dt \tag{2.31c}$$

$$\text{moles accumulated} = \text{accumulation in solid phase} + \text{accumulation in fluid phase} \tag{2.31d}$$

$$\text{accumulation in solid phase} = A(1-\epsilon) \int_{z=0}^{z=L} \left[q(z)|_{\text{final}} - q(z)|_{\text{initial}} \right] dz \tag{2.31e}$$

$$\text{accumulation in fluid phase} = A\epsilon \int_{z=0}^{z=L} \left[\left. \frac{P(z)\, y(z)}{RT(z)} \right|_{\text{final}} - \left. \frac{P(z)\, y(z)}{RT(z)} \right|_{\text{initial}} \right] dz \tag{2.31f}$$

where, A, ϵ, L and q are the cross-sectional area, bed voidage, length of the column, and equilibrium solid phase concentration, respectively. The performance indicators namely, purity,

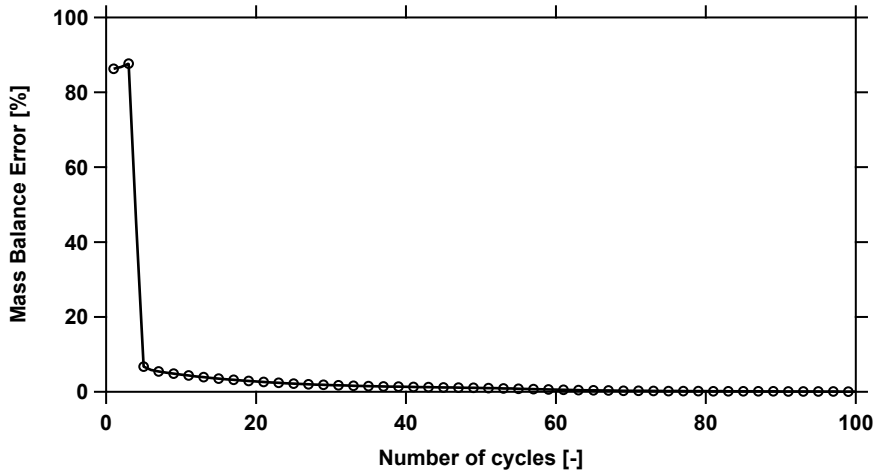

Figure 2.4: Decrease in the mass balance error with the number of cycles for a typical P/VSA cycle.

recovery, energy and productivity were calculated at the CSS. It is worth nothing that, a single column was made to undergo all the constitutive steps of the P/VSA process sequentially. The state of the column at the end of each step is used as the initial condition for the subsequent step. This approach has been a standard practice in adsorption process modeling and has been found to predict multi-column pilot-scale experiments [30]. Translating from a single column to a multi-column can change the productivity as it may change the cycle time as idle steps may be required, but the other performance indicators namely, purity, recovery and energy are unaffected.

Figure 2.4 shows the decrement of mass balance error with the number of cycles for a typical P/VSA cycle. As seen from the figure the mass balance error drops from the very first cycle and after ≈ 80 cycles, the curve flattens out and at this condition the system is said to have attained CSS. Depending on the material, cycle configuration and process conditions, the number of cycles necessary for the system to reach CSS might change. It is worth showing the relative positions of the concentration, temperature and pressure gradient across the column with increasing number of cycles. The gas phase and solid phase concentration profiles for the adsorption step are shown in Figure 2.5, for a given set of operating condition for post-combustion CO_2 capture on Zeolite 13X. After a few cycles, the transient profiles across the column do not change with the number of cycles. Such a behavior is observed in all the constitutive steps and for a given cycle, the profiles change their positions between individual steps, but once the system reaches CSS, the profiles remain unchanged between different cycles. It has been observed that for systems studied in this work, for cases with a very sharp isotherm for the heavy component, the number of cycles required to reach cyclic steady state was in the order of 600-700 cycles, while for linear isotherms it was in the order of 50-60 cycles.

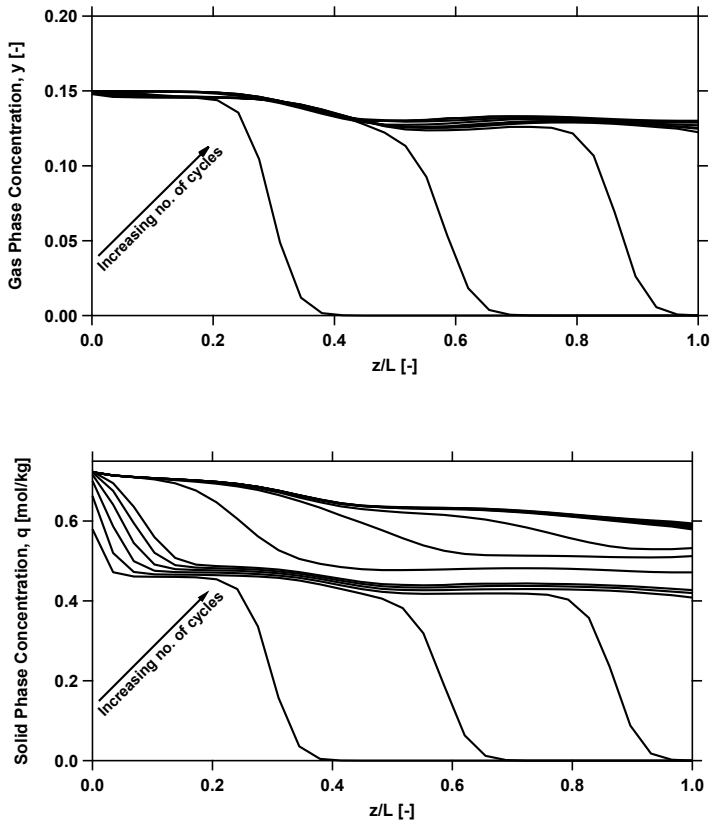

Figure 2.5: Transient solid phase and gas phase concentration profiles across the column observed in a P/VSA process.

Model validation with pilot scale experiments

The model was found to reach the mass balance constraints without compromising on the dynamics of the PSA process. The model was validated with pilot scale experiments reported elsewhere [30]. The transient profiles obtained from the pilot scale experiments were comparable to the profiles obtained from numerical simulations using the full cycle model. Also, the performance indicators namely, purity, recovery, energy consumption and productivity from the model were compared with pilot scale experiments. The purity and recovery were found to be in good agreement, while the predictions for the productivity had modest agreement. The energy consumption of the vacuum pumps calculated using the isentropic equations in the model had a large deviation from the values observed from the pilot scale studies. The efficiency for the vacuum pumps used in the model was assumed to be $\approx 70\%$, while comparison between the pilot plant and model energy consumption, clearly indicated a lower efficiency of $\approx 30\%$ for the vacuum pumps. Nevertheless, the trends observed for the energy consumption were comparable

and hence, the model can be used used evaluate the performances for the adsorptive processes described in chapter 3, 4 and 5.

2.5 Process optimization of a PSA cycle

For any given separation process, maximizing the purity and recovery of the desired product is of paramount importance. Furthermore, the energy consumption for the separation process must be minimized and the productivity, which represents the amount of product that could be purified for a given volume of adsorbent and cycle time must be maximized. The energy consumption and productivity are often used as a proxy for operating and capital expenses, respectively. The CO_2 separation processes considered in this work must satisfy regulatory targets, i.e., CO_2 purity and recovery in excess of 90% [38]. Rigorous optimization has to be performed to identify operating conditions that would minimize the energy consumption and maximize the productivity by meeting the purity-recovery demands. Maximizing purity-recovery and minimizing energy and maximizing productivity involves competing objectives, with the later optimization problem involving constraints on the purity-recovery. Hence, when the optimization problem is defined, a global optimization tool which could be used find the global minima taking into account multiple objectives and could also implement the constraints associated with the process.

A non-dominated sorting genetic algorithm (NGSA-II) [39] available in the MATLAB global optimization tool box was found to meet the requirements associated with choosing an optimization tool. The genetic algorithm (GA) can be used to solve both unconstrained and constrained optimization problems. The GA solves using natural selection which mimics biological evolution. The algorithm chooses an initial population, a combination of the decision variables (step times, pressures and feed velocity in this work). A fitness value is calculated for each member of the current population, and based on the fitness value members called parents are created by the optimizer. The optimizer then creates children from the parents either by a *crossover* between different members of the population or by *mutation*, where random changes are made to a single parent. The parents are replaced by the children to form the next generation. By making changes over a number of generations, the population marches towards an optimal solution. The genetic algorithm is stochastic in nature and the algorithm has the ability to escape local minima, but a global optima is not guaranteed. The major advantage of using GA is that the optimizer is parallelizable to speed-up the optimization and it can be easily coupled with the full-cycle PSA model described in the preceding section.

The typical workflow of an optimization routine is shown in Figure 2.6. The optimizer combines the decision variables randomly to generate an initial population which is input to the full cycle PSA model. The objective functions in the form of performance indicators, namely, purity,

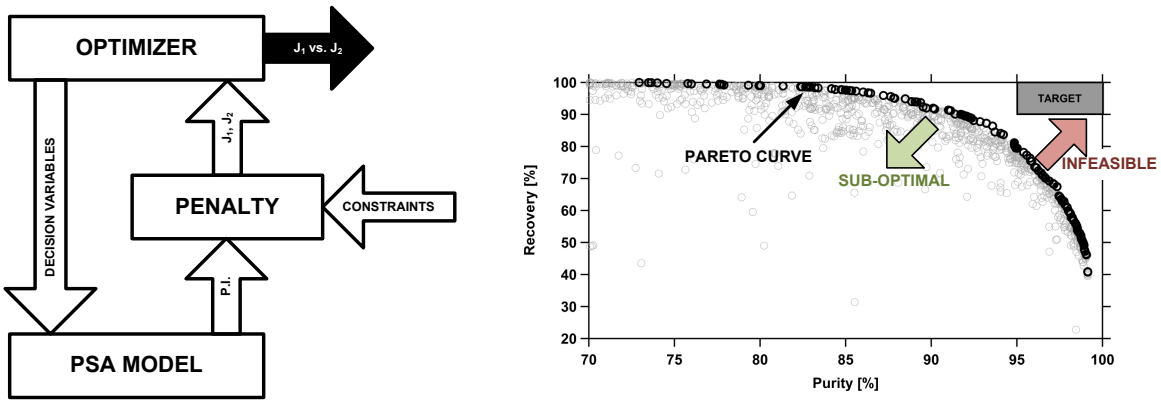

Figure 2.6: Typical workflow of process optimization for the PSA cycles discussed in this work and trade-off obtained between purity-recovery at the end of a full-cycle process optimization. Note: P.I. are the performance indicators and J_1/J_2 are the objective functions evaluated when the cycle attains CSS.

recovery, energy or productivity are calculated once the cycle reaches CSS. For an unconstrained optimization problem, the cycle repeats till one of the optimization stopping criteria is met, which can be the maximum number of generations or the tolerances for the objective function. While, for a constrained optimization problem, if the desired constraints are not met, the objective function is penalized and sent to the optimizer to calculate the fitness value for each member of the population. Once the stopping criteria is met by the optimizer, a trade-off (J_1 vs. J_2) between the objective functions is obtained. A typical output at the end of the optimization routine is also shown in Figure 2.6. Each point shown in the figure, corresponds to performance indicator calculated at CSS for different operating conditions (decision variables). The black curve represents the pareto curve, which is the "best" trade-off obtained by varying the decision variables. It is worth noting that improvement in one of the objectives is always accompanied by a decrement in the other. Any point below the pareto curve is sub-optimal which would mean that the process could essentially perform better, while any point above the pareto curve is infeasible. Hence, an ideal process would correspond to the operating conditions on the pareto curve.

For the optimization results discussed in subsequent chapters, a maximum of 50 generations has been set as the stopping criteria for the GA. Members of the initial population and size of the population plays a key role in generating a diverse population. The initial population was generated using latin hypercube sampling (LHS), as the initial population generated by in-built MATLAB functions were found to be biased towards the bounds of the decision variables. A population size of 24 times the number of decision variables was used for the multi-objective optimization. The larger population size comes at the cost of longer computational times, but

allowed the optimizer to thoroughly search the entire decision variable space which enabled the optimizer to escape local minima.

All computations reported in this work were carried out on a desktop workstation with two 12-core INTEL Xeon 2.5GHz processors and 128GB RAM. The pareto curves reported were obtained by taking the best points from different optimization routines with different initial populations. A typical purity-recovery optimization took around 8-16 hours for generating a pareto curve, while it was around 3-4 days for an energy-productivity optimization.

2.6 Conclusions

Different empirical isotherm models were presented in this chapter which would be used in the subsequent chapters to define adsorption equilibria on a given adsorbent adsorbent. A non-isothermal, non-isobaric full-cycle PSA model along with the necessary boundary conditions was presented. A finite volume based technique based on van-Leer flux limiter was used to discretize the set of coupled partial differential equations in the spatial domain. The van-Leer based FVM technique was found to be robust and efficient, and with 30 volume elements the method was able to achieve the desirable accuracy for process performance indicators. The model presented was able to accomplish the mass balance constraints on the system. Also, a full-cycle multi-objective optimization based on genetic algorithm was presented. The genetic algorithm based optimization was parallelizable and had the ability to escape local minima. The model coupled with the optimizer will be used in the subsequent chapters to predict process performances for the different processes and adsorbents considered in this work.

Part I

Post-combustion CO_2 capture

Chapter 3

Process optimization based adsorbent screening of Mg-MOF-74, Zeoilte 13X, UTSA-16 and activated carbon

3.1 Introduction

In recent years there has been a significant development in the synthesis of novel materials and processes to capture CO_2 from anthropogenic sources. Absorption and adsorption based processes have been proposed over the years to capture CO_2 [40–43]. CO_2 capture based on pressure swing adsorption (PSA) and temperature swing adsorption (TSA) have been studied extensively. A PSA based CO_2 capture system is advantageous due to shorter cycle times when compared to a TSA based CO_2 capture thereby increasing the throughput for a given volume of adsorbent [10] . In designing an adsorption based separation process, the choice of adsorbent plays a crucial role [9]. On the one hand, classical materials like Zeolite 13X, Activated Carbon have been used and studied extensively as adsorbents in an adsorption based CO_2 capture process. On the other hand, novel materials like the metal organic frameworks (MOFs) have caught recent attention due to the high CO_2 storage capacities and selectivity, some even in the presence of moisture [13, 44, 45].

Figure 3.1 shows the typical workflow starting from adsorbent synthesis to process development. The process starts with synthesis where a few milligrams/grams of adsorbent is synthesized. The adsorbent is then characterized to measure various properties such as porosity, surface area, heats of adsorption, etc. At this stage of development, the single component isotherms of the main constituents of the gas are measured. Isotherms of key impurities in the gas, if any,

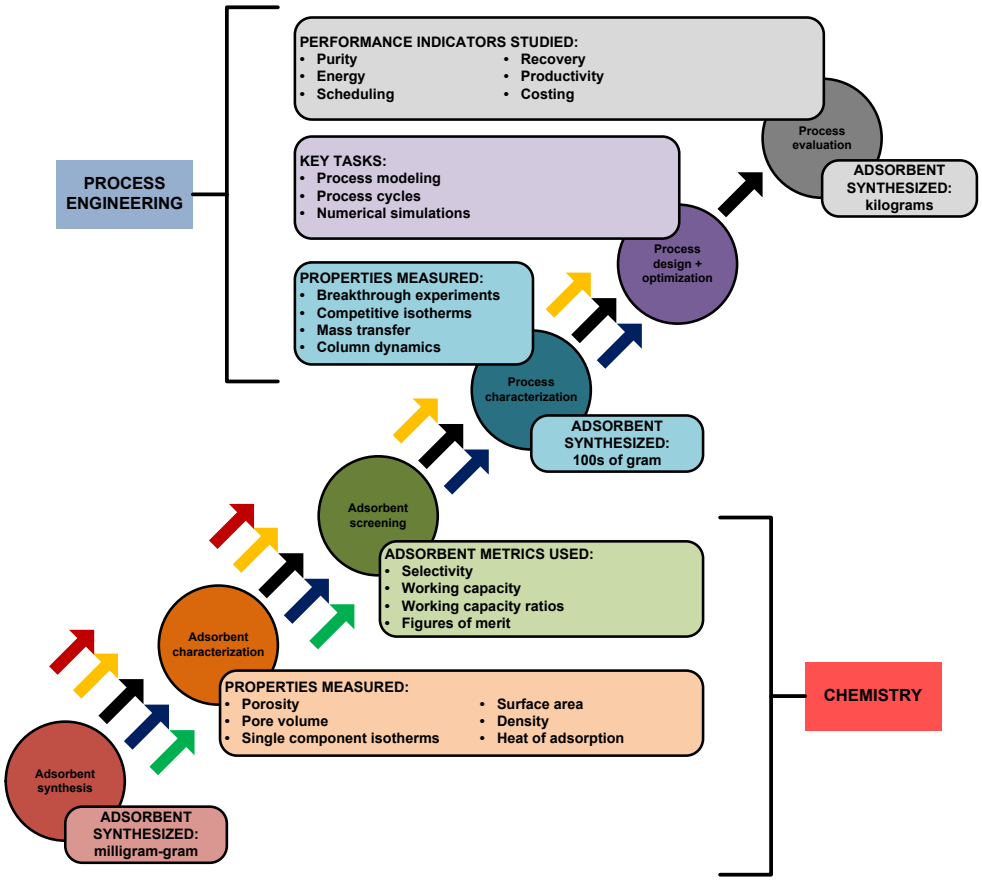

Figure 3.1: Typical workflow of an adsorption based separation process from adsorbent synthesis to full scale process development.

may also be measured at this stage. In most cases, binary/multi-component isotherms are not measured at this stage and this effort is postponed until screening is completed. Screening is an important decision making step where adsorbents that are deemed to move on for further evaluation are selected and the development of unsuitable adsorbents are terminated. Once the screening is performed, larger quantities (100s of grams) are produced; the ability to form particles is explored and the particles or other suitable forms are explored. At this stage, process characterization is performed which typically involves measurement of binary/multi-component isotherms, evaluating the mass transfer effects and studying the interplay of heat and mass transfer. These experiments also provide key input parameters for computer-based process design and optimization. Once a suitable process is determined, it is tested on a lab-scale or a pilot-scale system where process performance indicators such as purity, recovery, energy, productivity, costs are evaluated. If these indicators are favorable process, is scaled up for industrial application.

In the workflow discussed here adsorbent screening is a key stage-gate node as important decisions are made about which materials should be carried forward. It also symbolizes the step

where the development 'baton' is handed over by the chemists to the engineers. Owing to the dearth of detailed information about the adsorbents, screening is traditionally performed based on the so-called "adsorbent metrics". Simple adsorbent metrics that could be evaluated using isotherms, that are readily available once an adsorbent is synthesized have been used to screen adsorbents. Many adsorption metrics have been proposed in the literature. They vary in complexity and are listed in Table 3.1. While this list is not exhaustive, they represent some of the most commonly used metrics.

Selectivity, analogous to the concept of relative volatility used in distillation, is perhaps the most commonly used metric. The selectivity is defined as

$$\alpha = \frac{\left(\frac{\text{equilibrium solid loading of heavy component}}{\text{equilibrium solid loading of light component}}\right)}{\left(\frac{\text{gas phase composition of heavy component}}{\text{gas phase composition of light component}}\right)} \tag{3.1}$$

Many definitions of selectivity are traditionally used. They mostly vary in the manner in which the equilibrium solid loading is calculated. The Henry selectivity is calculated at low concentrations, i.e., at the limit where the adsorption isotherm is linear. For pure component selectivity, α_{P}, the equilibrium loadings are calculated at the partial pressure corresponding to the feed but without accounting for competitive/co-operative adsorption. For the competitive selectivity, the solid loadings are calculated again at the feed composition, but now by accounting for competitive/co-operative adsorption. The major drawback of selectivity arises from the fact that it does not consider the differences in equilibrium solid phase loading caused by a pressure or temperature swing enforced in an adsorption process. This aspect is critical as it determines the effective amount of gas that could be adsorbed and desorbed from an adsorbent. To account for the regeneration of the adsorbent during a pressure or temperature swing process, the working capacity has been used. The working capacity of an adsorbent is defined as the difference in equilibrium capacities between the high and low pressures for the case of P/VSA and high and low temperature for the case of TSA. Typically the high pressure corresponds to the partial pressure of the components in the feed. The definition of the equivalent quantity for the low pressure for the case of PSA (and the high temperature for TSA) is often not defined clearly. Some practitioners consider the lowest total pressure at a composition of the product or sometimes at the feed composition. Selectivity and the working capacity using the pure component isotherms at a given feed condition have been suggested as adsorbent metrics [46]. It is worth noting the definition of selectivity and working capacity does not take into account the change in temperature which is common owing to the exothermic nature of adsorption.

Further to the use of selectivity and working capacity, lumped parameters of selectivity and working capacity were proposed by [47–49] for a PSA based air separation process. These "figures of merit" proposed by [47] and [48] were defined such that the multi-component equilibrium load-

ings were evaluated at pressure, temperature and composition corresponding to the adsorption and desorption conditions rather than a single point loading used in the calculation of selectivity and working capacity discussed above. These metrics were defined for evaluating and selecting adsorbents for layered bed bulk gas separation and emphasized on having a high selectivity and working capacity for an adsorbent to be preferred for a separation process. The figure of merit proposed by [49] was a simplified form of the figure of merit proposed by [47], as it assumed that for a good experimental fit to an equilibrium model, the adsorption and desorption selectivities would be similar. The metric accounted for the working capacity of both the heavy and the light species rather than just the heavy species as was the case with [47]. Yang's FOM was applied for an air separation process and was shown to have a direct correlation with purity, recovery or product throughput if two of these indicators were fixed.

Analytical solutions for isothermal PSA cycles based on equilibrium theory for linear and nonlinear isotherm models have been proposed earlier [50, 51]. A simplified model for rapid adsorbent screening was recently put forward by [52]. In this model a simple cycle was simulated by assuming the adsorption column to be batch system, i.e., in the absence of axial gradients. This effectively simplified the constitutive partial differential equations to ordinary differential equations. Using this model, the authors studied various parameters that affect process performance. The simplified model was able to capture the equilibrium effects along with the heat effects which were absent in the equilibrium theory models. These models were developed for a given cycle configuration, hence they overcame the limitation of the absence of cycle configuration in simple screening metrics.

Adsorbent screening using molecular modeling has been used in the recent years. In one of the recent studies [53], screening of 14 different metal organic frameworks (MOFs) was performed using Monte Carlo simulations on a model which considered the electrostatic and Lennard-Jones interactions among the atoms. The different MOFs were ranked using the uptake rates at feed conditions (0.1 bar and room temperature). The authors have suggested that using molecular modeling can aid in selecting adsorbent materials and understand the mechanism of CO_2 adsorption. The parasitic energy due to CCS is important and it is ultimately one of the deciding factors for an adsorbent material or process to be used on a commercial scale. Recently, a parasitic energy curve was proposed [54], which relates the parasitic energy with the Henry coefficient (adsorption equilibrium constant in the Langmuir isotherm model) of CO_2. 1000s of hypothetical materials were generated using Monte Carlo simulations and the equilibrium for CO_2 and N_2 on these materials were described using single- or dual-site Langmuir isotherm models. For each of these materials, optimal process conditions to minimize the parasitic energy were evaluated using a hybrid pressure and temperature swing adsorption cycle. The study indicates that an ideal adsorbent is one which has a high selectivity such that it can adsorb significant amounts of CO_2, but not very high that regenerating the adsorbent becomes difficult.

The major shortcoming of this approach stems from the fact that the material selection process is approached using the CO_2 Henry coeffecient while the effect of N_2 even though it has been accounted for in the definition of the adsorption equilibria, the effect of N_2 on the parasitic energy is not addressed.

Simulations of adsorption processes involve the solution of coupled algebraic and partial differential equations which are complex and time consuming. Further, explicit design-methods are established only for simple processes under limiting conditions of isothermal operating coupled with the assumption of local equilibrium. hence adsorbent metrics were developed to overcome the limitations and to provide researchers an easy tool to identify promising adsorbents. It is important to note that most metrics and simplified models do not take into account mass and heat transfer effects, cycle configurations, pressure drop effects, characteristics of wave dynamics that occur during adsorption and desorption operations. Further, most the metrics were developed for raffinate cycles, i.e., separations where the light component was the target product. Finally, it is still not clear which process performance, e.g. purity, recovery, energy, etc., the adsorbent metrics correlate to. Over the years adsorbent metrics have been used as the de-facto criterion to make claims that one adsorbent is better than the other. This trend is noticed particularly in the area of CO_2 capture which has spurred the development of hundreds of new materials.

The main goal of this work is to revisit these adsorbent metrics and ask a key question " Can adsorbent metrics be reliably used to screen adsorbents? ".This important question is answered by considering the case of post-combustion CO_2 capture, a topic that has occupied the interest of both synthetic chemists and engineers. We consider four adsorbent materials, the properties of which have been reported in the literature. In order to answer the question, we consider process design using detailed models that have been demonstrated to predict pilot scale operations and cycle optimization which allows the thorough search for thousands of operating conditions, thereby allowing the adsorbent to "choose" operating conditions that maximize its ability.

Adsorbent Metric	Definition	Adsorbents				References
		Mg-MOF-74	Zeolite 13X	UTSA-16	Activated Carbon	
Adsorption capacity	$q^*\vert_{\text{feed}}$	<u>6.36</u>	3.44	2.33	0.90	[17]
Henry selectivity	$\alpha_{\text{H}} = \frac{H_{\text{CO}_2}}{H_{\text{N}_2}} = \frac{(q_{\text{sb}}b+q_{\text{sd}}d)_{\text{CO}_2}}{(q_{\text{sb}}b+q_{\text{sd}}d)_{\text{N}_2}}$	385.80	<u>834.41</u>	374.84	18.12	[55]
Pure-component selectivity	$\alpha_{\text{P}} = \left[\left(\frac{q^*_{\text{CO}_2,\text{Pure}}}{q^*_{\text{N}_2,\text{Pure}}}\right)\frac{y_{\text{N}_2}}{y_{\text{CO}_2}}\right]\Big\vert_{\text{feed}}$	45.49	69.82	<u>200.62</u>	17.99	[17]
Competitive selectivity	$\alpha_{\text{C}} = \left[\left(\frac{q^*_{\text{CO}_2,\text{Comp}}}{q^*_{\text{N}_2,\text{Comp}}}\right)\frac{y_{\text{N}_2}}{y_{\text{CO}_2}}\right]\Big\vert_{\text{feed}}$	404.08	<u>981.45</u>	374.84	60.55	[17]
Pure-component working capacity	$\beta_{\text{P}_i} = \left(q^*_{ads,\text{Pure}} - q^*_{des,\text{Pure}}\right)\Big\vert_{\text{feed}}$	<u>2.07</u>	1.04	1.59	0.64	[17]
Competitive working capacity	$\beta_{\text{C}_i} = \left(q^*_{ads,\text{Comp}} - q^*_{des,\text{Comp}}\right)\Big\vert_{\text{feed}}$	<u>2.05</u>	1.03	1.58	0.51	[17]
Notaro's FOM	$\gamma_{\text{N}} = \beta_{\text{C}_{\text{CO}_2}}\left(\frac{\alpha^2_{\text{C}_{ads}}}{\alpha_{\text{C}_{des}}}\right)$	866.00	<u>1189.12</u>	594.15	68.17	[47]
Ackley's FOM	$\gamma_{\text{A}} = \beta_{\text{C}_{\text{CO}_2}}\left(\frac{\beta_{\text{P}_{\text{CO}_2}}}{\beta_{\text{P}_{\text{N}_2}}}\right)$	5.52	4.01	<u>39.59</u>	1.21	[48]
Yang's FOM	$\gamma_{\text{Y}} = \alpha_{\text{P}}\left(\frac{\beta_{\text{P}_{\text{CO}_2}}}{\beta_{\text{P}_{\text{N}_2}}}\right)$	122.61	269.94	<u>5010.71</u>	42.88	[49]
Wiersum's FOM	$\gamma_{\text{W}} = \frac{(\alpha_{\text{C}}-1)^{0.5}\beta^2_{\text{C}_{\text{CO}_2}}}{\left\vert\Delta H_{\text{ads}_{\text{CO}_2}}\right\vert}$	<u>2.71</u>	0.87	1.26	0.04	[56]

Table 3.1: Definition of adsorbent metrics and the comparison of these metrics calculated at 25 °C for different adsorbents considered in this study. The underlined value represents the adsorbent that is ranked best by the specific metric.

3.2 Case Study

3.2.1 Post-combustion capture of CO_2

In this case study, a post-combustion CO_2 capture system from a dry flue gas stream is considered. The flue gas predominantly consists of CO_2 and N_2 along with trace quantities of impurities like SO_x, NO_x and moisture. The impurities present in the flue gas compete for the sites available for adsorption with CO_2 and might also degrade the adsorbents over a period of time. For polar adsorbents, the selectivity of an adsorbent towards water can be more than the selectivity towards CO_2. Even though we acknowledge the fact that impurities might have an impact on the process performance, we have assumed the flue gas to be composed of 15% CO_2 and 85% N_2 available at 1 bar pressure and 25°C. The assumption on the flue gas components would simplify the process and would allow us to rank materials and provide key insights regarding the performances of different materials for the questions posed in this thesis. If the performances of the adsorbent materials are found to be attractive, sensitivity of impurities on such materials can be examined in the future. Previous studies from our group and in the literature have clearly identified the advantage of vacuum swing adsorption over pressure swing adsorption and hence this study considers only VSA based concentration. In order to evaluate the metrics, four different adsorbents are considered; Zeolite 13X, two metal-organics frameworks (MOFs) and activated carbon.

Zeolite 13X is the current benchmark material for CO_2 capture. Zeolite 13X has a high CO_2/N_2 selectivity and has been shown to achieve purity-recovery in excess of 90% in both simulations [43, 57] and in pilot scale demonstrations [30]. Metal-organic frameworks have caught recent attention for their high CO_2 adsorption capacity and selectivity [45]. Hence, two adsorbents namely, Mg-MOF-74 and UTSA-16 were chosen as representative materials. The stability of these materials are still being explored, and large-scale demonstrations have not been reported. However this should not distract the study of these materials to evaluate their potential. Carbonaceous materials like activated carbon are moisture-tolerant and less expensive when compared to other adsorbents [58]. The adsorption mechanism for all the four adsorbents considered in this study were based on physical adsorption and the separation mechanism was equilibrium-based.

3.2.2 Adsorption equilibria

The equilibrium isotherm data for CO_2 and N_2 on Zeolite 13X were measured in our laboratory [30] while the isotherms for Mg-MOF-74, UTSA-16 and activated carbon were obtained from the literature [52, 59]. The adsorption equilibria for the four adsorbents were described using a

dual-site Langmuir (DSL) model:

$$q_i^* = \frac{q_{\mathrm{sb},i} b_i c_i}{1 + \sum_{i=1}^{n_{\mathrm{comp}}} b_i c_i} + \frac{q_{\mathrm{sd},i} d_i c_i}{1 + \sum_{i=1}^{n_{\mathrm{comp}}} d_i c_i} \tag{3.2}$$

where, $q_{\mathrm{sb},i}$ and $q_{\mathrm{sd},i}$ were the solid-phase saturation loadings for the two sites, and b_i and d_i were the adsorption equilibrium constants which followed an Arrhenius-type temperature dependence given by

$$b_i = b_{0,i} e^{\left(-\frac{\Delta U_{\mathrm{b},i}}{RT}\right)} \tag{3.3a}$$

$$d_i = d_{0,i} e^{\left(-\frac{\Delta U_{\mathrm{d},i}}{RT}\right)} \tag{3.3b}$$

The isotherm parameters for the adsorbents are given in Table 3.2 and the fitted pure component isotherms at 25°C are shown in Figure 3.2. From the pure component isotherms, it was clear that the adsorption capacity of CO_2 on Mg-MOF-74 was the highest among the four adsorbents considered followed by Zeolite 13X, UTSA-16 and activated carbon. For the case of Mg-MOF-74, higher CO_2 adsorption capacity was also accompanied by higher N_2 adsorption. The activated carbon had the least non-linearity for CO_2 but was accompanied by a stronger N_2 adsorption compared to Zeolite 13X and UTSA-16.

The adsorbent metrics calculated for the different adsorbents are summarized in Table 3.1. The ranking of adsorbents using different metrics paint an interesting picture. All metrics consistently ranked activated carbon as the least favorable. However, there is no clear winner predicted by the adsorbent metrics. Mg-MOF-74 is predicted as the most favorable by four metrics, while Zeolite 13X and UTSA-16 are ranked as the best by three metrics. Hence, it becomes difficult to rank Mg-MOF-74, Zeolite 13X and UTSA-16 due to discrepancy in the ranking of adsorbents between different screening metrics. It now becomes pertinent to examine which of these materials offers the best separation performance.

	Mg-MOF-74		**Zeolite 13X**		**UTSA-16**		**Activated Carbon**	
	CO_2	**N_2**	**CO_2**	**N_2**	**CO_2**	**N_2**	**CO_2**	**N_2**
$q_{\mathrm{sb},i}$ [mol kg^{-1}]	6.80	14.00	3.09	5.84	5.00	12.70	0.59	0.16
$q_{\mathrm{sd},i}$ [mol kg^{-1}]	9.90	0.00	2.54	0.00	3.00	0.00	7.51	41.30
$b_{0,i}$ [m^3 mol^{-1}]	1.81×10^{-07}	3.45×10^{-06}	8.65×10^{-07}	2.50×10^{-06}	6.24×10^{-07}	2.96×10^{-06}	9.40×10^{-06}	1.81×10^{-03}
$d_{0,i}$ [m^3 mol^{-1}]	1.06×10^{-06}	0.00	2.63×10^{-08}	0.00	1.87×10^{-23}	0.00	1.04×10^{-05}	1.72×10^{-12}
$-\Delta U_{\mathrm{b},i}$ [kJ mol^{-1}]	39.30	15.50	36.60	15.80	30.60	9.77	25.61	8.67
$-\Delta U_{\mathrm{d},i}$ [kJ mol^{-1}]	21.20	0.00	35.70	0.00	44.70	0.00	17.55	44.90

Table 3.2: Dual-site Langmuir isotherm parameters for CO_2/N_2 on the four materials studied.

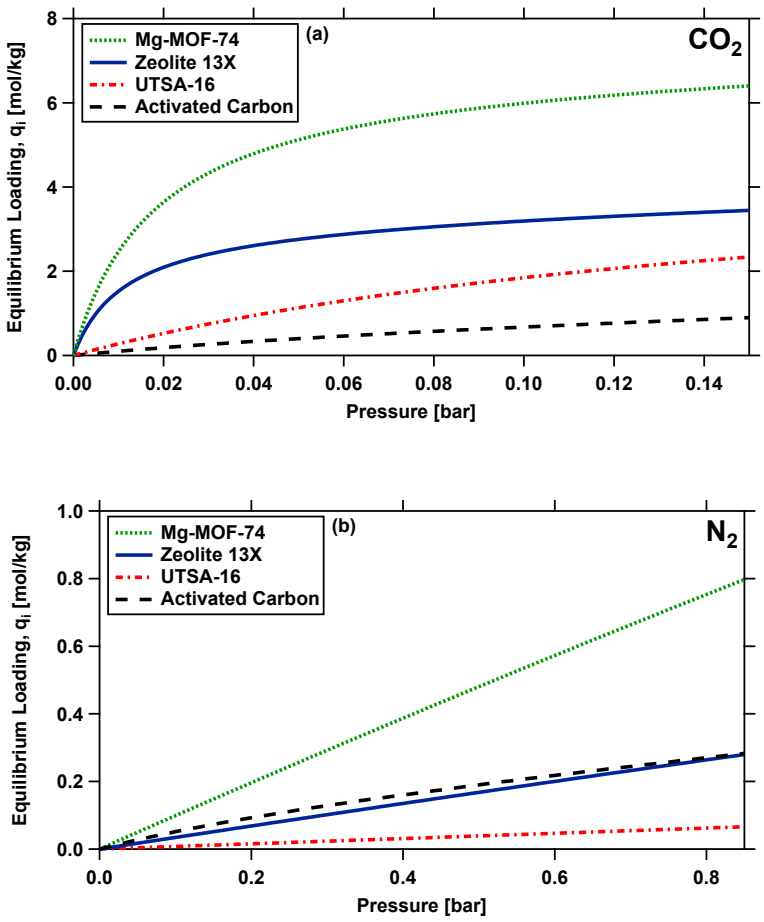

Figure 3.2: Single component isotherms for (a) CO_2 and (b) N_2 at 25°C on the four materials studied.

3.3 Adsorption process design and optimization

3.3.1 Modeling of the adsorption process

In order to evaluate the efficacy of the adsorbent metrics, it is important to evaluate adsorbent performance under realistic conditions. For this a detailed model is developed. The adsorption dynamics in the column is described using a one dimensional mathematical model. The transport equations, a set of coupled non-linear partial differential equations, and the boundary conditions necessary to solve the equations are summarized in the supplementary material. The model assumed an axially dispersed plug flow behavior to represent the gas flow through the fixed bed. The model assumes ideal gas behavior and local thermal equilibrium between the gas and the solid phase. Energy balance equations for the bed and the column wall take into

account the dispersive and convective transfer effects to accurately describe the heat transfer. The pressure drop in the column was considered. Zeolite 13X used in this study was pelletized using a binder and properties of the pellets formed were used in the cycle simulations. For the MOFs, experimental equilibrium data is available only for the crystals and not particles. Hence, it was assumed that binderless particles can be formed wihtout loss in capacity and the equilibrium data for "pseudo" particles was assumed to be identical to the crystals on a "per unit mass" basis. Accordingly the crystal density was used to describe the particle density. Should a pelletization process be developed using a binder, the equilibrium loading is expected to reduce. The controlling mass transfer mechanism in Zeolite 13X has been established to be controlled by molecular diffusion in the macropores. There is no mass transfer study available on the MOF materials. Under this situation it was assumed that the molecular diffusion in the macropores also controls the mass transfer in the other materials as well. When adsorbent properties of Mg-MOF-74, UTSA-16 and activated carbon were unavailable, properties of Zeolite 13X were used for the cycle simulations. The adsorbent properties and the bed voidage was assumed to be uniform across the column and are listed in Table 3.3.

For all the cycle simulations reported in this work, the bed was initially saturated with pure N_2 at 1 bar and 25 °C. As discussed in [34], a finite volume technique using a van-Leer flux limiter [36,37] was used to discretize the system of coupled non-linear partial differential equations into 30 volume elements in the axial direction. The resulting ordinary differential equations (ODE) in the temporal domain were integrated using a stiff solver available in MATLAB. The performance indicators, namely purity, recovery, energy and productivity were calculated once the system had attained cyclic steady state (CSS). The system was considered to have reached CSS, if the mass balance error for five consecutive cycles was less than 0.5%. A maximum of 2000 cycles was set for each combination of operating conditions to attain CSS in the simulations. It is to be noted that for the cycle simulations, a single column was made to undergo the constitutive steps of a cycle in a specified sequence. When there were coupled steps in the process, the output variables from a step namely, fluid phase and solid phase concentrations, the bed and wall temperatures and the pressure across the column were stored in a data buffer. The data stored in the data buffer was used as an input for the coupled step for further simulations. It is worth noting that this is a standard practice in adsorption process simulation. The number of columns required to implement the cycles depends on the duration of each step and the nature of interconnected steps. Translating from a single column to a multi-column configuration can change the value of productivity as idle steps may be required. However, other performance metrics such as purity, recovery and energy consumption will not be affected. The model described here has been shown to successfully predict multi-column pilot scale experiments [30].

3.3.2 Cycle Configuration

In this work a 4-step PSA cycle with a light product pressurization (LPP) shown in Figure 3.3 is used. The rationale behind choosing this configuration stems from the fact that previous optimization work where multiple configurations were studied [43], showed that the 4-step cycle with LPP was superior compared to many others achieving target purity and recovery at the lowest energy consumption. The 4-step PSA cycle with LPP consists of the following steps:

1. **Adsorption (ADS):** Feed gas is introduced at z=0 at the feed pressure (P_{feed}) and temperature (T_{feed}). The strongly adsorbing component (CO_2) adsorbs preferentially over the weakly adsorbing component (N_2) in this step. The end, z=L is kept open and N_2 is collected at this end.

2. **Blowdown (BLO):** The feed end of the column (z=0) is closed and the column is depressurized from high pressure (P_{H}) to an intermediate pressure (P_{INT}) from the z=L end. This step removes the N_2 from the column, thereby increasing the concentration of CO_2 in the column. Due to depressurization, a small amount of CO_2 could be lost from the N_2 product end.

3. **Evacuation (EVAC):** The column closer to z=0 is concentrated with CO_2 and in order to remove the product, the column is closed at the end, z=L and is depressurized from an intermediate pressure (P_{INT}) to a low pressure (P_{L}). This is the CO_2 product step is collected in this step.

4. **Light product pressurization (LPP):** In this step, the feed end, i.e., z=0 is closed and the column is pressurized in the reverse direction, i.e., z=L using the light product obtained from the adsorption step. The LPP step is limited by the high pressure (P_{H}) in the column and once the desired high pressure in the column is reached, the adsorption outlet stream is collected as a raffinate product. If the stream from the adsorption step is not sufficient enough to pressurize the column to the high pressure, an additional feed pressurization step is introduced after the maximum duration of the LPP step is reached, which is set as the time of adsorption step (t_{ADS}). This step serves to compress the CO_2 tail that is formed during the blowdown step and improves CO_2 recovery [43].

3.3.3 Optimization framework

In this work similar to the previous studies, genetic algorithm (GA) is used to optimize the process. Two separate problems are studied. The first one deals with an unconstrained optimization problem of simultaneously maximizing purity and recovery. The second problem deals with maximization of productivity and minimization of energy subject to constraints on purity

Parameter	Value
Column Properties	
Column length, L [m]	1.00
Inner column radius, r_{in} [m]	0.1445
Outer column radius, r_{out} [m]	0.1620
Column void fraction, ϵ [-]	0.37
Particle voidage, ϵ_{p} [-]	0.35
Particle radius, r_{p} [m]	7.5×10^{-4}
Tortuosity, τ [-]	3.00
Fluid and Adsorbent Properties	
Flue gas pressure, P_{feed} [bar]	1.00
Feed temperature, T_{feed} [K]	298.15
Ambient temperature, T_{a} [K]	298.15
Column wall density, ρ_{w} [kg m^{-3}]	7800
Adsorbent density, ρ_{s} [kg m^{-3}]	
Mg-MOF-74	905.00
Zeolite 13X	1130.00
UTSA-16	1680.00
Activated Carbon	799.50
Specific heat capacity of fluid phase, $C_{\text{p,g}}$ [J mol^{-1} K^{-1}]	30.70
Specific heat capacity of adsorbed phase, $C_{\text{p,a}}$ [J mol^{-1} K^{-1}]	30.70
Specific heat capacity of adsorbent, $C_{\text{p,s}}$ [J kg^{-1} K^{-1}]	1070.00
Specific heat capacity of column wall, $C_{\text{p,w}}$ [J kg^{-1} K^{-1}]	502.00
Fluid viscosity, μ [kg m^{-1} s^{-1}]	1.72×10^{-5}
Molecular diffusivity, D_{m} [m^2 s^{-1}]	1.30×10^{-5}
Adiabatic constant, γ [-]	1.40
Effective gas thermal conductivity, K_{z} [J m^{-1} K^{-1} s^{-1}]	0.09
Thermal conductivity of column wall, K_{w} [J m^{-1} K^{-1} s^{-1}]	16.00
Inside heat transfer coefficient, h_{in} [J m^{-2} K^{-1} s^{-1}]	8.60
Outside heat transfer coefficient, h_{out} [J m^{-2} K^{-1} s^{-1}]	2.50
Compression/evacuation efficiency, η [-]	0.72
Universal gas constant, R [m^3 Pa mol^{-1} K^{-1}]	8.314

Table 3.3: Simulation parameters used in PSA cycle modeling for the four materials studied.

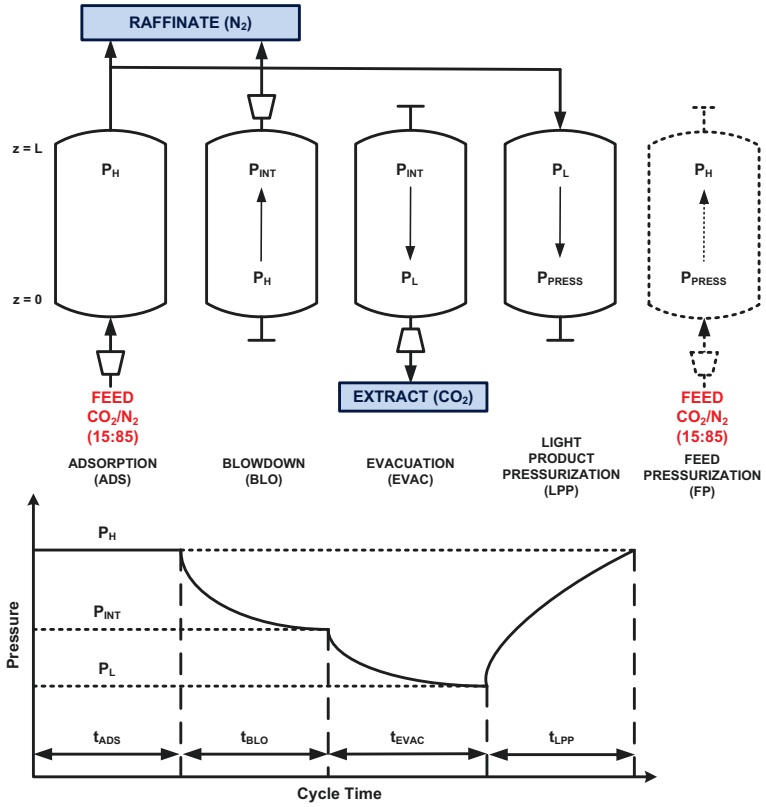

Figure 3.3: Process schematic for a 4-step cycle with light product pressurization (LPP).

and recovery. The objectives are defined as follows:

$$\text{Purity, } Pu\,[\%] = \frac{\text{Total moles of } CO_2 \text{ in the extract product}}{\text{Total moles of } CO_2 \text{ and } N_2 \text{ in the extract product}} \times 100 \tag{3.4a}$$

$$\text{Recovery, } Re\,[\%] = \frac{\text{Total moles of } CO_2 \text{ in the extract product}}{\text{Total moles of } CO_2 \text{ fed into the cycle}} \times 100 \tag{3.4b}$$

$$\begin{aligned}\text{Energy, } En \left[\frac{\text{kWh}}{\text{tonne } CO_2 \text{ captured}}\right] \\ = \frac{E_{ADS} + E_{BLO} + E_{EVAC} + E_{FP}}{\text{Mass of } CO_2 \text{ in the extract product per cycle}}\end{aligned} \tag{3.4c}$$

$$\begin{aligned}\text{Productivity, } Pr \left[\frac{\text{mol } CO_2}{\text{m}^3 \text{ adsorbent . s}}\right] \\ = \frac{\text{Total moles of } CO_2 \text{ in the extract product}}{(\text{Total volume of adsorbent})\,(\text{Cycle time})}\end{aligned} \tag{3.4d}$$

where, E_j refers to the energy consumption in step j.

The objectives were met by varying the decision variables which were the step times for adsorption, blowdown and evacuation; the intermediate and the low pressures; and the feed velocity over a range of conditions. It is well known that GA does not guarantee global minima but has the ability to escape local minima. The GA can be easily coupled with the full cycle one-dimensinal, non-isothermal and non-isobaric PSA model described in the literature [34]. GA is also amenable to parallelization and helps to speed-up the optimization. A non-dominated sorting genetic algorithm proposed by [39] available in the MATLAB global optimization toolbox along with the MATLAB parallel computing toolbox was used in this work. All computations reported in this work were carried out on a desktop workstation with two 12-core INTEL Xeon 2.5GHz processors and 128GB RAM. The GA uses 50 generations with a population size of 24 times the number of decision variables for the multi-objective optimization routines. The larger population size comes at the cost of longer computation times, but allowed the optimizer to thoroughly search the entire decision variable space which enabled the optimizer to escape local minima.

3.4 Results and discussions

3.4.1 Maximization of purity and recovery

One of the main challenges in adsorptive CO_2 capture is the requirement to concentrate from 15 mol % to >90% in the product while achieving a CO_2 recovery in excess of 90%. The constraints on purity arise from sequestration requirements and that on recovery are imposed by regulatory bodies such as the U.S. Department of Energy. Hence, it is paramount that no matter what adsorbent is used, these constraints should be met simultaneously. The four materials considered in this work were subjected to a multi-objective optimization to maximize purity and recovery. The objective functions for the optimization were defined as

$$\min\ J_1 = \frac{1}{Pu_{CO_2}} \tag{3.5a}$$

$$\min\ J_2 = \frac{1}{Re_{CO_2}} \tag{3.5b}$$

The decision variables t_{ADS}, t_{BLO} and t_{EVAC} were varied between 20 - 100 s, 30 - 200 s and 30 - 200 s, respectively; P_{INT} and P_L were varied between 0.03 - 0.50 bar; and v_0 was varied between 0.1 - 2 m s^{-1}. The lowest pressure for the vacuum pump is 0.03bar. This comes from our experience in operating pilot scale units [30] and from previous studies that point to the fact that reducing vacuum pressures to lower values result in increased energy consumption [34]. In order to make the process meaningful a constraint $P_{INT} \geq P_L$ was imposed.

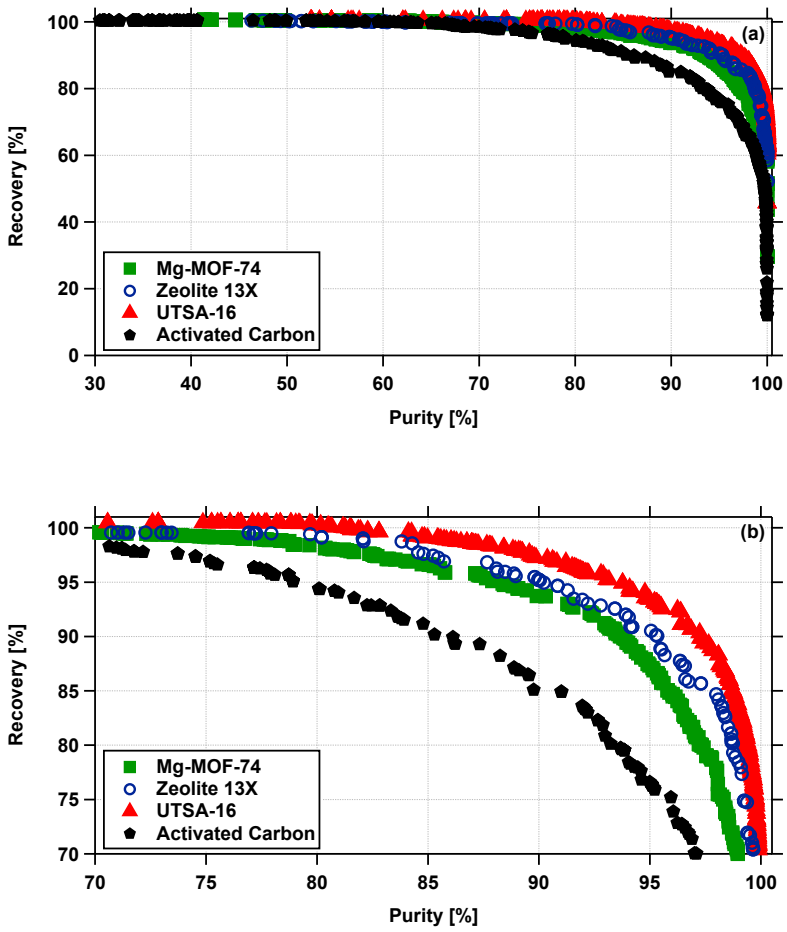

Figure 3.4: Purity-recovery pareto curves for the four materials studied in this work. (The pareto curves for the four materials are plotted on the magnified axis in (b) for clarity.)

The pareto curve provides the "best" trade-off that is achievable for each material. The region to the top-right of each curve is unattainable for the operating range provided; while the region to the bottom-left is sub-optimal. Hence, an ideal process operation is one that lies on the pareto curve. Also note that on the pareto curve, an increase in one of the performance metrics results in lowering the other. The pareto curve for purity-recovery optimization for the four materials is shown in Figure 3.4. As seen from the figure, Mg-MOF-74, Zeolite 13X and UTSA-16 were able to achieve purity and recovery in excess of 90% while the activated carbon was not able to achieve these targets. Further over the entire range of purity and recovery the performance of the four materials can be ranked as UTSA-16> Zeolite 13X> Mg-MOF-74 > activated carbon.The poor performance of activated carbon was in fact predicted by all metrics. This could be explained by the fact that activated carbon has both a weak CO_2 adsorption and a strong N_2 adsorption, i.e, a selectivity that is too low compared to the other materials. The pareto curves of the

other three materials, although are clearly distinct from on-another they are reasonably close to each other. The GA is a stochastic optimization routine and minor deviations in the pareto curves are normally seen. The pareto fronts shown here were obtained by taking the best points from different optimization routines with different initial populations. In all cases the relative position of pareto curves for the different materials was unchanged. At this point it is pertinent to compare the adsorbent metrics to the pareto curves. Of all the metrics only two, namely pure selectivity and Yang's FOM seem to predict the trend correctly. Although they rank the adsorbents correctly the magnitudes of these metrics deserve attention. The pure component selectivity of UTSA-16 is ≈ 2.9 times that of Zeolite 13X and ≈ 4.4 times that of Mg-MOF-74. Similarly, Yang's FOM for UTSA-16 is ≈ 18.5 times larger than Zeolite 13X and ≈ 41 times larger than that of Mg-MOF-74. However the optimization results indicate that the advantage of one material over the other, baring activated carbon, is at best marginal.

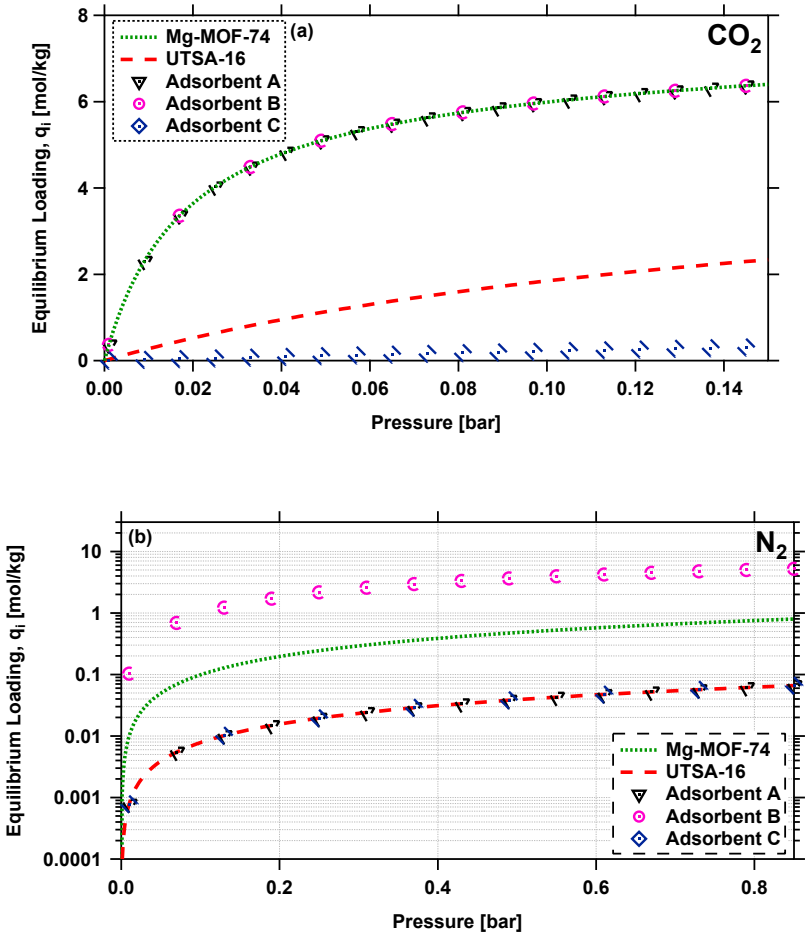

Figure 3.5: Single component isotherms for (a) CO_2 and (b) N_2 at 25°C on Mg-MOF-74, UTSA-16 (solid lines) and three hypothetical adsorbents (open symbols).

	Adsorbent A		Adsorbent B		Adsorbent C	
	CO_2	N_2	CO_2	N_2	CO_2	N_2
$q_{sb,i}$ [mol kg^{-1}]	6.80	12.70	6.80	12.70	6.80	12.70
$q_{sd,i}$ [mol kg^{-1}]	9.90	0.00	9.90	0.00	9.90	0.00
$b_{0,i}$ [m^3 mol^{-1}]	1.81×10^{-07}	2.96×10^{-06}	1.81×10^{-07}	3.95×10^{-04}	1.05×10^{-09}	2.96×10^{-06}
$d_{0,i}$ [m^3 mol^{-1}]	1.06×10^{-06}	0.00	1.06×10^{-06}	0.00	6.19×10^{-09}	0.00
$-\Delta U_{b,i}$ [kJ mol^{-1}]	39.30	9.77	39.30	9.77	39.30	9.77
$-\Delta U_{d,i}$ [kJ mol^{-1}]	21.20	0.00	21.20	0.00	21.20	0.00

Table 3.4: Dual-site Langmuir isotherm parameters for CO_2/N_2 on the three hypothetical materials considered in this work.

In order to understand the effect of selectivity and shape of the isotherm on the process performance, hypothetical adsorbents with different CO_2/N_2 isotherms were chosen and were subjected to a multi-objective optimization to maximize purity and recovery. Three hypothetical adsorbents were considered such that two adsorbents (A and B) had the same CO_2 isotherm parameters as Mg-MOF-74 and two adsorbents (A and C) had the same N_2 isotherm parameters as UTSA-16. CO_2 and N_2 isotherm parameters on the three hypothetical materials, Mg-MOF-74 and UTSA-16 are given in Table 3.4 and the isotherms are shown in Figure 3.5. The Henry selectivity for A, B and C were 4913.91, 36.81 and 28.59, respectively.

The purity-recovery paretos for the three hypothetical adsorbents, Mg-MOF-74 and UTSA-16 are shown in Figure 3.6. Adsorbents A, UTSA-16 and adsorbent C which all had identical N_2 isotherms but different CO_2 isotherms resulted in purity-recovery pareto curves that were very close to each other. This indicates that CO_2 affinity is so strong that a change in CO_2 affinity has a marginal impact on the acievable purity-recovery. At this point it is worth clarifying that should CO_2 affinity have been weaker than what is observed in many materials such as the MOFs and Zeolite 13X, the CO_2 will have a more decisive impact on process performance. Now let us observe the difference between adsorbents A, Mg-MOF-74 and B, which all had identical CO_2 isotherms but different N_2 isotherms. While adsorbents A and Mg-MOF-74 had similar pareto curves, adsorbent B with a strong N_2 affinity showed a pareto that was inferior to all the adsorbents. It is worth noting that even when the Henry selectivity for adsorbents B and C were similar, adsorbent C performed better than adsorbent B. This trend could be explained by considering the N_2 isotherms for the two materials. In the range of working pressures, N_2 isotherm on adsorbent B was sharper than adsorbent C, which contributed to a better performance for adsorbent C.

The analysis with the hypothetical isotherms showed that for an adsorbent which was reasonably selective to CO_2, increasing the CO_2 affinity further did not lead to a significant increase in the achievable purity-recovery but it was the N_2 affinity that seemed to control the process performance.

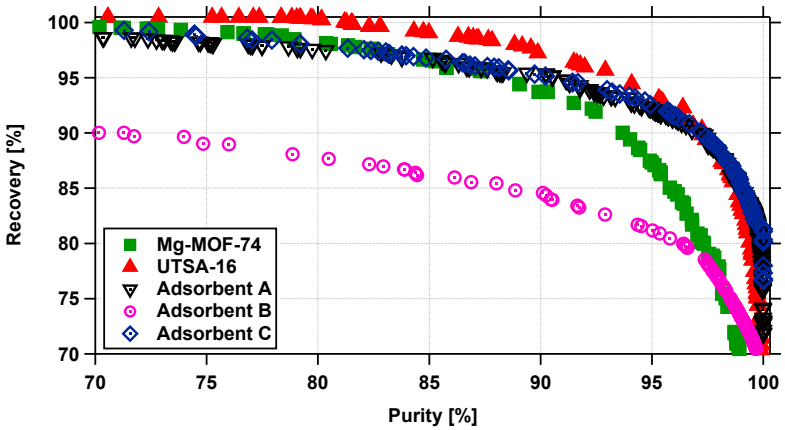

Figure 3.6: Purity recovery pareto fronts for Mg-MOF-74, UTSA-16, and three hypothetical adsorbents.

3.4.2 Minimization of energy and maximization of productivity

In the previous section, we have assessed the performance of the four materials based on their purity-recovery pareto fronts. While the purity-recovery pareto curves provide information about the ability of these adsorbents to meet regulatory requirements they do not provide any information regarding the capital and operating expenses that could be incurred. It is common practice to use productivity and energy consumption as a proxy for capital and operating expenses. Converting these values to cost is a rather complex exercise and is beyond the scope of this work. The material used for a given separation process must have the least energy consumption with the maximum productivity. Hence, the adsorbents which met the purity-recovery requirements, i.e., in excess of 90% were subjected to an optimization to obtain the trade-off between the energy consumption and the productivity. The materials considered for the energy-productivity were the Mg-MOF-74, Zeolite 13X and UTSA-16, while clearly the activated carbon, which did not achieve high purity and recovery, was not considered.

The energy-productivity optimization was a constrained optimization problem; hence the constraints on the purity-recovery had to be accounted for in the definition of the objective for the problem. The objective functions for the optimization problem were defined as

$$\min\ J_1 = \psi_1 E + \lambda_1 \left[\max\left(0, Pu_{\text{target}} - Pu_{\text{CO}_2}\right)\right]^2 + \lambda_2 \left[\max\left(0, Re_{\text{target}} - Re_{\text{CO}_2}\right)\right]^2 \tag{3.6a}$$

$$\min\ J_2 = \frac{\psi_2}{Pr} + \lambda_1 \left[\max\left(0, Pu_{\text{target}} - Pu_{\text{CO}_2}\right)\right]^2 + \lambda_2 \left[\max\left(0, Re_{\text{target}} - Re_{\text{CO}_2}\right)\right]^2 \tag{3.6b}$$

where ψ_i and λ_i were the penalty functions, Pu_{target} and Re_{target} were the target purity and recovery, respectively. The optimization problem defined in Equation 3.6 ensured that the materials considered were able to attain the minimum purity-recovery targets even if an operating

condition which would yield a higher purity-recovery was attainable. The bounds on the decision variables used for the purity-recovery optimization discussed in the previous section were kept unchanged.

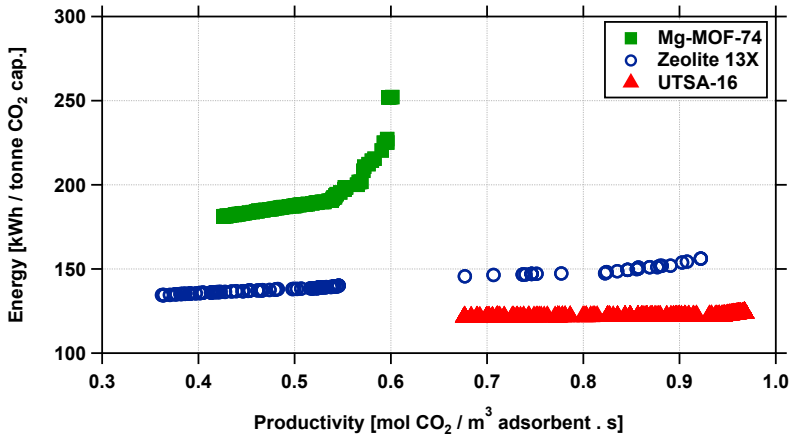

Figure 3.7: Energy-productivity pareto fronts for Mg-MOF-74, Zeolite 13X and UTSA-16 that meet 90% purity-recovery constraints.

The energy-productivity pareto obatined from the optimization is shown in Figure 3.7. All the points in the pareto curve correspond to the different sets of operating conditions which met the purity-recovery constraints. The pareto front of the three materials show a clear distinction with UTSA-16> Zeolite 13X> Mg-MOF-74, a trend that was observed in the purity-recovery optimization. The differences in the performances could be explained by examining the decision variables corresponding to the pareto points. The process configuration includes two vacuum pumps and a blower that contribute to the energy consumption. The contribution from the vacuum pumps is decisive in lowering the energy consumption for a given material or a given process. The energy consumption for a vacuum pump with a delivery pressure of 1 bar is given by

$$E = \frac{1}{\eta}\epsilon\pi r_{\text{in}}^2 \frac{\gamma}{\gamma-1}\int_{t=0}^{t=t_{\text{step}}} vP_{\text{out}}\left[\left(\frac{1}{P_{\text{out}}}\right)^{\frac{(\gamma-1)}{\gamma}} - 1\right] dt \tag{3.7}$$

From equation 3.7, it is clear that the energy consumption depends on the pressure levels between which the vacuum pump operates and the gas flow rate through the vacuum pump. A higher value of P_{out} would result in a lower energy consumption for a vacuum pump. In Figure 3.8, intermediate pressure (P_{INT}) and low pressure (P_{L}) corresponding to the energy-productivity pareto curves are plotted. In order to meet the recovery targets, P_{L} corresponding to the pareto points for all the three materials converge close to the lower bound for P_{L}, i.e., 0.03 bar. The achievable purity for a given material depends on the intermediate pressure, P_{INT}. In order to remove the N_2 from the column to achieve high CO_2 purity from the evacuation step, lower P_{INT} is desired. However lowering P_{INT} also has the tendency to lower CO_2 recovery as it can be lost

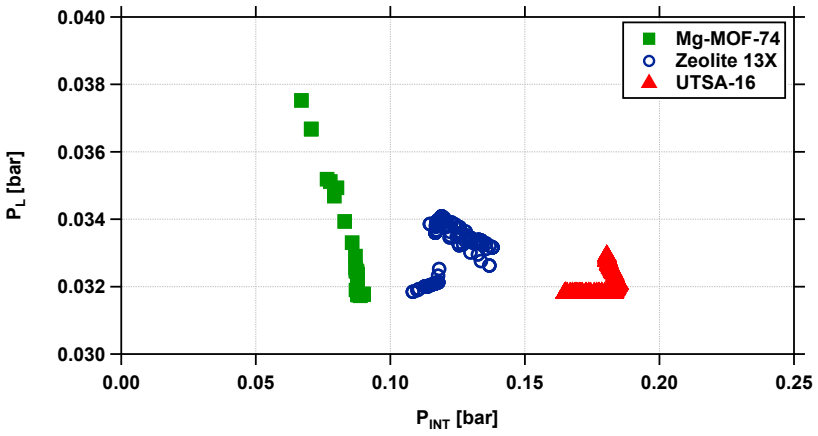

Figure 3.8: Intermediate pressure (P_{INT}) and low pressure (P_{L}) corresponding to the pareto points for Mg-MOF-74, Zeolite 13X and UTSA-16 shown in Figure 3.7.

in the blowdown step. Hence, a desirable material is one where sufficient N_2 can be removed at a higher P_{INT}, and CO_2 can be extracted at a high purity. Among the three materials studied here, nitrogen had the strongest affinity on Mg-MOF-74 and the weakest affinity on UTSA-16. Owing to this, P_{INT} that had to be reached was $\approx$ 0.06-0.09 bar when compared to $\approx$ 0.16-0.18 bar for UTSA-16, while the Zeolite 13X had P_{INT} intermediate to other two materials as shown in Figure 3.8.

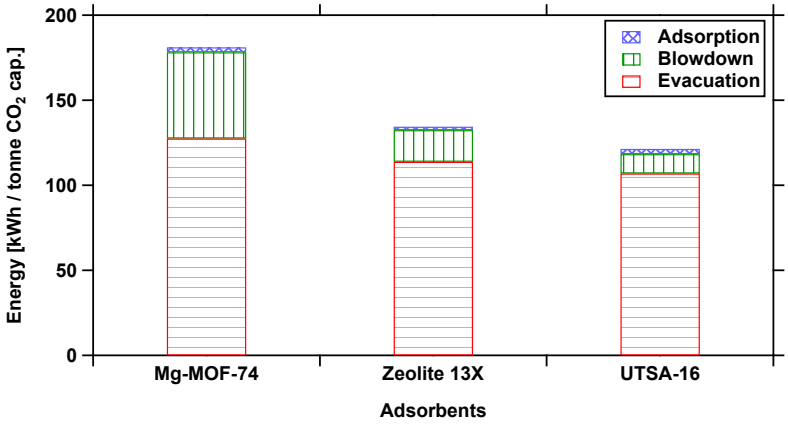

Figure 3.9: Energy contribution from constitutive steps corresponding to the minimum energy consumption for Mg-MOF-74, Zeolite 13X and UTSA-16 for the following operating conditions: Mg-MOF-74 - t_{ADS}=88.97 s, t_{BLO}=156.69 s, t_{EVAC}=131.44 s, P_{INT}=0.090 bar, P_{L}=0.032 bar, v_0=0.59 m s^{-1}; Zeolite 13X - t_{ADS}=88.05 s, t_{BLO}=164.22 s, t_{EVAC}=66.69 s, P_{INT}=0.138 bar, P_{L}=0.033 bar, v_0=0.42 m s^{-1}; UTSA-16 - t_{ADS}=75.42 s, t_{BLO}=90.83 s, t_{EVAC}=73.10 s, P_{INT}=0.180 bar, P_{L}=0.033 bar, v_0=0.68 m s^{-1}.

The energy contribution of the constitutive steps corresponding to the minimum energy consumption for the three adsorbents is shown in Figure 3.9. The energy required by the adsorption and evacuation steps are comparable between the three materials and the key difference arises

from the blowdown step. The energy contribution from the blowdown step for Mg-MOF-74 was 50.75 kWh/tonne CO_2 cap. ($\approx$ 28.02% of total energy consumption), while for UTSA-16 it was 11.33 kWh/tonne CO_2 cap. ($\approx$ 9.34% of total energy consumption). This is directly related to the P_{INT} at the end of the blowdown step shown in Figure 3.8. The lower P_{INT} for Mg-MOF-74 when compared to the other two adsorbents led to a higher energy consumption in the blowdown step, which was decisive in the total energy consumption for a given adsorbent.

It is clear from the above discussions that UTSA-16 was able to achieve the desired purity-recovery targets with the least energy consumption for the 4-step cycle with LPP. The N_2 affinity plays a key role in determining the achievable purity-recovery and thus the energy consumption for the given process.

3.5 Concluding remarks

The main objective of the work presented in this chapter was to evaluate the capability of adsorbent metrics. Their efficacy was evaluated by performing rigorous process optimization for four different adsorbent for post-combustion CO_2 capture from dry flue gas. The study indicated that all adsorbent metrics were able to identify the adsorbent that eventually performed poorly. However among the other three, the relative ranking provided by various metrics were very different. After comparing the results of the process optimization, only two metrics namely, pure component selectivity and Yang's FOM seemed to provide the ranking. However the difference in magnitudes of these metrics between different materials did not correlate with their process performance. While it might be tempting to use these metrics to screen adsorbents, studies reported in chapter 4show that even these two metrics do not have a predictive capability.

The optimization of purity-recovery and energy-productivity provides key insights about the impact N_2 adsorption on the process performance. For most CO_2 capture materials, CO_2 affinity does not show an improvement in achievable performance. This observation stems from the fact that process constraints such as the lowest practically achievable vacuum pressures ($\approx$ 0.03 bar) do not allow the exploitation of sharper CO_2 isotherms. However the ability of an adsorbent to reject N_2 plays a far more important role than what is usually considered during sorbent selection. This observation, which is now obtained from detailed process optimization is consistent with the other observations in literature [52].

We also acknowledge that in this study, it is possible that each adsorbent should be "married" to a process that maximizes the potential [60]. This would require more complex optimization tools such as the use of superstructures [35]. This should be certainly explored in the future. It is also important to stress that eventual success of an adsorbent depends on many other factors that have not been accounted for, e.g. long-term stability, behavior towards impurities,

cost, etc., However, it is our opinion that these considerations are made only if the adsorbent can perform the basic separation task that it is chosen for and methods discussed here allow the researchers to make objective evaluations. In conclusion, this study suggests that including process optimization tools early in the adsorbent development workflow can infact be beneficial.

Chapter 4

A graphical approach for screening adsorbents for post-combustion CO_2 capture

4.1 Introduction

In chapter 3, a process-optimization based adsorbent screening was carried out for four different materials, with different equilibrium CO_2 capacities. Most of the simple adsorbent metrics did not predict the ranking of adsorbents, but the process optimization based screening approach was able to rank adsorbents based on their purity-recovery or energy-productivity performances for a given process configuration. As an extension to the previous chapter, the main objective of this chapter was to perform a systematic study to understand how equilibrium affects the process performance. Hypothetical adsorbents with different non-linearities for both CO_2 and N_2 have been explored and the process performances were evaluated for these materials. The adsorbent equilibrium properties and the process performances are graphically represented to provide directions to the chemists to synthesize materials with desirable properties that would satisfy the purity-recovery constraints with the least energy consumption for a post-combustion CO_2 capture.

4.2 Case study

4.2.1 Adsorption process design and optimization

A post-combustion CO_2 capture from a dry flue gas stream of 15% CO_2 and 85% N_2 available at 1 bar pressure and 25°C is considered. A vacuum swing adsorption based process is the chosen

separation technology for this case study. Zeolite 13X has been widely studied for CO_2 capture because of the high CO_2/N_2 selectivity. Previous studies have shown that post-combustion CO_2 capture with Zeolite 13X as the adsorbent can achieve purity-recovery in excess 90%, and hence would satisfy the current purity-recovery constraints set by regulatory bodies [43, 57]. The adsorption equilibria on the different materials were described using a dual-site Langmuir (DSL) model in chapter 3. As discussed in the previous chapters, the DSL model is not a constant selectivity isotherm model, i.e., the competitive selectivity is a function of fluid phase concentration of the constituent species, which can be attributed to the way the DSL model is defined (Equation 2.3). Whereas, the single site Langmuir (SSL) model, given by Equation 4.1 is a constant selectivity model. The Henry and competitive selectivity for any given concentration depends only on the saturation capacity, $q_{s,i}$ and the adsorption equilibrium constant of the adsorbent, b_i. The SSL adsorption equilibrium model is given as follows:

$$\boldsymbol{q_i^* = \frac{q_{s,i} b_i c_i}{1 + \sum_{i=1}^{n_{comp}} b_i c_i}} \tag{4.1}$$

where, q_i^* is the equilibrium solid phase concentration at a given temperature and pressure, $q_{s,i}$ is the saturation solid phase concentration of the given component i and b_i is the adsorption equilibrium constant which follows an Arrhenius type temperature dependence given by

$$b_i = b_{0,i} e^{-\frac{\Delta U_i}{RT}} \tag{4.2}$$

Equality of saturation capacities, i.e., $q_{s,CO_2} = q_{s,N_2}$, is a requirement to make the Langmuir adsorption isotherm thermodynamically consistent. The Henry selectivity (α_H) and competitive selectivity (α_C) for a SSL model are given as follows:

$$\alpha_H = \frac{q_{s,CO_2} b_{CO_2}}{q_{s,N_2} b_{N_2}} = \frac{b_{CO_2}}{b_{N_2}} \tag{4.3a}$$

$$\alpha_C = \left[\frac{\frac{q_{s,CO_2} b_{CO_2} c_{CO_2}}{1 + b_{CO_2} c_{CO_2} + b_{N_2} c_{N_2}}}{\frac{q_{s,N_2} b_{N_2} c_{N_2}}{1 + b_{CO_2} c_{CO_2} + b_{N_2} c_{N_2}}} \right] \times \frac{c_{N_2}}{c_{CO_2}} = \frac{q_{s,CO_2} b_{CO_2}}{q_{s,N_2} b_{N_2}} = \frac{b_{CO_2}}{b_{N_2}} \tag{4.3b}$$

The main objective of this chapter is to show the effects of equilibrium on process performance, which would mean exploring adsorbents with different CO_2/N_2 isotherms. Zeolite 13X is chosen as the base adsorbent for the study and the CO_2/N_2 isotherm for Zeolite 13X is modified to make the hypothetical adsorbents linear or non-linear with respect to the base adsorbent. The adsorption equilibria on Zeolite 13X and the hypothetical adsorbents are defined using the SSL model. The equilibrium isotherm data for CO_2 and N_2 on Zeolite 13X given in the Appendix are

	$q_{s,i}$ [mol kg^{-1}]	$b_{0,i}$ [m^3 mol^{-1}]	$-\Delta U_i$ [kJ mol^{-1}]
CO_2	4.39	2.50×10^{-06}	31.19
N_2	4.39	2.70×10^{-06}	16.38

Table 4.1: Single-site Langmuir isotherm parameters for CO_2/N_2 on Zeolite 13X.

used to fit the equilibrium data on a SSL model. Although, previous studies have shown that the equilibrium data fits the DSL model better than the SSL [30, 34, 43], in order to understand the effect of the CO_2/N_2 isotherms and the corresponding metrics, the SSL was used as it had constant selectivity for any given concentration and its simple form enabled generating isotherms for hypothetical adsorbents by just varying the b_i of either CO_2 or N_2 or both together. The single component isotherms described using the SSL and DSL model for CO_2 and N_2 at four different experimental temperatures are shown in Figure 4.1 and the SSL parameters for CO_2 and N_2 on Zeolite 13X are given in Table 4.1.

The competitive working capacity ratio (θ_C) defined as the ratio of the working capacity of CO_2 to N_2 and the Yang's FOM (γ_Y) discussed in chapter 3 are a function of adsorption equilibrium constants of the two components and the feed concentration. The two adsorbent metrics, are defined as follows:

$$\theta_C = \frac{b_{CO_2}}{b_{N_2}} \left.\frac{y_{CO_2}}{y_{N_2}}\right|_{feed} \tag{4.4a}$$

$$\gamma_Y = \left[\frac{b_{CO_2}}{b_{N_2}}\right]^2 \left.\frac{y_{CO_2}}{y_{N_2}}\right|_{feed} \tag{4.4b}$$

The effect of Henry and competitive selectivity, competitive working capacity ratio (WCR) and the Yang's FOM will be studied in detail in the subsequent sections. Once the Henry or the competitive selectivity for an adsorbent is fixed, WCR and Yang's FOM can be determined as they are simple extensions of the Henry or competitive selectivity for a SSL model.

To evaluate the performance of the different hypothetical adsorbents a 4-step PSA cycle with light product pressurization (LPP) presented in chapter 3 and shown in Figure 3.3 is used. As discussed before, the rationale behind choosing this configuration was the ability of the process to achieve target purity and recovery with the least energy consumption [43]. The simulation parameters used in the case studies discussed in this chapter are given in Table 3.3. Hypothetical adsorbents with constant Henry selectivity or fixed CO_2 isotherm or fixed N_2 isotherm are put under a process test by performing process optimization to evaluate the maximum purity and recovery that these adsorbents could achieve with the least energy consumption. The full cycle model is coupled with a genetic algorithm to optimize the process for the two problems studied. The first problem is to maximize the purity and recovery, simultaneously and the second problem is to simultaneously minimize energy and maximize productivity with constraints on purity and

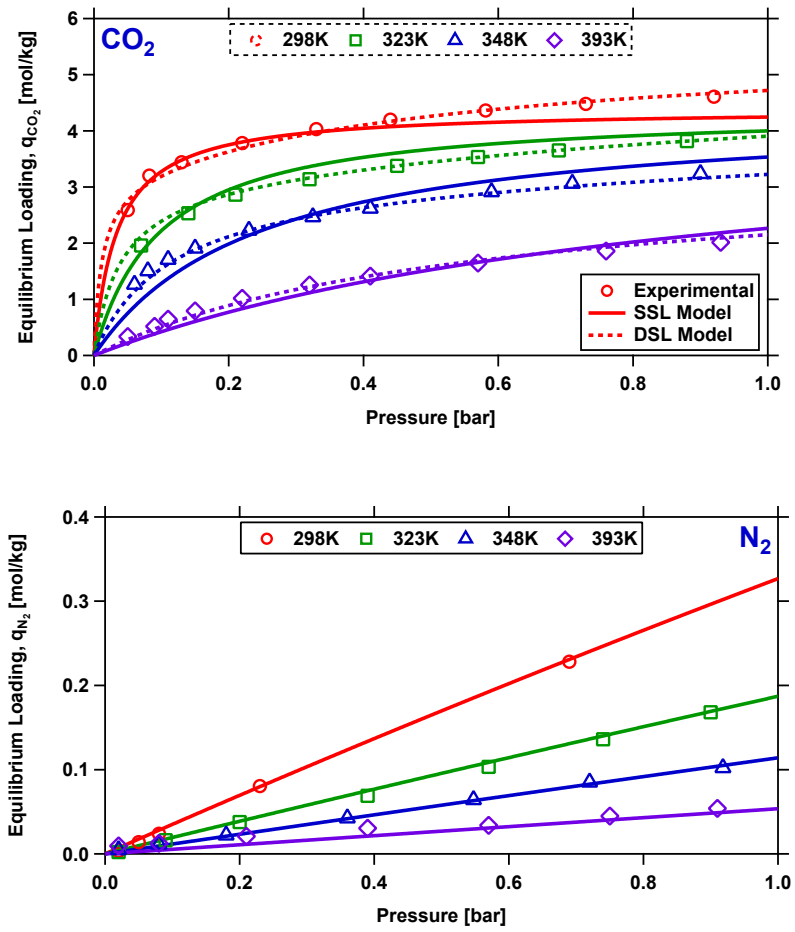

Figure 4.1: Experimental equilibrium loadings (open symbols), single component isotherms for CO_2 and N_2 using single site Langmuir model (solid lines) and dual site Langmuir model (dotted lines) at four different temperatures on Zeolite 13X.

recovery to be in excess of 90%. The decision variables for the optimization routine t_{ADS}, t_{BLO} and t_{EVAC} are varied between 20 - 100s, 30 - 200s and 30 - 200s, respectively; P_{INT} and P_{L} are varied between 0.03 - 0.50 bar; and v_0 is varied between 0.1 - 2.0 m s^{-1}.

4.2.2 Non-linearity plot

The hypothetical adsorbents studied in this work were chosen such that their non-linearity was scaled with respect to the base adsorbent, Zeolite 13X. The hypothetical adsorbents were assumed to have the same saturation capacity, $q_{\mathrm{s},i}$ and heat of adsorption, ΔH_i for both CO_2 and N_2; and adsorbent density (ρ_{s}) as that of Zeolite 13X. The isotherms for the hypothetical adsorbents were generated by varying the adsorption equilibrium constant, $b_{0,i}$ in the SSL model

for Zeolite 13X. A graphical approach was proposed to depict the relative positions of the hypothetical adsorbents in the context of isotherm non-linearity when compared to Zeolite 13X. The non-linearity plot shown in Figure 4.2, is for a binary system. The value of b_i of the strongly adsorbing species (CO_2) is represented in the Y axis and moving to the top of the plot would increase the non-linearity, similarly for the weakly adsorbing species (N_2) shown in X axis, moving towards the right would increase the non-linearity. Since the plot is generated with respect to the base adsorbent, point with the coordinate (1, 1) would correspond to the base adsorbent. Adsorbents with linear isotherms for both the species would be close to the bottom-left corner of the plot and adsorbents with non-linear isotherms for both the species would stay away from the origin in the top-right corner.

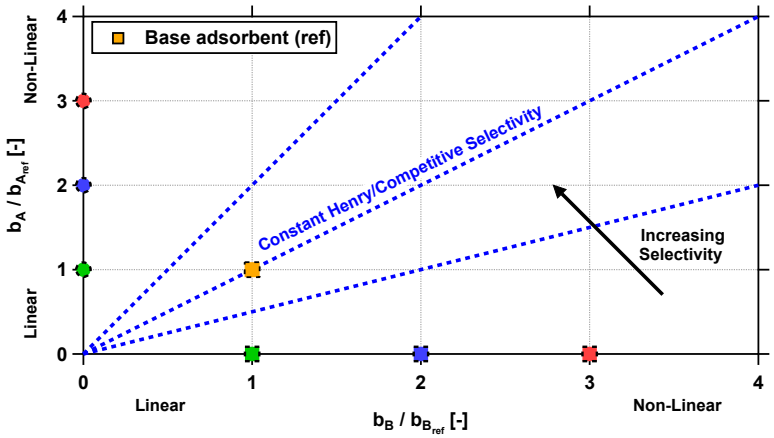

Figure 4.2: Non-linearity plot to represent the adsorption equilibrium constant b_i for a binary feed gas (A - strongly adsorbing species, B - weakly adsorbing species) with a constant $q_{s,i}$ and ΔH_i for different hypothetical adsorbents.

The adsorbents that lie on a line originating from the origin, shown by the blue dotted lines in Figure 4.2 are characterized by same selectivity. On the non-linearity plot, the selectivity of the adsorbents increases on moving from the bottom-right corner to the top-left corner. The adsorbents on the non-linearity plot are represented as MC_xN_y, where x is the ratio of b_{CO_2} to $b_{CO_{2,ref}}$ and y is the ratio of b_{N_2} to $b_{N_{2,ref}}$. For example Zeolite 13X, the base adsorbent is denoted as MC_1N_1 in the results discussed in chapter.

4.3 Test of selectivity, working capacity ratio and Yang's FOM

The Henry and competitive selectivity for Zeolite 13X (MC_1N_1) from the SSL model was found to be ≈ 365. The Henry selectivity using the SSL model was less than that obtained from a DSL model. This could attributed to the fact that the fit provided by SSL model was poorer than the DSL model. The Henry selectivity is the ratio of slopes of CO_2 to N_2 at very low pressures,

hence the accurate description of the equilibria at low pressure is critical in evaluating the Henry selectivity. The main focus of this work was to study the effect of the selectivity and isotherm non-linearity using hypothetical adsorbents, hence the relative trends observed for the performance of these adsorbents would remain unaffected by the differences observed in the Henry selectivity. As a word of caution, it wouldn't be wise to compare the process performance for Zeolite 13X reported in the previous chapter with the one presented in this chapter for the above mentioned reasons. Hereafter, selectivity would refer to Henry selectivity and competitive selectivity.

The objective of the first study was to explore whether adsorbents with the same selectivity would result in similar purity-recovery performances. Four different hypothetical adsorbents and Zeolite 13X (MC_1N_1) with a selectivity of 365 with different non-linearities for CO_2 and N_2 were considered. Depending on the non-linearity of the adsorbents, different adsorbents were placed in the non-linearity plot shown in Figure 4.3.

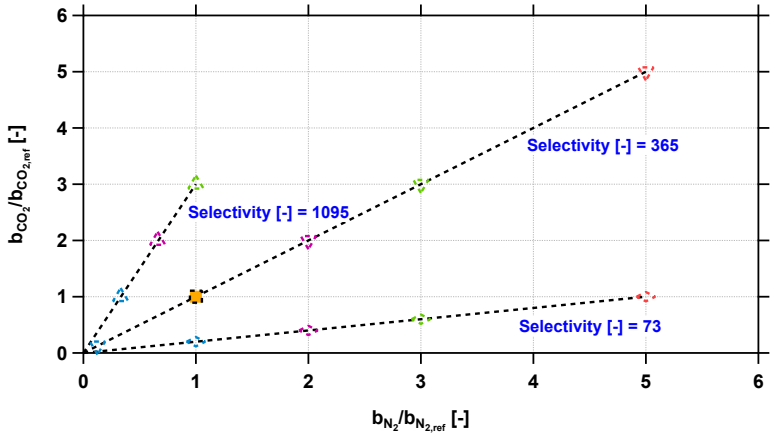

Figure 4.3: Relative position of the hypothetical adsorbents in the non-linearity plot with a selectivity of 73, 365 and 1095 considered for process optimization.

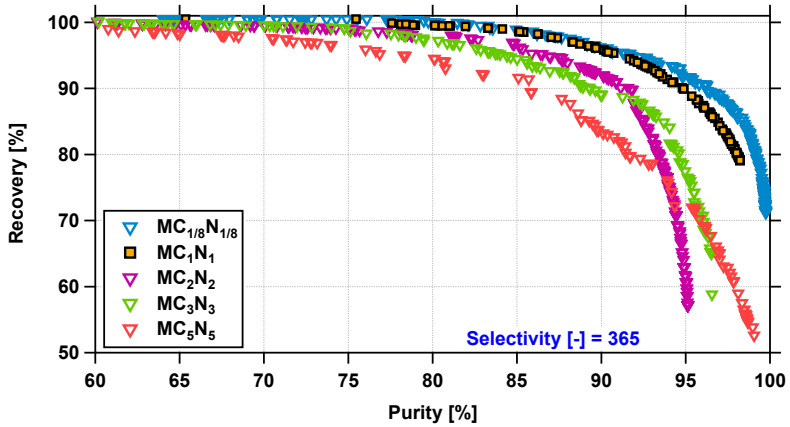

Figure 4.4: Purity-recovery optimization pareto curves for adsorbents with a selectivity of 365.

All the adsorbents were subjected to a multi-objective optimization to maximize purity and recovery simultaneously. The operating ranges for the step times, pressures and feed velocity used in the optimization routine were discussed in section 4.2. The purity-recovery pareto curves for Zeolite 13X and the four hypothetical adsorbents with a constant selectivity of 365 are shown in Figure 4.4. As seen from the figure, four of the five adsorbents were able to achieve purity and recovery in excess of 90%. The adsorbent MC_5N_5 was unable to achieve the target purity and recovery. It was clear from the pareto curves that the adsorbent, $MC_{1/8}N_{1/8}$ had the best performance over the entire range of purity and recovery. On moving from the bottom-left corner to the top-right corner of the non-linearity plot, the CO_2 and N_2 non-linearity for the adsorbents increases, while maintaining the same selectivity. The adsorbent MC_5N_5 had both a strong CO_2 and N_2 when compared to Zeolite 13X and it has been shown with the adsorbents discussed in chapter 3 that materials with strong N_2 affinity perform significantly poorer than the materials with a weak N_2 affinity. The observations from this study clearly indicates that adsorbents with the same selectivity need not necessarily have same or similar performances in terms of purity and recovery.

To understand the dynamics of the process, solid and fluid phase column profiles were obtained for a Zeolite 13X (MC_1N_1) and MC_5N_5. Single cycle simulation was performed at operating conditions corresponding to a recovery of 90% for both the adsorbents. At these conditions, purity of MC_1N_1 ($\approx 95\%$) was higher than MC_5N_5 ($\approx 86\%$). The intermediate and low pressure for the two adsorbents showed an interesting trend. The intermediate (P_{INT}) pressure and low pressure (P_{L}) for MC_1N_1 was 0.062 bar and 0.030 bar, respectively while it was 0.069 bar and 0.045 bar, respectively for the hypothetical adsorbent. The optimizer chose a higher P_{INT} for MC_5N_5 to restrict CO_2 losses in the blowdown step. Since the CO_2 affinity on the hypothetical adsorbent is more that of MC_1N_1, a small change in the pressure would desorb significant amount of CO_2 in the blowdown step. But downside of a higher P_{INT} is that the N_2 would contaminate the extract product during the evacuation step, and hence would result in a low purity CO_2 product. Similarly, MC_5N_5 could be used at a lower P_L, which would improve the CO_2 recovery but it would be achieved at the cost of desorbing more N_2 in the extract product and hence would result in a lower CO_2 purity. The CO_2 purity and recovery are defined as:

$$Pu_{\mathrm{CO_2}} = \left.\frac{n_{\mathrm{CO_2}}}{n_{\mathrm{CO_2}} + n_{\mathrm{N_2}}}\right|_{\mathrm{EVAC}} \tag{4.5a}$$

$$Re_{\mathrm{CO_2}} = \frac{n_{\mathrm{CO_2}}|_{\mathrm{EVAC}}}{n_{\mathrm{CO_2}}|_{\mathrm{ADS+FP}}} \tag{4.5b}$$

where, n_i is the number of moles of species i. The solid phase profiles for MC_1N_1 and MC_5N_5 along the length of the column evaluated at CSS at the end of the adsorption, blowdown and evacuation steps are shown in Figure 4.5. For the conditions at which the column profiles were

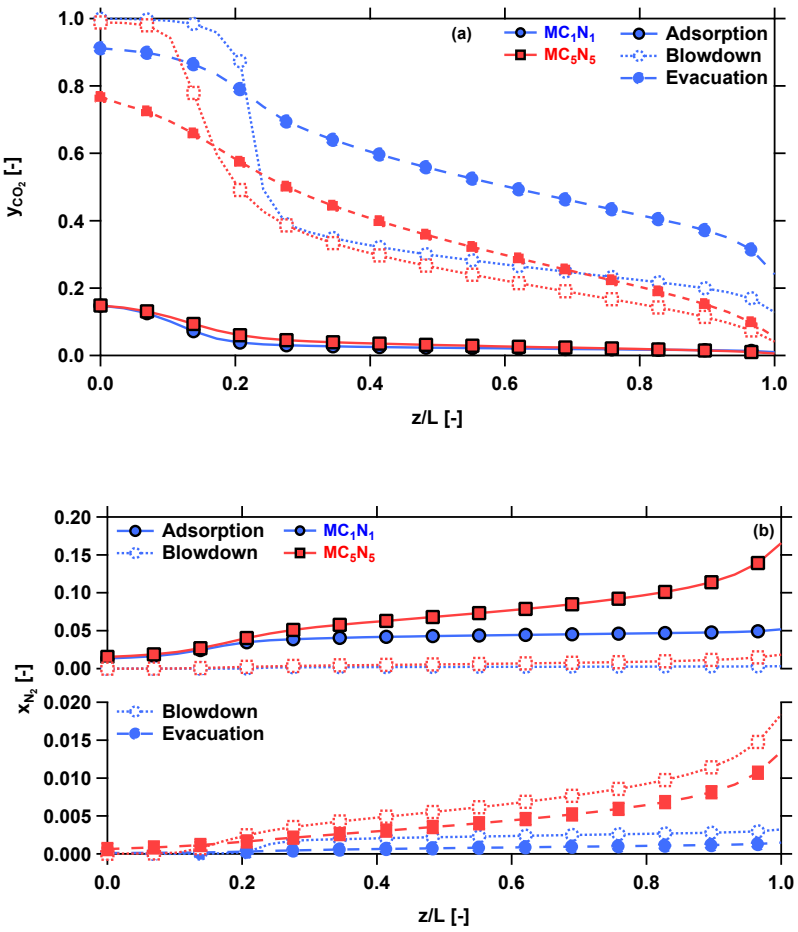

Figure 4.5: (a) CO_2 gas phase and (b) N_2 solid phase profile across the column at CSS for Zeolite 13X (MC_1N_1) and a hypothetical adsorbent (MC_5N_5).

obtained, the CO_2 recovery and moles of gas fed into the cycle were similar for both the adsorbents. Hence, from equation 4.5b, it is clear that for the two adsorbents the number of moles of CO_2 desorbed in the evacuation step is comparable. Thus, according to equation 4.5a, the CO_2 purity depends only on the moles of N_2 desorbed in the evacuation step. The area between the blowdown and evacuation curve in the N_2 solid phase profiles is the amount of N_2 desorbed in the evacuation step. Since, the area between the curves for MC_5N_5 was more than that of MC_1N_1, a contaminated product was obtained for MC_5N_5. And these observations led to a conclusion that the effect of the isotherm non-linearity and the constraints under which the process operates are crucial. Further, this study showed clearly that selectivity cannot be treated as a determinant of process performance, as it was clearly shown that even with the same selectivity, adsorbents with varying CO_2 and N_2 affinity can produce differing process performances.

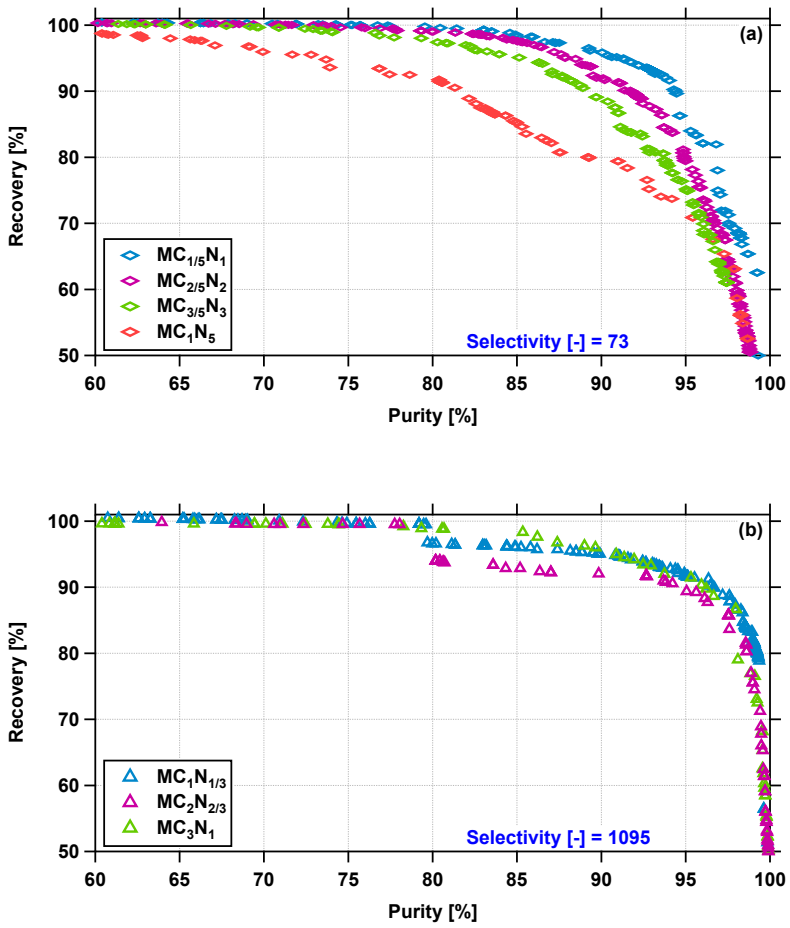

Figure 4.6: Purity-recovery optimization pareto curves for adsorbents with a selectivity of (a) 73 and (b) 1095.

Adsorbents with thrice (α_H = 1095) and one fifth (α_H = 73) the selectivity of MC_1N_1 (α_H = 365) were also subjected to purity-recovery maximization using process optimization. The motivation behind choosing adsorbents with different selectivities was to study the effect of selectivity on the carbon capture process as previous studies have emphasized that increasing the selectivity of the adsorbent towards the extract product enhances the process performance [47]. The adsorbents based on their isotherms were placed on the non-linearity plot shown in Figure 4.3. The purity-recovery pareto curves for the hypothetical adsorbents with a selectivity of 73 and 1095 are shown in Figure 4.6. It was interesting to note that the adsorbents with a selectivity of 1095 showed similar performances in terms of the maximum achievable purity and recovery, while the adsorbents with a selectivity of 73 showed a clear distinction in the performance. For adsorbents with low selectivity, since the adsorbent was relatively less selective towards CO_2 when compared to the reference case (MC_1N_1), attaining purity in excess of 90% was

difficult. With process constraints on the lowest bound for the intermediate and low pressures, removing N_2 in the blowdown step without losing out on the CO_2 recovery becomes impossible without making significant changes in the process configuration. Even with the low selectivity, adsorbents with weaker N_2 adsorption were able to meet the target purity and recovery, and as the N_2 isotherm became more sharper the performance was affected significantly. A detailed study will be presented in the succeeding section by fixing either the CO_2 or N_2 isotherm to understand the contribution from the non-linearities of individual species in the feed gas. The results from the study also showed that once the adsorbent was fairly selective towards CO_2 as seen for adsorbents with $\alpha_H = 1095$, the process performance remained unaffected with the changes in the non-linearity of both CO_2 and N_2 isotherms.

With the results discussed above, it is clear that the adsorbents with a linear CO_2/N_2 isotherm, i.e., on the bottom-left corner of the non-linearity plot exhibit the best performances in terms of purity and recovery. The energy consumption and productivity for the adsorbent cannot be obtained from the purity-recovery pareto curves. Hence in order to get a complete picture about the efficacy of an adsorbent, performing an energy-productivity optimization with a constraint on the purity-recovery is essential.

4.4 Test of fixed CO_2/N_2 isotherms

4.4.1 Effect of CO_2 isotherm

Four hypothetical adsorbents were considered such that they had the same N_2 isotherm parameters as MC_1N_1 (shown in Figure 4.7). The selectivity of the adsorbents varied between 73 and 1825 depending on the non-linearity of the CO_2 isotherm. The adsorbents were subjected to a purity-recovery optimization like all the other adsorbents discussed before. Contrary to what was expected, purity-recovery curves of the adsorbents overlapped upon increasing the CO_2 affinity by fixing the N_2 isotherm. Novel materials like metal organic frameworks have caught recent attention for carbon capture because of their high CO_2 adsorption capacity. Results from this particular case study shows that increasing the CO_2 affinity/capacity, which in turn would increase the CO_2 selectivity does not lead to a betterment in the process performance, atleast in terms of the achievable purity-recovery for the given separation problem. The differences in the non-linearities might have a significant impact on the productivity, but the productivity analysis is outside the scope of this work. It is important to note that there is a threshold for the CO_2 isotherm non-linearity beyond which separation becomes difficult because of the extreme rectangular nature of the isotherm. Due to a fixed lower bound for the operating pressures arising from process constraints, recovering CO_2 from the solid phase would be impossible without relaxing the pressures lower than the existing bounds in the optimization routine.

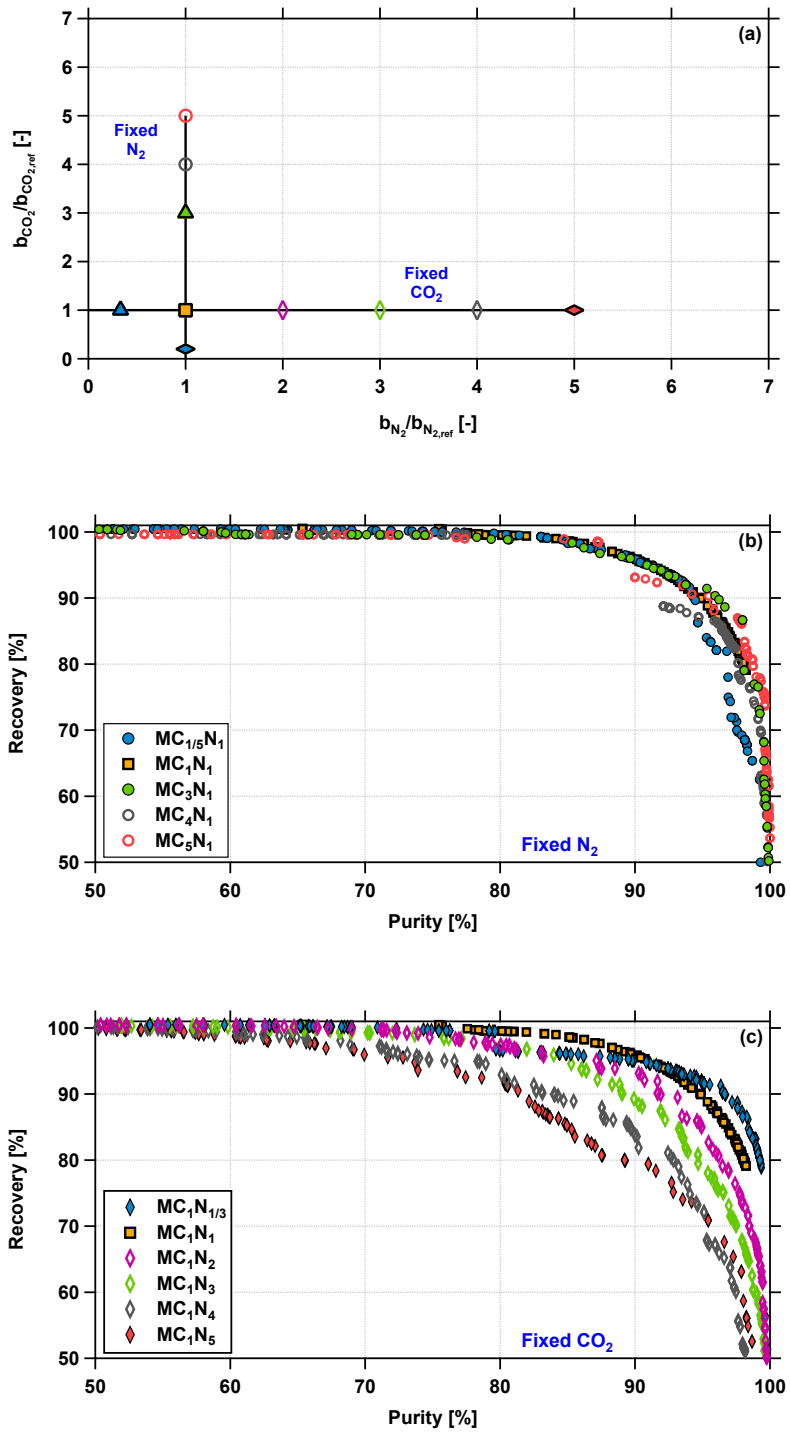

Figure 4.7: (a) Non-linearity plot for fixed CO_2/N_2 adsorbents and purity-recovery optimization pareto curves for adsorbents with a (b) fixed N_2 isotherm and (c) fixed CO_2 isotherm.

4.4.2 Effect of N_2 isotherm

An approach similar to the one discussed in the previous sub-section was employed with new set of hypothetical adsorbents, but in this study by fixing the CO_2 isotherm and varying the N_2 isotherm. The CO_2 isotherm parameters for MC_1N_1 were retained and the N_2 isotherm parameters were varied to make the isotherms for the hypothetical adsorbents more linear or non-linear with respect to MC_1N_1. The selectivity of the adsorbent would drop by increasing the N_2 non-linearity keeping the CO_2 isotherm fixed. The purity-recovery pareto fronts for the hypothetical adsorbents are shown in Figure 4.7. Unlike the case of fixed N_2 isotherm, where increasing the selectivity from 73 to 1825 did not improve the achievable purity-recovery, in the case of fixed CO_2 isotherm, the effect of the N_2 non-linearity was clearly visible. Among the adsorbents chosen, the adsorbent with the highest N_2 affinity performed the worst (MC_1N_5) and the observations assert the role of the N_2 isotherm on process performance. Difficulty in removing N_2 in the raffinate product step can be attributed to the poor performance of adsorbents with stronger N_2 affinities.

The purity-recovery pareto fronts obtained from the hypothetical adsorbents provided deeper insights into the role of selectivity and the isotherms on process performance. There is a clear boundary beyond which no matter the selectivity or the CO_2 adsorption affinity on the adsorbent, for the given capture system and process configuration achieving purity-recovery in excess of 90% is impossible. The results from fixed CO_2 and N_2 have defined boundaries for the maximum isotherm non-linearity that the individual species can enjoy without compromising on achieving the purity-recovery targets.

4.5 Minimum selectivity limit

In an ideal case, to selectively adsorb a component over an adsorbent, the selectivity of the adsorbent should be > 1. In the non-linearity plot, the lines that originate from the origin are iso-selective, i.e., the adsorbents have the same selectivity along a given line. Adsorbents on the iso-selectivity line corresponding to a selectivity of 1 will not be able to concentrate the CO_2 from 15% to a higher concentration. Like the boundaries for the maximum possible isotherm non-linearity for the concerned species discussed in the previous section, there also exits a minimum isotherm non-linearity and selectivity that the adsorbent must posses. And, since the target purity-recovery is in excess of 90%, there lies a selectivity contour corresponding to 90% purity and recovery below which the CO_2 cannot be concentrated enough to reach the targets. The selectivity contour will be referred to as the critical selectivity henceforth.

In order to define the boundary for the critical selectivity, five adsorbents with the same N_2

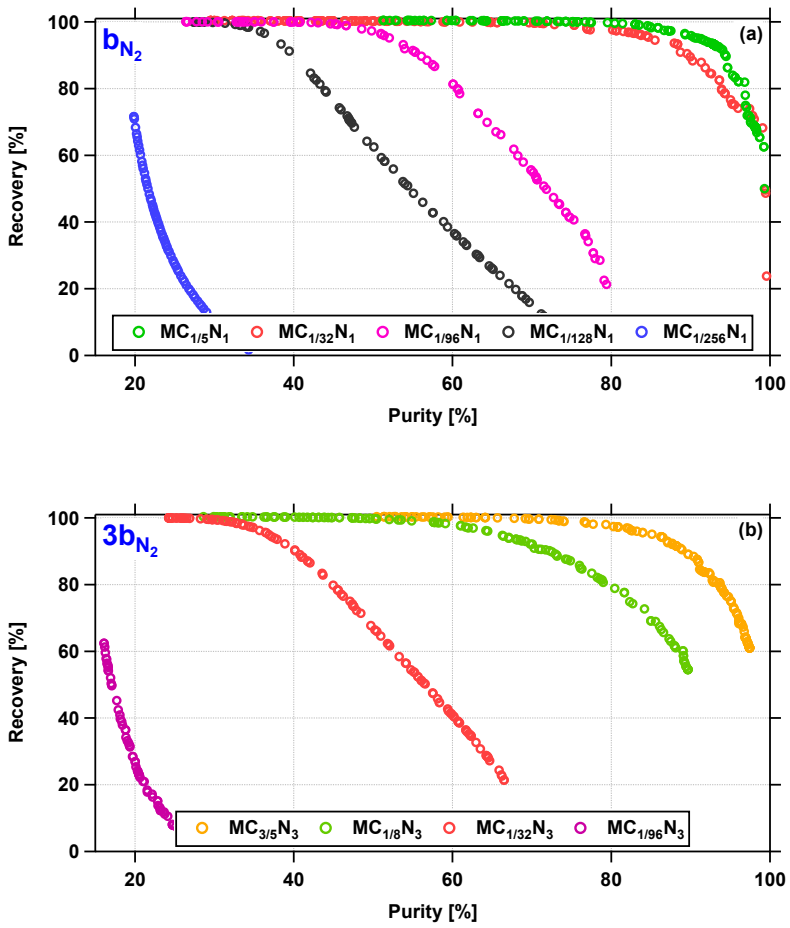

Figure 4.8: Purity-recovery optimization pareto curves for adsorbents with (a) MC_xN_1 and (b) MC_xN_3 N_2 isotherm parameters for the determination of the critical selectivity contour corresponding to 90% purity-recovery.

isotherm parameters as Zeolite 13X and four adsorbents with the same N_2 isotherm parameters as $3b_{N_2,13X}$ were considered. The CO_2 isotherm parameters were chosen such that the selectivity of the adsorbents varied from values close to 1 to a high enough selectivity such that the adsorbent was be able to satisfy the purity-recovery targets. The adsorbents were subjected to a purity-recovery optimization and the paretos are shown in 4.8. As expected for adsorbents with a very low selectivity ($MC_{1/256}N_1$ and $MC_{1/96}N_3$), the maximum achievable purity was $\approx$ 35% with a negligible CO_2 recovery in the extract product. But as the adsorbent became more selective towards CO_2, the pareto curves marched towards the 90% purity-recovery region, i.e., towards the top-right corner of the plot.

The pareto curves from Figure 4.8 were used to generate the critical selectivity contour. For adsorbents that were able to satisfy 90% recovery, two independent functional relations between

b_{CO_2} of b_{N_2} and $3b_{N_2}$; and purity corresponding to 90% recovery was found. Since, the grid was not fine enough to accurately find the b_{CO_2} for the two N_2 isotherms that would achieve the purity-recovery targets, this approach had to be used. Using the b_{CO_2} values obtained for b_{N_2} and $3b_{N_2}$, a quadratic function was fitted with these two points and the origin to generate the critical selectivity contour.

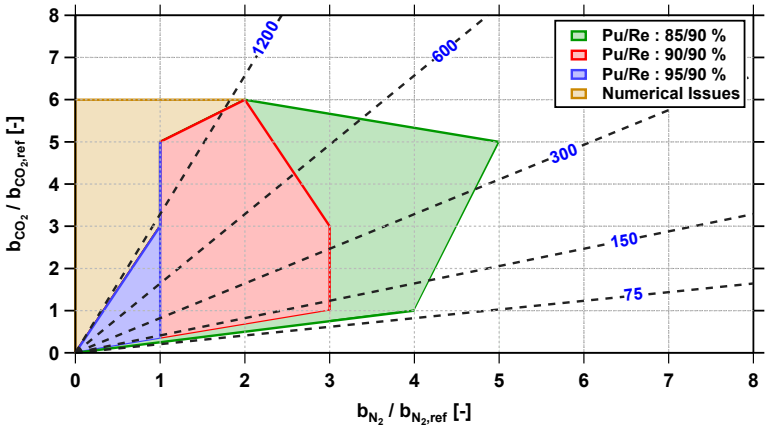

Figure 4.9: Non-linearity plot with the region showing the adsorbents that would satisfy 85/90, 90/90 and 95/90 % purity-recovery targets (blue, red and green) and the region with numerical issues (brown).

Using the boundaries defined in section 4.4 and the current section, a contour corresponding to adsorbents that satisfied 85/90, 90/90 and 95/90% purity-recovery were generated in the non-linearity plot and is shown in Figure 4.9. From the purity-recovery contours it is clear that maximum purity can be attained by moving towards the bottom-left corner of the non-linearity plot. Adsorbents with linear isotherms for both CO_2 and N_2 with a selectivity above the minimum selectivity limit is enough to achieve the purity-recovery targets, rather than having a very high selectivity or a high CO_2 adsorption capacity. It is worth noting that the contours generated here are just interpolations from the purity-recovery optimization results discussed in the preceding sections, and in order to get a complete picture, further purity-recovery optimization has to be carried out for adsorbents within the region which is represented as a region with numerical issues. Due to the extreme CO_2 isotherm non-linearity and selectivity for the adsorbents in the region marked in brown, we encountered numerical issues. For the adsorbents in this region, we would expect a better performance than the adsorbents which were explored and reported in the previous sections because of the weak N_2 adsorption. When the adsorbents were subjected to a purity-recovery optimization, a complete pareto curve was not obtained and contrary to what was expected, the adsorbents were unable to achieve recovery in excess of 90%. For a few sets of operating conditions, the closure of mass balance was not guaranteed, due to which breaks in the pareto curves were observed.

4.6 Preliminary energy analysis

In the previous sections, the performance of the hypothetical adsorbents were assessed based on their achievable purity-recovery for the given process. As discussed in the previous chapter, the purity-recovery pareto fronts does not provide information regarding the energy consumption and the productivity; and lower the energy consumption of an adsorbent, the better it is for the given separation process. Hence, the adsorbents which met the purity-recovery targets, i.e., in excess of 90% were subjected to a multi-objective optimization to minimize the energy consumption and maximize the productivity, simultaneously with constraints on the purity-recovery. The objective functions for the optimization problem were defined using equation 3.6. The decision variables used for the purity-recovery optimization were kept unchanged for the energy-productivity optimization.

Generating an energy-productivity pareto curve is a challenging task and the computational time in general is in the order of 7-10 days. The process involved dividing the entire decision variable domain into smaller sub-domains and performing a multi-objective optimization in each of these sub-domains. The pareto points from all the sub-domains were used as an initial population for the optimizer and the adsorbents were subjected to several shorter optimization runs to generate the entire pareto. It has been observed that for constrained optimization problems, the GA found it difficult to escape the local minima and using the approach mentioned enabled a thorough search over the entire decision variable space and has been found successful in generating complete energy-productivity paretos shown in chapter 3. Since, the energy-productivity analysis for the adsorbents is in the initial stage, only a preliminary overview of the expected trends for the energy consumption is presented.

The relative energy consumption for the different adsorbents are shown in the non-linearity plot in Figure 4.10. In the non-linearity plot the red closed marker is representative of the energy consumption for a given adsorbent. The size of the markers corresponds to the energy consumption obtained after performing the optimization. Smaller the markers, lesser is the energy consumption and hence, better is the adsorbent for the given capture process. With the limited results presented, a clear trend in the energy consumption was observed. Adsorbents with linear isotherm for CO_2 and weaker N_2 affinity consumed lesser energy than the adsorbents with non-linear CO_2 isotherm and stronger N_2 affinity in the adsorbent. The trends in the energy consumption were also observed in the achievable purity-recovery for the adsorbents. The observations from these curves have consistently placed the adsorbents with linear isotherms ahead of the ones with non-linear isotherms in terms of purity, recovery and energy consumption, i.e., adsorbents closer to the bottom-left corner of the non-linearity plot had the best performance.

The differences observed in the energy consumption were similar to energy-productivity pareto

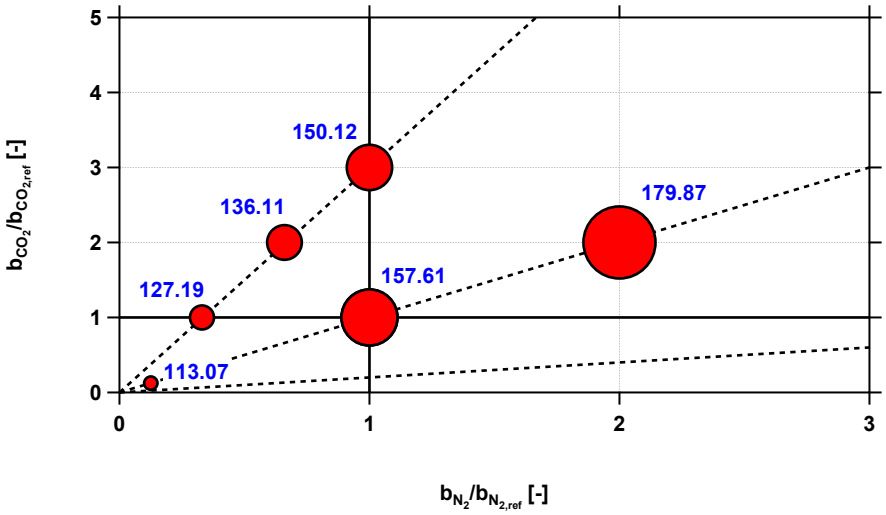

Figure 4.10: Energy consumption (closed markers) for individual adsorbents from preliminary energy-productivity optimization. Note that smaller the marker, lower the energy consumption and the value next to the markers are the minimum energy consumption in kWh/tonne CO_2 cap. for each adsorbent.

curves discussed in chapter 3. In order to understand the differences, the primary contributors to the energy consumption, intermediate pressure (P_{INT}) and low pressure (P_{L}) corresponding to the pareto points were plotted and are shown in Figure 4.11. From equation 3.7, it is clear that the energy consumption depends on the pressure range between which the vacuum pump operates. A vacuum pump operating at a higher outlet pressure would consume less energy. The low pressure (P_{L}) for all the adsorbents converge to the lower bound for P_{L}, i.e., 0.03 bar and hence seeing significant differences in the energy contribution from evacuation step would be difficult. It can be seen from Figure 4.10 and 4.11 that the hypothetical adsorbent $MC_{1/8}N_{1/8}$ consumed the least energy to achieve the target purity and recovery. The $MC_{1/8}N_{1/8}$ had the weakest N_2 affinity among all the adsorbents chosen for the energy analysis study, hence the removal of N_2 in the blowdown step was carried out at higher P_{INT} which resulted in a lower energy consumption. Similarly, the hypothetical adsorbent MC_2N_2 with the strongest N_2 affinity, had to operate at a lower P_{INT} to remove the N_2 and hence, consumed a higher energy. The trends in P_{INT} observed for different adsorbents were in agreement with the energy consumed by the process, i.e., an adsorbent with the highest P_{INT} had the least energy consumption and vice-versa.

The energy contribution of the constitutive steps in the 4-step PSA cycle with LPP corresponding to the minimum energy consumption for adsorbents considered for the energy analysis is shown in Figure 4.12 and the operating conditions at which the energy contribution was evaluated is given in Table 4.2. For a selectivity of 365, the energy contribution from the blowdown step for $MC_{1/8}N_{1/8}$ was 8.14 kWh/tonne CO_2 cap. ($\approx$ 7.20% of total energy consumption), while

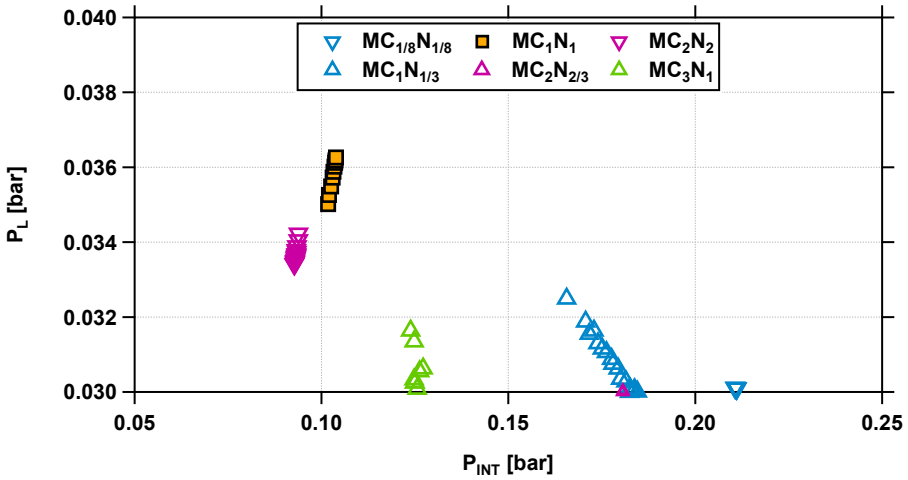

Figure 4.11: Intermediate pressure (P_{INT}) and low pressure (P_{L}) corresponding to the pareto points for Zeolite 13X and the hypothetical adsorbents obtained from preliminary energy analysis shown in Figure 4.10.

for MC_2N_2 was 49.76 kWh/tonne CO_2 cap. ($\approx$ 27.66% of total energy consumption). The key contributor to the trends observed in the energy consumption was the intermediate pressure at the end of the blowdown step which was due to differences in the N_2 affinity in different adsorbents. The preliminary energy analysis verifies the claims made in chapter 3, where it was shown that N_2 affinity plays a crucial role in the achievable performance in terms of purity, recovery and energy consumption.

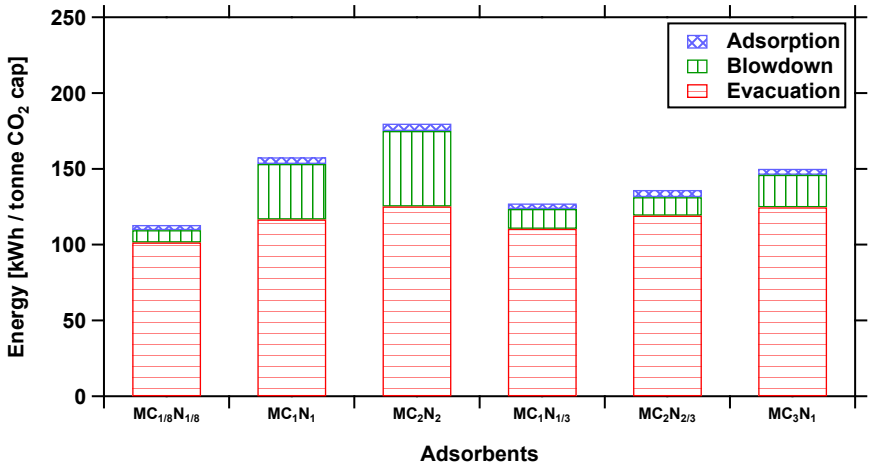

Figure 4.12: Energy contribution from constitutive steps corresponding to the minimum energy consumption for the hypothetical adsorbents with selectivity of 365 and 1095 that satisfy the purity-recovery constraints for the operating conditions given in Table 4.2.

Selectivity	Adsorbent	t_{ADS} [s]	t_{BLO} [s]	t_{EVAC} [s]	P_{INT} [bar]	P_L [bar]	v_0 [m s^{-1}]
365	$MC_{1/8}N_{1/8}$	40.35	66.83	54.32	0.211	0.030	0.73
	MC_1N_1	41.70	63.35	61.62	0.104	0.036	0.91
	MC_2N_2	41.14	68.25	58.50	0.094	0.034	0.99
1095	$MC_1N_{1/3}$	40.32	69.19	61.54	0.166	0.032	0.78
	$MC_2N_{2/3}$	42.09	69.10	61.82	0.181	0.030	0.98
	MC_3N_1	41.55	69.60	61.77	0.124	0.032	0.80

Table 4.2: Operating conditions corresponding to the minimum energy consumption with a 90% purity-recovery constraint for the adsorbents.

4.7 Conclusions

The main objective of the work presented in this chapter was to evaluate the process performances of adsorbents with different selectivity and pure-component isotherms for CO_2 and N_2. The performances were evaluated by performing rigorous optimization to maximize purity-recovery and minimize energy on Zeolite 13X and hypothetical adsorbents for post-combustion CO_2 from dry flue gas. The study provided deeper insights on the effect of selectivity and indicated that adsorbents with the same selectivity need to necessarily have the same performances. The Yang's FOM which seemed to provide the relative ranking of adsorbents in chapter 3, failed for the adsorbents considered in this chapter. The study was also able to clearly show that increasing the CO_2 affinity on an adsorbent does not help in improving the process performance. The impact of N_2 adsorption on the adsorbents was more dominating than the CO_2 affinity

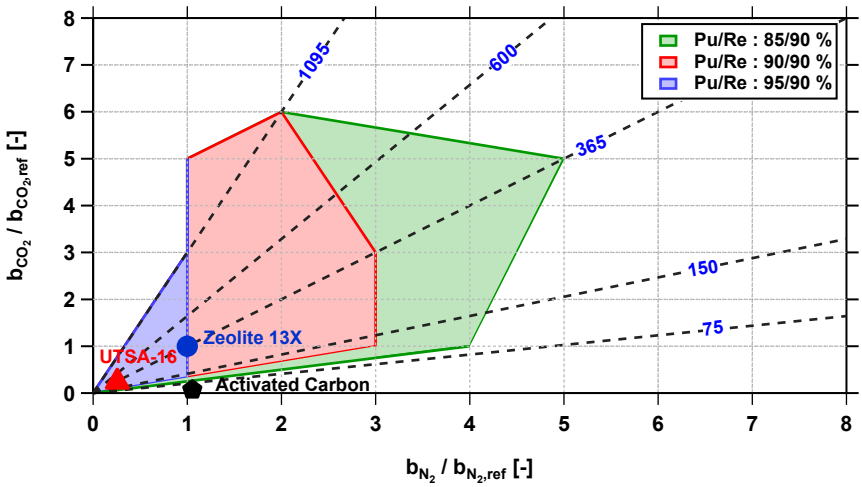

Figure 4.13: Relative position of Zeolite 13X, UTSA-16 and activated carbon on the non-linearity plot with purity-recovery contours (blue, red and green).

in the performance of a carbon capture process. The results from this chapter have reinforced the claims made on the effect of N_2 affinity on the energy consumption. The non-linearity plot proposed in this chapter was used to compare the performances of Zeolite 13X, UTSA-16 and activated carbon discussed in chapter 3. The non-linearity plot was able to predict the performance of the three real world materials and is shown in Figure 4.13. UTSA-16 with a linear isotherm of CO_2 and lower affinity for N_2 was in the region corresponding to a purity/recovery of 95/90%. While activated carbon was below the minimum selectivity limit corresponding to a purity/recovery of 85/90% and hence had the worst performance. With the limited study conducted in this chapter, the effectiveness of using the non-linearity plot is showing promising results for adsorbent screening. Once a detailed study is conducted by varying the saturation capacity and the heat of adsorption for the CO_2 and N_2, the non-linearity plot presented, would be extremely useful as it has the potential to direct the chemists towards synthesizing materials with desirable isotherms which could eventually have a superior performance than the existing materials for carbon capture.

Part II

Pre-combustion CO_2 capture

Chapter 5

PSA cycle design for pre-combustion CO_2 capture using TDA-AMS-19

5.1 Introduction

Pre-combustion CO_2 capture is a carbon capture technology, where the CO_2 is captured before being fully combusted. Unlike a post-combustion CO_2 capture system which could be applied to a conventional coal-fired power plant, the pre-combustion CO_2 can be implemented only in integrated gasification combined cycle (IGCC) based power plants. In an IGCC based power plant (shown in Figure 5.1), the coal is chemically broken to produce syngas which is primarily carbon monoxide (CO) and hydrogen (H_2). The syngas is converted to pre-combustion CO_2 gas stream constituents, namely carbon dioxide (CO_2) and hydrogen (H_2) by the water-gas shift (WGS) reaction. Impurities like hydrogen sulfide (H_2S) and water are removed and the gas mixture of CO_2 and H_2 is processed in a CO_2 capture system to remove CO_2. After the removal of CO_2, the H_2 is used as a fuel to generate electricity in a gas turbine combustor combined cycle [61].

Capturing CO_2 from this stream is of paramount importance and various regulatory bodies set targets in excess of 90% for CO_2 purity and recovery. Compared to a traditional post-combustion CO_2 capture process, IGCC based power plants provide better conditions in terms of CO_2 composition (40%) and the operating pressure ($\approx$ 35 bar) of the process that could favor CO_2 capture. One of the main challenges of a pre-combustion based CO_2 capture stems from the fact that IGCC is not widely used in the power industry around the world. This chapter

This work was performed in collaboration with TDA Research Inc., Wheat Ridge, Colorado, U.S.A.

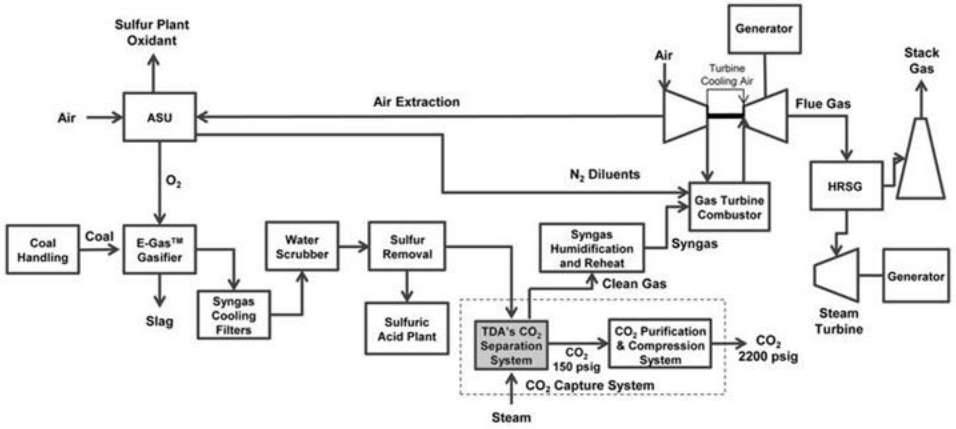

Figure 5.1: IGCC power plant with CO_2 capture system (the dotted box indicates current project scope).

explores the potential of a pre-combustion CO_2 capture system using a pressure swing adsorption technology (PSA) to meet the process performance targets set by the regulatory bodies.

5.2 Experimental setup for measuring equilibrium isotherms

Adsorption equilibria is a key input parameter for the process simulation. The isotherms for CO_2 on AMS-19 were measured at three different temperatures over a wide of range of pressure. The isotherms were obtained using by performing breakthrough experiments on the setup shown in Figure 5.2. Thermocouples were aligned along the length of the column to measure temperature across the adsorbent bed. The CO_2 concentration was monitored on-line using two analyzers, namely, NOVA multi-gas analyzer and Vasiala CO_2 probes. To characterize the dead volumes in the system (A+B+D+E+Drierite+Analysers), experiments were conducted by passing an inert gas through the bypass line rather than the column. The dead volumes present in the column might increase the retention time in the system or broaden the adsorption/desorption curves observed at the analyzer. The responses obtained from breakthrough experiments are often used to evaluate equilibrium and kinetic parameters and it is important to take into account the extra-column effects when the breakthrough responses are analyzed. The dead volumes were corrected using a point by point (PBP) method where the true response in the column is given as

$$t_{\mathrm{TR}} = t_{\mathrm{CR}} - t_{\mathrm{BR}} \tag{5.1}$$

where, t_{TR}, t_{CR} and t_{BR} are the true column response, composite response and blank response, respectively. The PBP method assumes that the band retention time and band broadening are linearly additive between the composite and blank response, which might have potential consequences in the evaluation of equilibrium and mass transfer parameters [62].

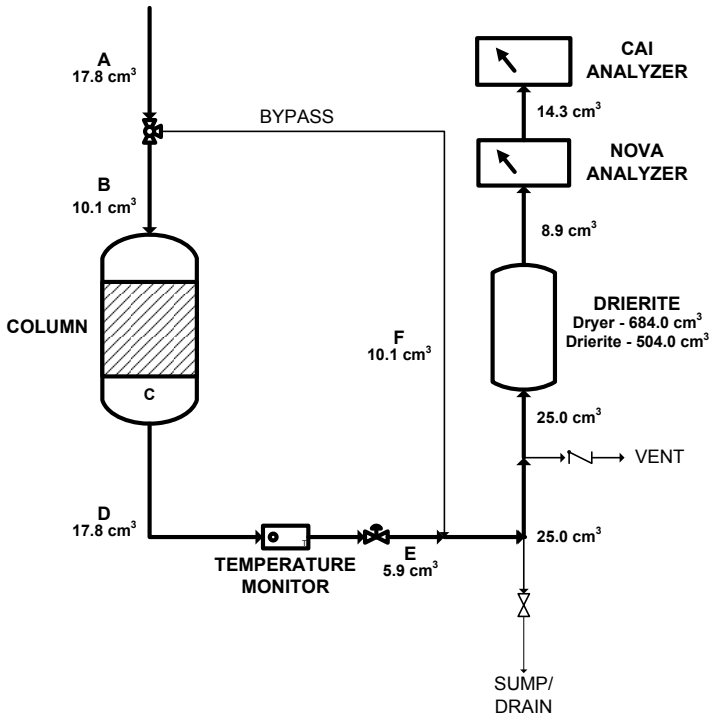

Figure 5.2: Breakthrough apparatus setup used to obtain the CO_2 isotherm on TDA-AMS-19 adsorbent.

The breakthrough experiments involve an adsorption and a desorption experiment and the typical adsorption and desorption curves obtained from these experiments are shown in Figure 5.3. The moles of the gaseous species accumulated in the solid and gas phase can be obtained from the adsorption and desorption curves, which can be used to calculate the equilibrium solid phase loading in the adsorbent for a given component at the experimental temperature and pressure. It is to be noted that the moles accumulated in the column is calculated using the true response curve after correcting for the dead volumes present in the system. In the present system, the moles of CO_2 accumulated in the column is given as follows:

$$n_{\mathrm{CO_2,ADS}} = \int_{t=0}^{t=t_{\mathrm{ADS}}} \left(Q_{\mathrm{in}} C_{\mathrm{in}} - Q_{\mathrm{out}} C_{\mathrm{out}}\right) dt \tag{5.2a}$$

$$n_{\mathrm{CO_2,DES}} = \int_{t=0}^{t=\infty} \left(Q_{\mathrm{out}} C_{\mathrm{out}}\right) dt \tag{5.2b}$$

where, Q and C are the molar flow-rates and concentration, respectively. The shaded region in Figure 5.3 gives the amount of CO_2 accumulated in the column in both solid and fluid phases. The heat of adsorption (ΔH_{ads}) for CO_2 on TDA-AMS-19 was provided by TDA Research Inc. ΔH_{ads} was found to be ≈ 20.5 kJ/mol and was measured using differential scanning calorimetry (DSC).

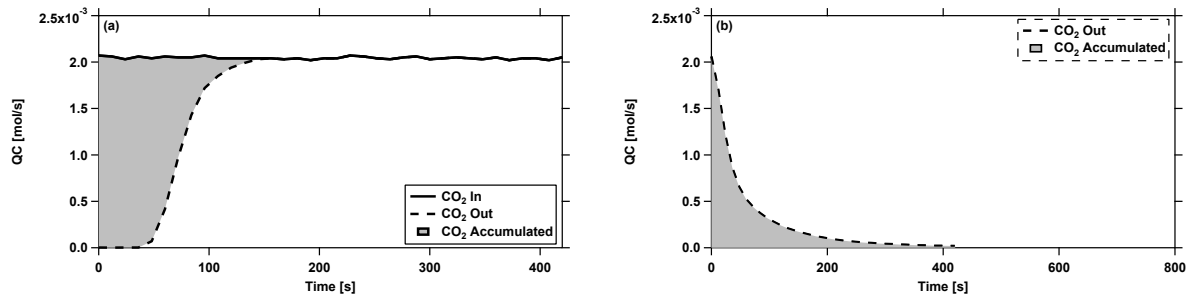

Figure 5.3: (a) Adsorption and (b) desorption curves for a 100% CO_2 with He as a carrier gas on TDA-AMS-19 at 1 bar and 120°C.

The experimental adsorption equilibrium data for CO_2 on TDA-AMS-19 adsorbent was provided by TDA Research Inc., at three different temperatures viz. 180°C, 240°C and 300°C (Figure 5.4) using the approach discussed above. Several isotherm models were considered to describe the equilibrium data, and the Sips isotherm model, discussed in Chapter 2 was selected since it provided a better fit at low pressures regions.

The Sips isotherm (Eq. 2.7) consists of eight parameters (ω_i, φ_i, θ_i, ϕ_i, $s_{1,i}$, $s_{2,i}$, T_{ref}, $s_{\mathrm{ref},i}$). The experimental data from the breakthrough experiments were fitted for the isotherm parameters simultaneously by nonlinear regression at the experimental temperatures. Figure 2 shows the fitted isotherm and the experimental data at the given temperatures (180°C, 240°C and 300°C) for CO_2.The hydrogen isotherm was not available on TDA-AMS-19, hence the Sips isotherm parameters for H_2 on activated carbon were obtained from the literature [63]. Note that the literature data corresponds to H_2 adsorption on activated carbon and therefore should be treated with caution. Figure 5.4 shows the single component isotherm for CO_2 and H_2 while Table 5.1 lists the corresponding isotherm parameters for the two components. The process simulations discussed further in this chapter involves multiple components and the competition between the mixture species needs to be accounted for in the simulations. Since multi-component experimental data was not available, single component parameters were retained and it was assumed that they can reliably predict multi-component behavior for the given conditions using the extended Sips isotherm model discussed in Chapter 2.

	ω_i [mol kg^{-1}]	φ_i [kJ mol^{-1}]	θ_i [Pa^{-1}]	ϕ_i [kJ mol^{-1}]	$s_{1,i}$ [-]	$s_{2,i}$ [-]	$s_{\mathrm{ref},i}$ [-]	T_{ref} [K]
CO_2	3.74	-7.87	26.9×10^{-9}	-2.05	0.136	0.110	0.760	281
H_2	6.66	0	0.7×10^{-9}	-9.83	0	0	0.956	273

Table 5.1: Single component Sips isotherm parameters for CO_2 and H_2

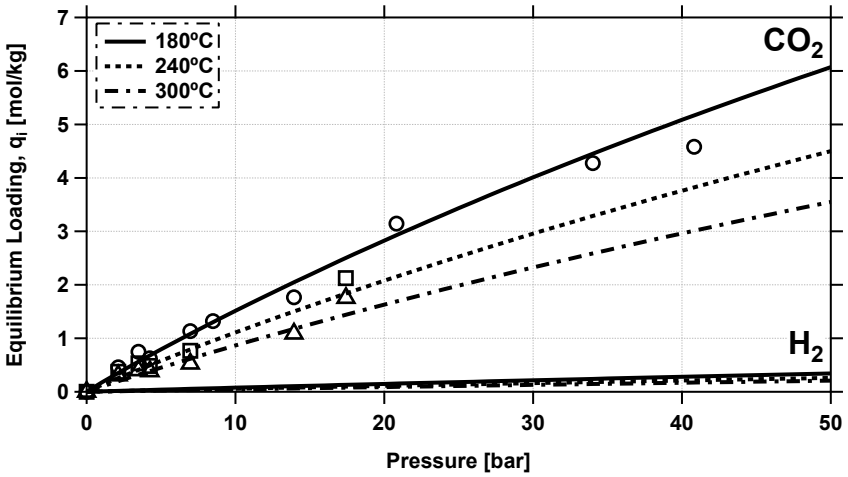

Figure 5.4: Single component Sips isotherms for CO_2 (fitted to TDAs equilibrium data) and H_2 (obtained from literature for actiavted carbon) at the experimental temperatures. Symbols are experimental values and the solid lines represent the Sips isotherm fit for 180°C (circles), 240°C (sqaures) and 300°C (triangles).

5.3 PSA cycle modeling

Different PSA cycle configurations were considered for the the pre-combustion CO_2 on TDA-AMS-19. Most PSA cycles used in the work consist of a feed pressurization, adsorption, co-current blowdown and a counter-current blowdown step. The basic 4-step PSA cycle discussed in chapter 2 was modified to come up with different process cycle configurations. The operating pressure range for the PSA cycle was a constraint on the process and it was provided by TDA Research Inc. The PSA cycles were operated between a high pressure, P_{H} and low pressure, P_{L} of 34.45 bar and 10.00 bar, respectively; and a feed gas temperature of 240 °C. The performance of the PSA cycles discussed in this section is given by the following key performance metrics viz. purity and recovery:

$$Purity, Pu(CO_2) = \frac{\text{Total moles of } CO_2 \text{ in extract product in one cycle}}{\text{Total moles of gas in extract product in one cycle}} \times 100 \tag{5.3}$$

$$Recovery, Re(CO_2) = \frac{\text{Total moles of } CO_2 \text{ in extract product in one cycle}}{\text{Total moles of } CO_2 \text{ fed into the column in one cycle}} \times 100 \tag{5.4}$$

$$Purity, Pu(H_2) = \frac{\text{Total moles of } H_2 \text{ in raffinate product in one cycle}}{\text{Total moles of gas in raffinate product in one cycle}} \times 100 \tag{5.5}$$

$$Recovery, Re(H_2) = \frac{\text{Total moles of } H_2 \text{ in extract product in one cycle}}{\text{Total moles of } H_2 \text{ fed into the column in one cycle}} \times 100 \tag{5.6}$$

Parameter	Value
Column properties	
Column length, L [m]	0.61
Inner column radius, r_{in} [m]	5.12×10^{-2}
Bed voidage, ϵ [-]	0.40
Particle voidage, ϵ_{p} [-]	0.57
Particle radius, r_{p} [m]	3.00×10^{-4}
Fluid and Adsorbent properties	
Syngas pressure, P_{feed} [bar]	34.50
Adsorbent density, ρ_{s} [kg m^{-3}]	1361.00
Specific heat capacity of gas phase, $C_{\text{p,g}}$ [J kg^{-1} K^{-1}]	1010.60
Specific heat capacity of adsorbent, $C_{\text{p,s}}$ [J kg^{-1} K^{-1}]	1877.20
Fluid viscosity, μ [kg m^{-1} s^{-1}]	2.15 x 10-5
Molecular diffusivity, D_{m} [m^2 s^{-1}]	4.81 x 10-8
Effective gas thermal conductivity, K_{z} [J m^{-1} K^{-1} s^{-1}]	0.09
Inside heat transfer coefficient, h_{in} [J m^{-2} K^{-1} s^{-1}]	0
Universal gas constant, R [m^3 Pa mol^{-1} K^{-1}]	8.314
Operating conditions for PSA cycles	
Feed composition (CO_2/H_2), y_{feed} [-]	0.40/0.60
High pressure, P_{H} [bar]	34.50
Low pressure, P_{L} [bar]	10.00
Feed temperature, T_{feed} [°C]	240.00
Purge gas temperature, T_{pur} [°C]	200.00
Interstitial feed velocity, v_{feed} [m s^{-1}]	0.10
Interstitial purge velocity, v_{pur} [m s^{-1}]	0.30

Table 5.2: Simulation parameters for PSA cycle modeling

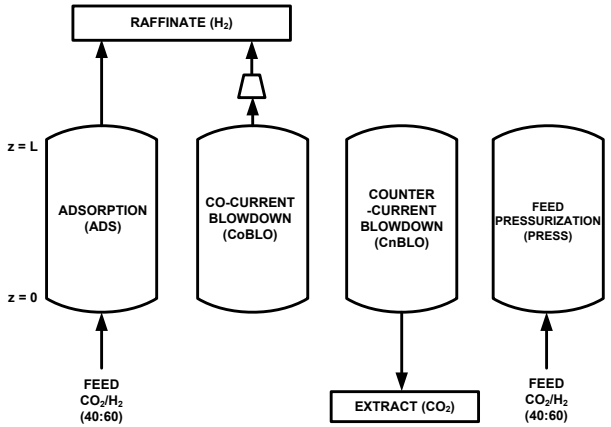

(a) Basic 4-step PSA cycle

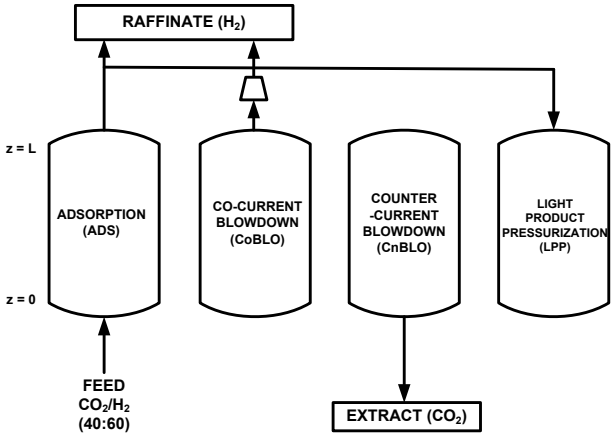

(b) 4-step PSA cycle with light product pressurization (LPP)

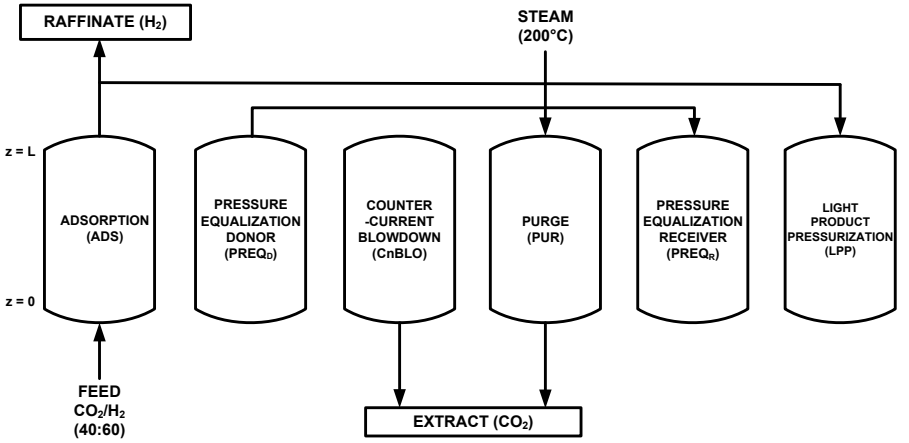

(c) 6-step PSA cycle with purge and pressure equalization (PE) and LPP

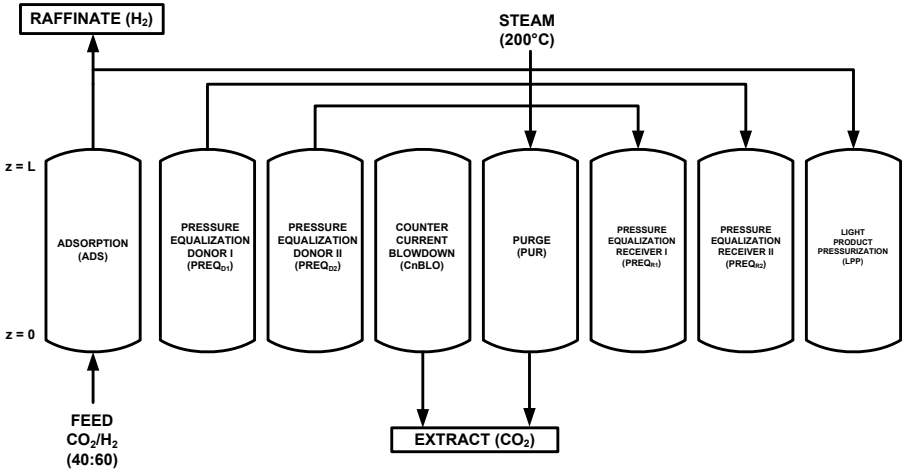

(d) 8-step PSA cycle with purge, two pressure equalizations (PE) and LPP

Figure 5.5: Process schematics for different PSA cycle configurations studied in the work

	t_{ADS} [s]	t_{CoBLO} [s]	t_{CnBLO} [s]	t_{PRESS} [s]	t_{PUR} [s]	t_{PREQ1D} [s]	t_{PREQ2D} [s]	P_{INT1} [bar]	P_{INT2} [bar]
A	40	45	95	20	-	-	-	12.0	-
B	40	45	95	t_{LPP}	-	-	-	12.0	-
C	40	-	95	t_{LPP}	20	45	-	21.8	-
D	40	-	95	t_{LPP}	20	15	30	25.5	17.5
E	40	-	95	t_{LPP}	20	45	-	21.8	-

Table 5.3: Process conditions (step times and intermediate pressures) for the different PSA cycle configurations shown in 5.5 (Configuration E refers to PSA cycle with co-current blowdown step (shown in 5.11))

5.3.1 Configuration A: Basic 4-step PSA cycle

A basic 4-step cycle was designed and a full cycle simulation was performed using the simulation parameters mentioned in Table 4 until the process reached cyclic steady state (CSS). The model was able to simulate the dynamics of the column and provide detailed gas phase, solid phase and temperature profiles across the column. The individual step times chosen for the four steps in the process are not optimized times at this point in the project (given in Table 5.3). In this cycle the H_2 product was obtained from the adsorption and the co-current blowdown step (Figure 5.6). The H_2 product thus obtained from the co-current blowdown step at an intermediate pressure required a compressor to raise the pressure of the raffinate stream from an intermediate pressure to high pressure for further processing. The simulation resulted in a CO_2 purity and recovery of ≈84 and ≈10 %, respectively (further details are summarized in 5.4). At the conditions for which the basic cycle was simulated, it was found that CO_2 was lost both in adsorption and co-current blowdown steps which were primarily raffinate product steps. From the CO_2 solid phase profile it was clear that at the end of the adsorption step (ADS), the bed was completely saturated at feed composition and CO_2 was breaking through the column (See Figure 5.6 ADS step) which eventually led to the loss of CO_2. This is also shown in Figure. 6, which shows the cumulative CO_2 collected at the end of each step. It can be noted that the amount of CO_2 collected at the end of the adsorption step for CO_2 was more than the CO_2 collected during the evacuation

PSA cycle configuration	CO_2		H_2	
	Purity [%]	**Recovery [%]**	**Purity [%]**	**Recovery [%]**
A	84.8	10.2	62.3	98.7
B	84.9	13.4	63.0	98.3
C	75.2	99.9	99.9	77.7
D	80.5	99.9	99.9	83.6
E	93.3	99.3	99.6	95.1

Table 5.4: Summary of purity/recovery for CO_2/H_2 for the different PSA cycle configuration reported (Table. 5.3). Performance indicators for cycles C, D and E are reported on dry basis

step (CO_2 product step), hence confirming the loss of CO_2 in the adsorption step. The losses in the co-current blowdown step can be attributed to the fact that the intermediate pressure (12 bar) was close to the low pressure (10 bar). Since the CO_2 isotherm is fairly linear for the given system, lower intermediate pressures or intermediate pressure closer to the low pressure are not recommended as this would lead to a significant CO_2 loss in the co-current blowdown, and this was exactly what was observed in the current cycle configuration. The raffinate product end of the column was contaminated with CO_2 (CoBLO) and led to reduction of H_2 purity (≈63% reported in Table 5.4) and CO_2 recovery.

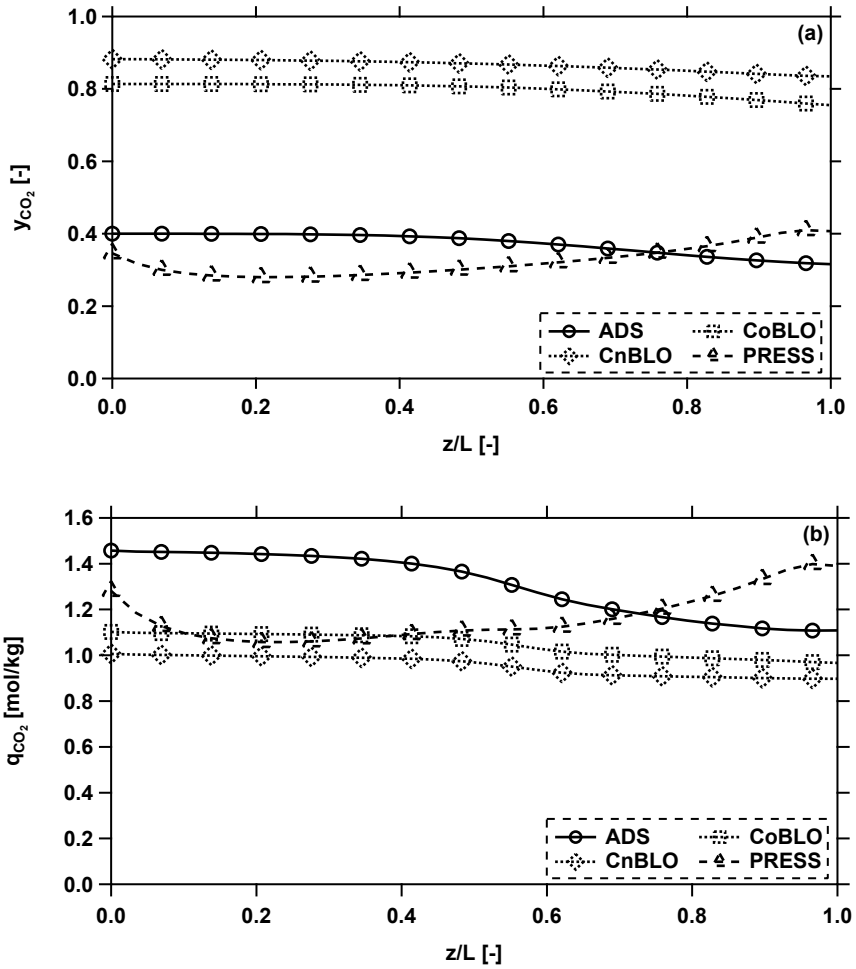

Figure 5.6: CO_2 (a) gas phase and (b) solid phase profile along the bed for basic 4-step PSA cycle for the conditions listed in Table 5.3

The other shortcoming of this cycle was that at the end of each cycle, the bed was not completely regenerated for fresh feed gas as observed in the CnBLO solid phase profile (Figure 5.6). As the counter-current blowdown pressure ($P_L = 10$ bar) was rather high, a process constraint, the CO_2

working capacity was low. These observations led to a modification in the cycle configuration, intending to reduce the CO_2 losses from the adsorption step.

5.3.2 Configuration B: 4-step PSA cycle with light product pressurization (LPP)

In configuration B, the feed pressurization step in the basic 4-step cycle was substituted with a light product pressurization (shown in Figure 5.5b) using the outlet gas stream from the adsorption step. The outlet stream from the adsorption step was used to pressurize the column from the H_2 product end (z=L). The LPP step was modeled using a data buffer, where the adsorption stream velocity, composition and temperature profiles as a function of time were stored in a buffer and then they acted as the inlet conditions to the LPP step. The LPP step was limited by the high pressure of the system, i.e., the gas from the adsorption outlet was used to pressurize the column till the pressure reached high pressure (P_H) in the column. Once the high pressure was reached, the adsorption outlet stream was collected as a raffinate product. If the desired high pressure was not attained by LPP, an extra feed pressurization would have been used. The rationale behind implementing a LPP step was to reduce the CO_2 losses from the adsorption step. The LPP step reduced CO_2 losses when compared to the basic 4-step cycle (shown in Figure 5.7) from the adsorption step but at the expense of H_2 recovery as part of H_2 was also fed back into the column.

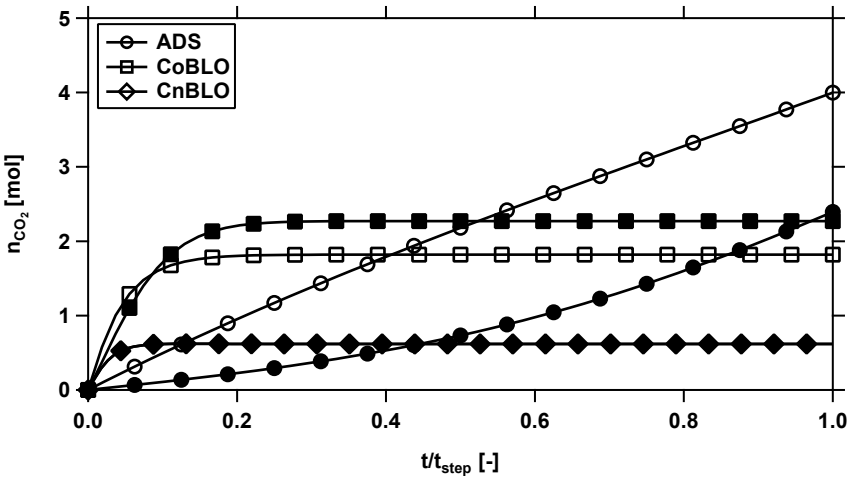

Figure 5.7: Cumulative amount of CO_2 collected at the end of adsorption, co-current and counter-current blowdown steps for basic 4-step PSA cycle (open symbols) and 4-step PSA cycle with LPP (closed symbols).

A full cycle simulation was performed for the new cycle configuration and as expected the CO_2 from the adsorption step was reduced when compared to the basic 4-step cycle (Figure 5.7)

and the cycle resulted in a minor increase in the CO_2 recovery. However this also led to a lower H_2 recovery as part of the H_2 product was used to pressurize the column. The addition of the LPP step would push the CO_2 front towards the z=0 end thereby reducing CO_2 losses in the subsequent steps. The conditions (listed in Table 5.3) chosen for this configuration were similar to the basic 4-step cycle conditions. These conditions were chosen in order to eliminate pressurizing the column using feed gas and since the time of adsorption was high (t_{ADS} = 40s), CO_2 brokethrough the column and contributed to losses in the adsorption step. But even with the addition of a LPP step in the cycle, the CO_2 recovery was low and this can be attributed to a higher intermediate (P_{INT} = 12 bar) and low pressure (P_L = 10 bar) in the process, which led to significant CO_2 losses in the co-current blowdown step and the bed in this configuration too wasn't completely regenerated for the feed step. The major short-comings of the cycle with LPP were the CO_2 losses from the co-current blowdown and the incomplete regeneration of the bed for the adsorption step. These losses from the co-current blowdown step can be overcome by either increasing the intermediate pressure of the process or by implementing a pressure equalization step and the bed can be regenerated by the addition of a purge step after the counter-current blowdown step. The 4-step cycle with LPP was hence modified and a 6-step PSA cycle was developed which is discussed in the next sub-section.

5.3.3 Configuration C: 6-step PSA cycle with purge, pressure equalization (PE) and light product pressurization (LPP)

The 4-step cycle with LPP was modified to a 6-step PSA cycle (shown in Figure 5.5c) to include a low pressure steam purge steam to have a CO_2 free bed for the fresh feed gas step and single pressure equalization to reduce the losses from the co-current blowdown step.

Purge step: A low-pressure purge step was added to the existing 4-step cycle with LPP. The purge gas was super-heated steam, and it was assumed to be a non-adsorbing gas in the process simulations. The basis for introducing a purge step was that the purge gas would extract the CO_2 remaining in the bed after the counter-current blowdown step and hence would help enhance CO_2 recovery. The purge step was also treated as an extract product step along with the counter-current blowdown step. The purge outlet stream is a wet product stream and the performance metrics reported are on dry basis.

Pressure equalization step: The blowdown step in the 4-step PSA cycle with LPP was substituted with a pressure equalization step. The pressure equalization step involved a donor and a receiver column, wherein the donor column was depressurized and the receiver column was pressurized using the gas from the donor. Addition of a pressure equalization step in the process eliminated the need for a compressor to pressurize the raffinate product to high pressure. The other advantage of introducing the pressure equalization step was that the CO_2 losses that were

observed in the cycles discussed before were reduced as the outlet stream from the donor column was used to pressurize the column and the CO_2 lost in the donor column was recycled back into the column. However, the introduction of the pressure equalization step led to the intermediate pressure in the system to be a dependent variable which can no longer be arbitrarily fixed. Since, the intermediate pressure is no longer a decision variable, H_2 recovery can be affected by the pressure levels (P_H and P_L) in the process.

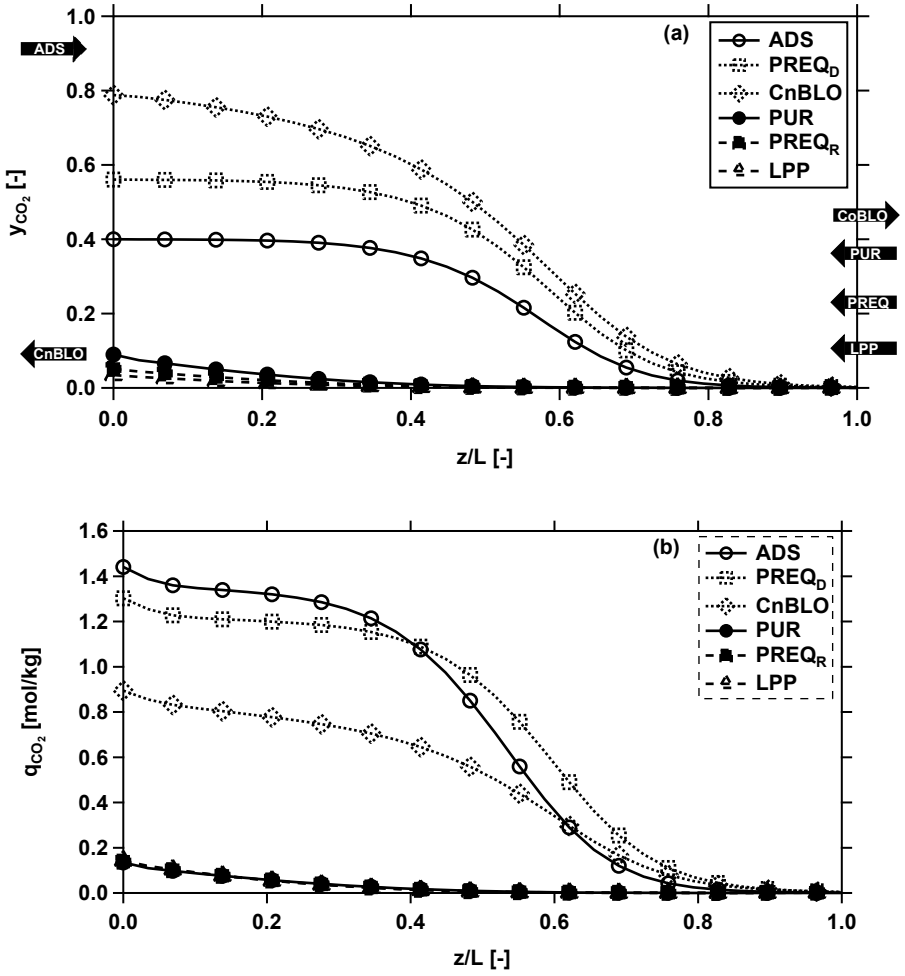

Figure 5.8: CO_2 (a) solid phase and (b) gas phase profile along the bed for the 6-step PSA cycle with purge, PE and LPP for the conditions listed in Table 5.3 (the arrows at the ends of the figures indicate the direction of flow).

Simulation results from 6-step PSA cycle with purge, PE and LPP: A full cycle simulation was run for the new cycle configuration until cyclic steady state was reached. The modifications in the cycle proved beneficial in improving the performance metrics when compared to the two cycles discussed in the previous subsections. The substitution of the co-current

blowdown with a pressure equalization decreased the CO_2 purity (≈75%) and this was a result of the high intermediate pressure for the pressure equalization step (P_{INT} = 21.8 bar). At these pressure levels, less H_2 was removed and it ended up contaminating the extract product from the counter-current blowdown step. This was confirmed by the gas phase profiles (Figure 5.8a), where the extract product end (z=0) had significant amount of H_2 and since H_2 was lost in the extract product step, it also resulted in reduced H_2 recovery. For the current cycle configuration, as the intermediate pressure was fixed by the pressure equalization constraint, for these high and low pressure levels, it would be difficult to increase the H_2 recovery significantly.

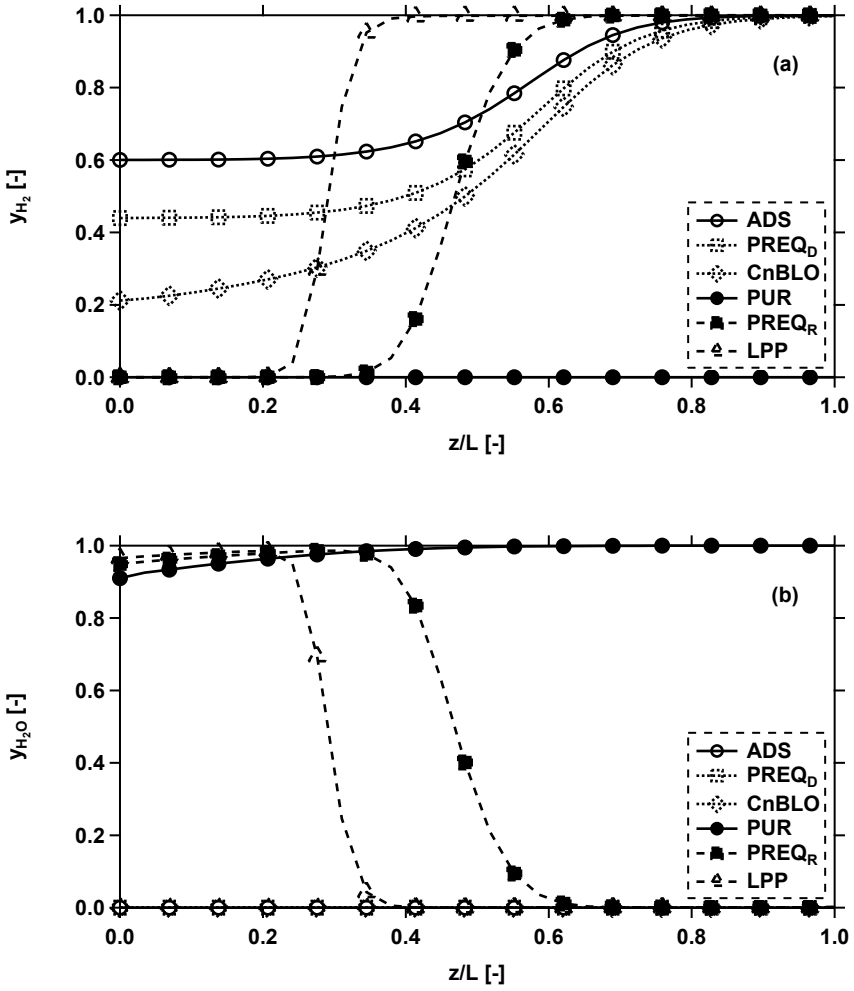

Figure 5.9: (a) H_2 and (b) H_2O gas phase profile along the bed for the 6-step PSA cycle with purge, PE and LPP at CSS for the conditions listed in Table 5.3.

On the other hand, the addition of a purge step in the process increased the CO_2 recovery by removing the remaining CO_2 from the solid phase by the end of the purge step. The raffinate

product end (z=L) of the column (shown Figure 5.9a) was not contaminated by the extract product (CO_2), and hence CO_2 was not lost in the raffinate product step (ADS in Figure 5.9a) and it led to pure H_2 being obtained. After the purge step, CO_2 and H_2 were present in trace amounts in both the solid and the gas phases. The third component, i.e., steam, being weakly adsorbing was present in the gas phase and the column was saturated with steam at the end of purge step (PUR in Figure 5.9b). The steam which remained in the gas phase was removed during the adsorption step and after the removal of the steam, pure H_2 product was obtained. The addition of the purge step regenerated the bed completely and the working capacity of CO_2 improved when compared to the cycles discussed before. However, the 6-step PSA cycle provided a lower CO_2 purity and H_2 recovery when compared to the previous two cycles. The main drawback of the 6-step PSA cycle with single PE arises from the rather high intermediate pressure ($P_{\mathrm{INT}} = 21.8$ bar) which was reached when compared to the cycles (Configuration A and B) where this pressure can be fixed a priori. At these conditions, H_2 was not completely removed before the counter-current blowdown step and significant amounts of H_2 contaminated the extract product end and in turn the CO_2 product.

5.3.4 Configuration D: 6-step PSA cycle with purge, two pressure equalizations (PE) and light product pressurization (LPP)

The 6-step PSA cycle with reversed counter-current blowdown step was able to achieve high CO_2 purity (≈93.3%) and recovery (≈99.3%) but at the expense of spending energy to compress the H_2 product obtained during the counter-current blowdown step. The basis behind reversing the direction of counter-current blowdown step was to remove more H_2 without losing out CO_2 in the raffinate product step. Enrichment of CO_2 to higher purities can also be attained by the addition of an extra pressure equalization step to the existing base 6-step PSA cycle (Figure 5.5c). The addition of an extra pressurization step would improve the process performance without any additional recompression for the raffinate product.

Implementation of pressure equalization: The 8-step PSA cycle (Figure 5.5d) had two pressure equalization steps and hence there were two intermediate pressures which were to be determined to satisfy the mass balance constraints (as in the 6-step PSA cycle). The first donor column was depressurized from a high pressure (P_{H}) to an intermediate pressure ($P_{\mathrm{INT_1}}$) and the second column was depressurized from an intermediate pressure, ($P_{\mathrm{INT_1}}$) to the second intermediate pressure ($P_{\mathrm{INT_2}}$). The desorbed moles from both the donor columns were collected in two separate tanks and were used to pressurize the two receiver columns from P_{L} to $P_{\mathrm{INT_1}}$ and $P_{\mathrm{INT_1}}$ to $P_{\mathrm{INT_2}}$. The constraints discussed in the implementation of pressure equalization for the 6-step PSA cycle were also taken care in the 8-step cycle and a local optimization was performed to determine the intermediate pressures in the process. The objective was to minimize

the difference between the moles flowing in and out of the two tanks with the intermediate pressures in the two pressure equalization steps as the decision variables and two empirical relations were obtained to approximate the intermediate pressures.

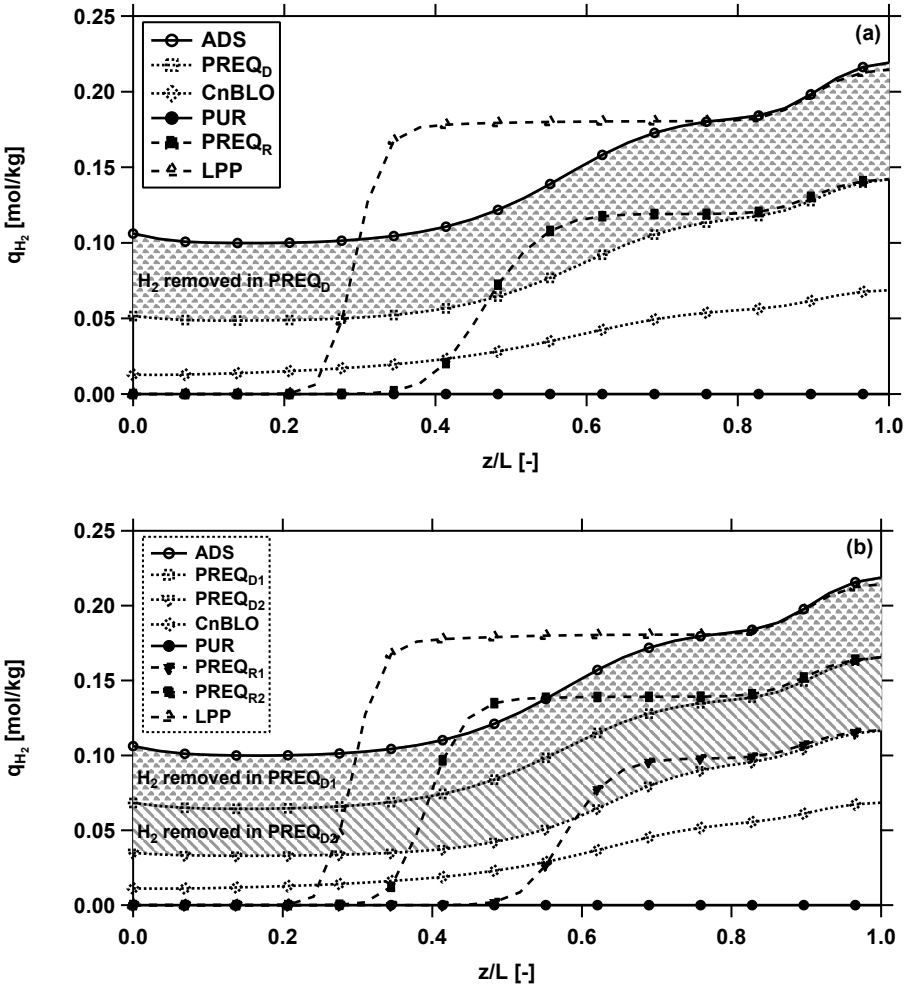

Figure 5.10: Comparison of H_2 solid phase profiles between PSA cycles with (a) 1PE and (b) 2PE, with $P_{\mathrm{INT}} = 21.8$ bar for 1PE and $P_{\mathrm{INT}_1}/P_{\mathrm{INT}_2}$ for 2PE = 25.5/17.5 bar (shaded area represents H_2 collected in pressure equalization step).

Effect of extra pressure equalization step on the 6-step PSA cycle: The 8-step PSA cycle was able to improve the CO_2 purity (≈80%) by removing more H_2 in the pressure equalization steps. The intermediate pressure at the end of the co-current blowdown step for the 8-step PSA cycle was found to be 17.5 bar, while for the 6-step PSA cycle the intermediate pressure at the end of the co-current blowdown step was 21.8 bar. A lower intermediate pressure for the 8-step cycle led to the removal of more H_2 and saturating the bed with H_2 at the raffinate product end while enriching CO_2 at the extract product end. The solid phase profiles for H_2 were

obtained for both the 6 and the 8-step PSA cycle (Figure 5.10). The amount of H_2 desorbed in the two cycles during the pressure equalization steps, given by the shaded region confirmed that the H_2 desorbed in the pressure equalization steps for the 8-step PSA cycle (donor column) was significantly higher when compared to the 6-step PSA cycle. Similarly, it was also observed that the amount of H_2 present as an impurity in the CO_2 product stream (represented by the blank area below CoBLO and $CoBLO_2$ profile in Figure 5.10) was smaller for the 8-step PSA cycle reflecting a higher CO_2 purity for this cycle. Identical process conditions and step times for the 6-step and 8-step cycles gave H_2 recoveries of 77.70% and 83.58% respectively. The addition of extra pressure equalization, i.e., a third pressure equalization step is expected to improve the H_2 recovery but further detailed studies would be performed in the future to quantify the effect of the third pressure equalization on the process performance.

5.3.5 Configuration E: 6-step PSA with purge, PE, LPP and co-current blowdown

One alternative to improve the Configuration C is to change the direction of the counter-current blowdown step. Reversal of the counter-current blowdown step into a co-current blowdown step, removed the H_2 which remained in the bed at the end of the pressure equalization step (donor column). H_2 was removed from the raffinate product end (z=L) and at the end of the co-current blowdown step, H_2 front moved to the raffinate product end and the extract product end (z=0) was rich in CO_2 (Figure 5.11). This led to pure CO_2 being obtained during the purge step which was the CO_2 product step in the new configuration and it was reflected by comparatively higher CO_2 purities ($\approx$93%). This can be best explained by considering the H_2 solid phase profiles and in turn the amount of H_2 being removed in the CO_2 product steps, which is given by the shaded region in Figure 5.11. For, the cycle with counter-current blowdown, the amount of H_2 present in the CO_2 product stream (shown as dashed and dotted area in Figure 5.11) was higher than the amount of H_2 in the CO_2 product stream in the reversed counter-current blowdown PSA cycle (dotted in Figure 5.11).

In the base 6-step PSA cycle, the H_2 product was obtained only from the adsorption step which was at high pressure (P_H), while the CO_2 was obtained at low pressure (P_L) from the counter-current blowdown and purge steps. This configuration eliminated the need of a compressor for the raffinate product as this product was obtained at high pressure (P_H), the pressure at which H_2 must be delivered for further processing. When the direction of counter-current blowdown step was changed for the new cycle configuration, H_2 product was obtained at two different pressures (P_H from adsorption step and P_L from counter-current blowdown step).

As mentioned before, the H_2 product needs to be delivered at P_H, hence extra costs would be associated with setting up and operating a compressor to compress the H_2 product from P_L to

P_H. Prior to deciding whether the 6-step PSA cycle with reversed counter-current blowdown step would be a viable option, a thorough energy-productivity study would be required. Nevertheless, in terms of purity/recovery the 6-step PSA cycle with reversed counter-current blowdown step was found to be promising for the given process and process conditions.

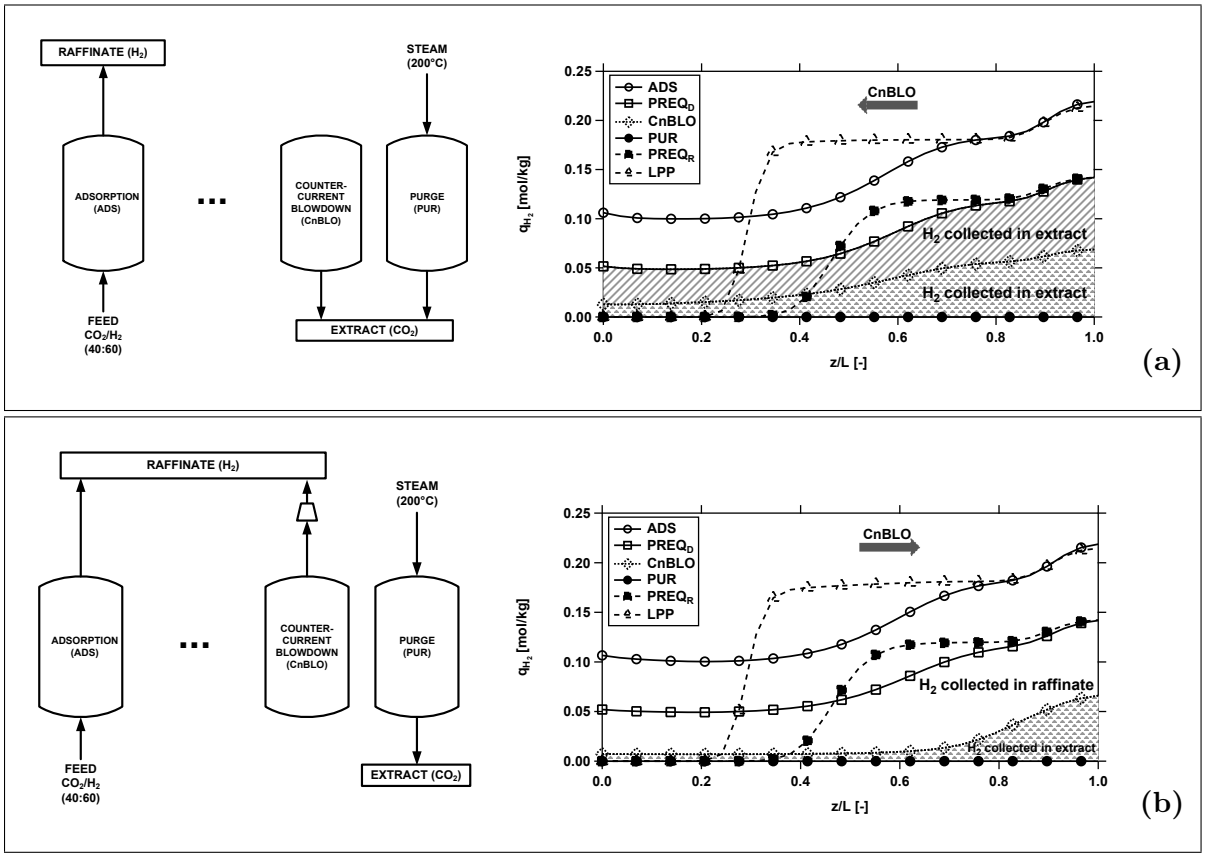

Figure 5.11: Process schematics and H_2 solid phase profiles for (a) 6-step PSA cycle base case and (b) 6-Step PSA cycle with reversed counter-current blowdown step (shaded area represents the H_2 collected in the extract stream and the arrows represent the direction of the counter-current blowdown step).

5.4 Conclusion

In this work, the main focus was to design preliminary PSA cycles for the pre-combustion capture of CO_2 using TDAs AMS-19 adsorbent. The adsorption equilibrium was described for CO_2 using experimental adsorption data on AMS-19 provided by TDA Research Inc., using the Sips isotherm model. H_2 isotherm parameters on activated carbon obtained from the literature [63] were used to design preliminary PSA cycles. The DOE sets a minimum CO_2 recovery target of 90% while CO_2 purity is expected to be in excess of 95%. A detailed one dimensional model was

developed in-house using Finite Volume Method (FVM) to describe the adsorption dynamics in the column. Mass, momentum and energy were considered for all the steps in a PSA process and full cycle simulations were performed for different PSA cycle configurations. The simulations were computationally fast (3-4 minutes for full cycle simulations) and were able to predict the gas and solid phase column profiles and the temperature profiles, which were obtained by solving partial differential equations over the entire time and space domain. The performance indicators, namely the purity and recovery for CO_2 and H_2 were calculated at the end of each cycle simulation, i.e., at the cyclic steady state. The preliminary PSA cycles were designed to

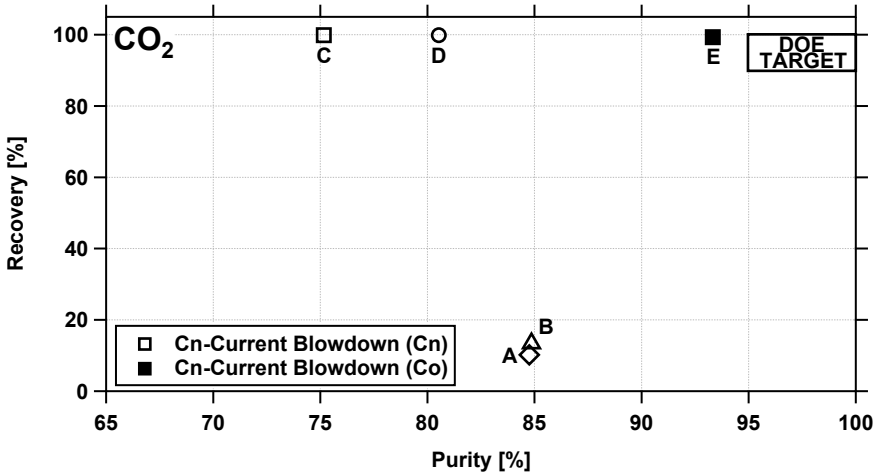

Figure 5.12: Cycle performance for CO_2 for the different PSA cycles reported in this work (Markers corresponds to cycles shown in Figure 5.5).

get as close as possible to the DOE targets. The study started with simple cycles to understand the process, but the simple cycles required additional compressors and compression energy to compress the products for further processing. To avoid additional compressors, a 6-step PSA cycle with pressure equalization and a purge step was designed. The counter-current blowdown direction in the 6-step PSA cycle was reversed and the modified cycle performed better than all the cycles reported in Figure 5.5 in terms of CO_2 purity and recovery (Figure 5.12). The process conditions used for the PSA cycle simulations were not optimized for performance metrics (Pu/Re) but further cycle optimization studies including energy consumption and productivity will have to be carried out to have a complete performance characterization. Dynamic column breakthrough (DCB) experiments of CO_2, H_2 and the mixtures will have to be modeled in the future to analyze the mass and heat transfer effects. Since, steam is being used in the process, the H_2O adsorption isotherms and DCB modeling would be necessary for complete description of the process. On the context of PSA cycle modeling, the modified 6-step PSA cycle with reversed counter-current blowdown step was able to hit 100% CO_2 recovery, but further cycle optimization and modification (addition of third pressure equalization step and reflux steps) in the PSA cycles to reach the DOE purity targets for CO_2 will have to be carried out.

Chapter 6

Concluding remarks

6.1 Conclusions

This thesis dealt with sorbent selection and process design for two different adsorption based carbon capture technologies. In the first part of the thesis, four different adsorbents reported in the literature were subjected to a purity, recovery, energy consumption and productivity analysis for a post-combustion CO_2 capture and were ranked accordingly using the performance metrics. Finally, hypothetical adsorbents were tested to asses the adsorption equilibria effects of CO_2 and N_2 on a post-combustion CO_2 capture. In the second part of the thesis, pressure swing adsorption (PSA) cycles for pre-combustion CO_2 capture were designed to separate CO_2 and H_2, and concentrate the CO_2 from 40 mol % to $\geq$ 90% in the product while achieving 90% recovery. Different PSA cycle configurations with pressure equalization and steam purge steps were investigated to achieve the purity and recovery targets for CO_2.

In Chapter 2, modeling and process optimization of a PSA cycle was presented. Different pure and competitive adsorption equilibria models like single-site Langmuir isotherm, dual-site Langmuir isotherm, and Sips isotherm used in Chapters 3, 4 and 5 were discussed. A rigorous one-dimensional model with the constitutive mass, momentum and heat balances was presented. A finite volume based discretization using van-Leer flux limiter was used for the constitutive equations and the resulting ordinary differential equations were integrated an in-built solver in MATLAB. The model was validated using a basic 4-step PSA cycle with adsorption, desorption and re-pressurization steps, by analyzing the fluid and solid phase profiles across the column and guaranteeing mass balance closure for the concerned species in the feed gas mixture. An overview of process optimization using genetic algorithm (GA) was presented. The merits and demerits of using a genetic algorithm and the GA input parameters like the number of generations, population size and the stopping criteria for the optimization routine were discussed.

The first part of the thesis focused on a process optimization based adsorbent screening for post-combustion CO_2 capture. In chapter 3, four adsorbents namely Zeolite 13X, two metal organic frameworks, Mg-MOF-74 and UTSA-16; and an activated carbon were subjected to multi-objective optimization to maximize purity and recovery simultaneously, and minimize energy consumption and maximize productivity for a 4-step PSA cycle with light product pressurization (LPP). The process optimization studies were able to key insights on the ability of adsorbent metrics like selectivity, working capacity and various figures of merit to predict process performance. It was seen that out of the ten commonly used adsorbent metrics, only the ranking of adsorbents provided by pure selectivity and Yang's FOM agreed with the trends obtained from a full cycle process optimization. It was shown from the purity-recovery studies on hypothetical adsorbents and energy-productivity analysis on Mg-MOF-74, Zeolite 13X and UTSA-16, that the ability of an adsorbent in rejecting N_2 played a far more decisive role than the ability of an adsorbent to have a high adsorption capacity or selectivity.

The objective of chapter 4 was to take the key observations and understandings from chapter 4 a step forward by performing process optimization studies on hypothetical adsorbents to test the effect of adsorbent selectivity and non-linearity of CO_2/N_2 isotherms. The non-linearity of CO_2 and N_2 isotherms on the hypothetical adsorbents were illustrated using as a non-linearity plot. Pure component selectivity and Yang's FOM which seemed to rank the adsorbents discussed in chapter 3, failed to rank the hypothetical adsorbents. It was clear from the results discussed in the second part of the thesis that none of the adsorbent metrics were able to reliably rank adsorbents and even though adsorbent screening using process optimization was computationally intensive, it was able to quantitatively rank the adsorbents based on the performance indicators.

Chapter 5 dealt with the process design for pre-combustion CO_2 capture. The feed for the capture system was a 40/60 % mixture of CO_2/H_2 at 35 bar and 240 °C. Adsorption equilibrium data for CO_2 were measured at three different temperatures by TDA, the industrial partner for the project on TDA-AMS-19, a surface modified activated carbon based adsorbent. The adsorption equilibria for CO_2 was defined using a extended Sips isotherm model. The adsorption equilibrium data for H_2 on TDA-AMS-19 was unavailable, hence the isotherm parameters on an activated carbon were obtained from literature and were used in the designing the process. Five different PSA cycle configurations were considered ranging from the a basic 4-step PSA cycle to an 8-step PSA cycle with purge and two pressure equalization steps. The 6-step PSA cycle with a pressure equalization purge step in which the direction of the counter-current blowdown step had the best performance in terms of the achievable purity and recovery. The cycles were optimized neither for purity-recovery nor for energy-productivity and the main objective of the chapter was to understand the dynamics of the different PSA cycles to reach the sequestration targets using TDA-AMS-19.

6.2 Outlook

The work has resulted in providing directions towards screening adsorbents and designing processes for adsorption based CO_2 capture. Using the one-dimensional non-isothermal and non-isobaric model coupled with a multi-objective optimization routine, operating conditions that could maximize purity, recovery, productivity and minimize energy consumption can be determined. Adsorbent screening using process optimization and PSA cycles designed for pre-combustion CO_2 capture have shown promising results to reach the sequestration targets, but there are several subjects which are untouched and further investigation would be required.

In the domain of adsorbent screening for post-combustion CO_2 capture, the results from the initial studies have firmly established the effect of the CO_2 and N_2 isotherms on process performance. The studies presented were conducted by varying the adsorption equilibrium constant, while the effect of the saturation adsorption capacity, and the heats of adsorption for the concerned species in the flue gas needs to incorporated in the non-linearity plot. These attempts to complete the non-linearity plot would eventually bridge the gap between adsorbent synthesis and process design. Finally, different cycle configurations would have to be tested to exploit the potential of adsorbents to maximize their performance.

For the process of pre-combustion CO_2 capture, it is necessary to describe the adsorption equilbria for H_2 and H_2O on TDA-AMS-19. Adsorption of mixtures on the adsorbent is critical in understanding the behavior of the syngas on the process and the accuracy of the extended Sips isotherm model. On the context of PSA cycle modeling to get a complete process performance characterization, studies in the future should focus on modifying and optimizing the existing cycles.

Bibliography

[1] D. Luthi, M. Le Floch, B. Bereiter, T. Blunier, J.-M. Barnola, U. Siegenthaler, D. Raynaud, J. Jouzel, H. Fischer, K. Kawamura, *et al.*, "High-resolution carbon dioxide concentration record 650,000–800,000 years before present," *Nature*, vol. 453, no. 7193, pp. 379–382, 2008.

[2] A. Neftel, H. Friedli, E. Moor, H. Ltscher, H. Oeschger, U. Siegenthaler, and B. Stauffer, "Historical CO_2 record from the siple station ice core. in trends: A compendium of data on global change.," tech. rep., Carbon Dioxide Information Analysis Center, Oak Ridge National Laboratory, U.S. Department of Energy, Oak Ridge, Tenn., U.S.A., 1994.

[3] B. Metz and I. P. on Climate Change. Working Group III., *Carbon Dioxide Capture and Storage: Special Report of the Intergovernmental Panel on Climate Change*. 25 CM, Cambridge University Press, 2005.

[4] NOAA (National Oceanic and Atmospheric Administration), *National Centers for Environmental Information*, 2015.

[5] WRI (World Resources Institute), *Climate Analysis Indicators Tool (CAIT) 2.0: WRI's climate data explorer.*, 2014.

[6] FAO (Food and Agriculture Organization), *FAOSTAT: Emissions - land use*, 2014.

[7] Global CCS Institute, *The global status of CCS*, 2012.

[8] A. B. Rao and E. S. Rubin, "A technical, economic, and environmental assessment of amine-based CO_2 capture technology for power plant greenhouse gas control," *Environ. Sci. Technol.*, vol. 36, no. 20, pp. 4467–4475, 2002. PMID: 12387425.

[9] D. M. Ruthven, *Principles of adsorption and adsorption processes*. New York : Wiley, 1984.

[10] D. M. Ruthven, S. Farooq, and K. S. Knaebel, *Pressure swing adsorption*. New York, N.Y. : VCH Publishers, 1994.

[11] M. E. Boot-Handford, J. C. Abanades, E. J. Anthony, M. J. Blunt, S. Brandani, N. Mac Dowell, J. R. Fernandez, M.-C. Ferrari, R. Gross, J. P. Hallett, R. S. Haszeldine, P. Heptonstall, A. Lyngfelt, Z. Makuch, E. Mangano, R. T. J. Porter, M. Pourkashanian, G. T. Rochelle, N. Shah, J. G. Yao, and P. S. Fennell, "Carbon capture and storage update," *Energy Environ. Sci.*, vol. 7, pp. 130–189, 2014.

[12] P. Bernardo, E. Drioli, and G. Golemme, "Membrane gas separation: A review/state of the art," *Ind. Eng. Chem. Res.*, vol. 48, no. 10, pp. 4638–4663, 2009.

[13] X. Hu, S. Brandani, A. I. Benin, and R. R. Willis, "Development of a semiautomated zero length column technique for carbon capture applications: Rapid capacity ranking of novel adsorbents," *Ind. Eng. Chem. Res.*, 2015.

[14] M. M. Hossain and H. I. de Lasa, "Chemical-looping combustion (clc) for inherent separationsa review," *Chemical Engineering Science*, vol. 63, no. 18, pp. 4433 – 4451, 2008.

[15] C. Skarstrom, "Method and apparatus for fractionating gaseous mixtures by adsorption," 1960. US Patent 2,944,627.

[16] K. G. E., *Gas-Adsorption Processes: State of the Art*, ch. 9, pp. 145–169.

[17] R. Yang, *Gas Separation by Adsorption Processes*. Chemical Engineering, Imperial College Press, 1997.

[18] S. Choi, J. H. Drese, and C. W. Jones, "Adsorbent materials for carbon dioxide capture from large anthropogenic point sources," *ChemSusChem*, vol. 2, no. 9, pp. 796–854, 2009.

[19] R. V. Siriwardane, M.-S. Shen, E. P. Fisher, and J. A. Poston, "Adsorption of CO_2 on molecular sieves and activated carbon," *Energy Fuels*, vol. 15, no. 2, pp. 279–284, 2001.

[20] S. Sircar, T. Golden, and M. Rao, "Activated carbon for gas separation and storage," *Carbon*, vol. 34, no. 1, pp. 1 – 12, 1996.

[21] H. Li, M. Eddaoudi, M. O'Keeffe, and O. M. Yaghi, "Design and synthesis of an exceptionally stable and highly porous metal-organic framework," *Nature*, vol. 402, pp. 276–279, Nov. 1999.

[22] A. R. Millward and O. M. Yaghi, "Metal organic frameworks with exceptionally high capacity for storage of carbon dioxide at room temperature," *J. Am. Chem. Soc.*, vol. 127, no. 51, pp. 17998–17999, 2005. PMID: 16366539.

[23] I. Langmuir, "The adsorption of gases on plane surfaces of glass, mica and platinum.," *J. Am. Chem. Soc.*, vol. 40, no. 9, pp. 1361–1403, 1918.

[24] P. M. Mathias, R. Kumar, J. D. Moyer, J. M. Schork, S. R. Srinivasan, S. R. Auvil, and O. Talu, "Correlation of multicomponent gas adsorption by the dual-site langmuir model. application to nitrogen/oxygen adsorption on 5a-zeolite," *Ind. Eng. Chem. Res.*, vol. 35, no. 7, pp. 2477–2483, 1996.

[25] D. Do, *Adsorption Analysis: Equilibria and Kinetics*. Chemical Engineer Series, Volume 2, Imperial College Press, 1998.

[26] R. Sips, "On the structure of a catalyst surface," *J. Chem. Phys*, vol. 16, no. 5, pp. 490–495, 1948.

[27] A. L. Myers and J. M. Prausnitz, "Thermodynamics of mixed-gas adsorption.," *AIChE J.*, vol. 11, no. 1, p. 121, 1965.

[28] J. Chen, L. S. Loo, and K. Wang, "An ideal absorbed solution theory (iast) study of adsorption equilibria of binary mixtures of methane and ethane on a templated carbon," *J. Chem. Eng. Data*, vol. 56, no. 4, pp. 1209–1212, 2011.

[29] A. Tarafder and M. Mazzotti, "A method for deriving explicit binary isotherms obeying the ideal adsorbed solution theory," *Chem. Eng. Technol.*, vol. 35, no. 1, pp. 102–108, 2012.

[30] S. Krishnamurthy, V. R. Rao, S. Guntuka, P. Sharratt, R. Haghpanah, A. Rajendran, M. Amanullah, I. A. Karimi, and S. Farooq, "CO_2 capture from dry flue gas by vacuum swing adsorption: A pilot plant study," *AIChE J.*, vol. 60, no. 5, pp. 1830–1842, 2014.

[31] J. Carter and M. Wyszynski, "The pressure swing adsorption drying of compressed air," *Chem. Eng. Sci.*, vol. 38, no. 7, pp. 1093 – 1099, 1983.

[32] N. S. Raghavan and D. M. Ruthven, "Numerical simulation of a fixed-bed adsorption column by the method of orthogonal collocation," *AIChE J.*, vol. 29, no. 6, pp. 922–925, 1983.

[33] E. S. Kikkinides and R. T. Yang, "Effects of bed pressure drop on isothermal and adiabatic adsorber dynamics," *Chem. Eng. Sci.*, vol. 48, no. 9, pp. 1545 – 1555, 1993.

[34] R. Haghpanah, A. Majumder, R. Nilam, A. Rajendran, S. Farooq, I. A. Karimi, and M. Amanullah, "Multiobjective optimization of a four-step adsorption process for post-combustion CO_2 capture via finite volume simulation," *Ind. Eng. Chem. Res.*, vol. 52, no. 11, pp. 4249–4265, 2013.

[35] A. Agarwal, L. T. Biegler, and S. E. Zitney, "A superstructure-based optimal synthesis of PSA cycles for post-combustion CO_2 capture," *AIChE J.*, vol. 56, no. 7, pp. 1813–1828, 2010.

[36] R. J. LeVeque, *Finite Volume Methods for Hyperbolic Problems*. Cambridge University Press, 2002.

[37] B. van Leer, "Towards the ultimate conservative difference scheme. v. a second-order sequel to godunov's method," *J. Comput. Phys.*, vol. 32, no. 1, pp. 101 – 136, 1979.

[38] M. Matuszewski and M. Woods, "Quality guidlines for energy system studies: CO_2 impurity design parameters," Report/Publication NETL/DOE-341/011212, National Energy Technology Laboratory, 2012.

[39] K. Deb, A. Pratap, S. Agarwal, and T. Meyarivan, "A fast and elitist multiobjective genetic algorithm: NSGA − II," *IEEE Trans. Evol. Comput.*, vol. 6, pp. 182–197, Apr 2002.

[40] D. Aaron and C. Tsouris, "Separation of CO_2 from flue gas: A review," *Sep. Sci. Technol.*, vol. 40, no. 1-3, pp. 321–348, 2005.

[41] J. Abanades, B. Arias, A. Lyngfelt, T. Mattisson, D. Wiley, H. Li, M. Ho, E. Mangano, and S. Brandani, "Emerging CO_2 capture systems," *Int. J. Greenh. Gas Control*, 2015.

[42] P. Xiao, J. Zhang, P. Webley, G. Li, R. Singh, and R. Todd, "Capture of CO_2 from flue gas streams with zeolite 13X by vacuum-pressure swing adsorption," *Adsorption*, vol. 14, no. 4-5, pp. 575–582, 2008.

[43] R. Haghpanah, R. Nilam, A. Rajendran, S. Farooq, and I. A. Karimi, "Cycle synthesis and optimization of a VSA process for postcombustion CO_2 capture," *AIChE J.*, vol. 59, no. 12, pp. 4735–4748, 2013.

[44] D. Britt, H. Furukawa, B. Wang, T. G. Glover, and O. M. Yaghi, "Highly efficient separation of carbon dioxide by a metal-organic framework replete with open metal sites," *Proc. Natl. Acad. Sci. U.S.A.*, vol. 106, no. 49, pp. 20637–20640, 2009.

[45] Z. Zhang, Z.-Z. Yao, S. Xiang, and B. Chen, "Perspective of microporous metal-organic frameworks for CO_2 capture and separation," *Energy Environ. Sci.*, vol. 7, pp. 2868–2899, 2014.

[46] P. J. Harlick and F. H. Tezel, "An experimental adsorbent screening study for CO_2 removal from N_2," *Micropor. Mesopor. Mat*, vol. 76, no. 13, pp. 71 – 79, 2004.

[47] F. Notaro, J. Mullhaupt, F. Leavitt, and M. Ackley, "Adsorption process and system using multilayer adsorbent beds," Sept. 22 1998. US Patent 5,810,909.

[48] M. Ackley, A. Stewart, G. Henzler, F. Leavitt, F. Notaro, and M. Kane, "PSA apparatus and process using adsorbent mixtures," Feb. 22 2000. US Patent 6,027,548.

[49] S. U. Rege and R. T. Yang, "A simple parameter for selecting an adsorbent for gas separation by pressure swing adsorption," *Sep. Sci. Technol.*, vol. 36, no. 15, pp. 3355–3365, 2001.

[50] K. S. Knaebel and F. B. Hill, "Pressure swing adsorption: Development of an equilibrium theory for gas separations," *Chem. Eng. Sci.*, vol. 40, no. 12, pp. 2351 – 2360, 1985.

[51] J. C. Kayser and K. S. Knaebel, "Pressure swing adsorption: Development of an equilibrium theory for binary gas mixtures with nonlinear isotherms," *Chem. Eng. Sci.*, vol. 44, no. 1, pp. 1 – 8, 1989.

[52] B. J. Maring and P. A. Webley, "A new simplified pressure/vacuum swing adsorption model for rapid adsorbent screening for CO_2 capture applications," *Int. J. Greenh. Gas Control*, vol. 15, no. 0, pp. 16 – 31, 2013.

[53] A. O. Yazaydin, R. Q. Snurr, T.-H. Park, K. Koh, J. Liu, M. D. LeVan, A. I. Benin, P. Jakubczak, M. Lanuza, D. B. Galloway, J. J. Low, and R. R. Willis, "Screening of metal-organic frameworks for carbon dioxide capture from flue gas using a combined experimental and modeling approach," *Journal of the American Chemical Society*, vol. 131, no. 51, pp. 18198–18199, 2009. PMID: 19954193.

[54] L.-C. Lin, A. H. Berger, R. L. Martin, J. Kim, J. A. Swisher, K. Jariwala, C. H. Rycroft, A. S. Bhown, M. W. Deem, M. Haranczyk, and B. Smit, "In silico screening of carbon-capture materials," *Nat Mater*, vol. 11, pp. 633–641, July 2012.

[55] K. S. Knaebel, "For your next separation consider adsorption," *Chem. Eng. (New York)*, vol. 102, p. 92, 11 1995.

[56] A. D. Wiersum, J.-S. Chang, C. Serre, and P. L. Llewellyn, "An adsorbent performance indicator as a first step evaluation of novel sorbents for gas separations: Application to metal organic frameworks," *Langmuir*, vol. 29, no. 10, pp. 3301–3309, 2013.

[57] J. Zhang and P. A. Webley, "Cycle development and design for CO_2 capture from flue gas by vacuum swing adsorption," *Environ. Sci. Technol.*, vol. 42, no. 2, pp. 563–569, 2008.

[58] M. Radosz, X. Hu, K. Krutkramelis, and Y. Shen, "Flue-gas carbon capture on carbonaceous sorbents: Toward a low-cost multifunctional carbon filter for "green" energy producers," *Ind. Eng. Chem. Res.*, vol. 47, no. 10, pp. 3783–3794, 2008.

[59] S. Xiang, Y. He, Z. Zhang, H. Wu, W. Zhou, R. Krishna, and B. Chen, "Microporous metal-organic framework with potential for carbon dioxide capture at ambient conditions," *Nat. Commun.*, vol. 3, pp. 954–, July 2012.

[60] S. Sircar, "Pressure swing adsorption," *Ind. Eng. Chem. Res.*, vol. 41, no. 6, pp. 1389–1392, 2002.

[61] National Energy Technology Laboratory, *DOE/NETL Advanced carbon dioxide capture R&D program: Technology update*, 2013.

[62] A. Rajendran, V. Kariwala, and S. Farooq, "Correction procedures for extra-column effects in dynamic column breakthrough experiments," *Chem. Eng. Sci.*, vol. 63, no. 10, pp. 2696 – 2706, 2008.

[63] N. Casas, J. Schell, R. Pini, and M. Mazzotti, "Fixed bed adsorption of CO_2/H_2 mixtures on activated carbon: experiments and modeling," *Adsorption*, vol. 18, no. 2, pp. 143–161, 2012.

Appendix A

Pure component adsorption data on Zeolite 13X and TDA-AMS-19

A.1 CO_2 on Zeolite 13X

25 °C		50 °C		75 °C		120 °C	
p_{CO_2} [bar]	q_{CO_2} [mol kg^{-1}]	p_{CO_2} [bar]	q_{CO_2} [mol kg^{-1}]	p_{CO_2} [bar]	q_{CO_2} [mol kg^{-1}]	p_{CO_2} [bar]	q_{CO_2} [mol kg^{-1}]
0.05	2.59	0.07	1.96	0.06	1.27	0.05	0.34
0.08	3.20	0.14	2.53	0.08	1.51	0.09	0.52
0.13	3.44	0.21	2.86	0.11	1.71	0.11	0.65
0.22	3.78	0.32	3.14	0.15	1.91	0.15	0.80
0.33	4.03	0.45	3.38	0.23	2.23	0.22	1.02
0.44	4.20	0.57	3.53	0.35	2.47	0.32	1.25
0.58	4.36	0.69	3.65	0.41	2.62	0.41	1.41
0.73	4.48	0.88	3.82	0.59	2.91	0.57	1.65
0.92	4.61	1.04	3.92	0.71	3.06	0.76	1.86
1.06	4.68			0.90	3.24	0.93	2.02
				1.05	3.35	1.08	2.14

Table A.1: Experimental equilibrium data for CO_2 on Zeolite 13X at 25 °C, 50 °C, 75 °C and 120 °C.

A.2 N_2 on Zeolite 13X

25 °C		50 °C		75 °C		120 °C	
p_{CO_2} [bar]	q_{CO_2} [mol kg^{-1}]	p_{CO_2} [bar]	q_{CO_2} [mol kg^{-1}]	p_{CO_2} [bar]	q_{CO_2} [mol kg^{-1}]	p_{CO_2} [bar]	q_{CO_2} [mol kg^{-1}]
0.02	0.003	0.02	0.002	0.02	0.005	0.02	0.009
0.05	0.139	0.09	0.016	0.08	0.011	0.08	0.013
0.08	0.024	0.20	0.038	0.18	0.022	0.21	0.021
0.23	0.081	0.39	0.069	0.36	0.043	0.39	0.030
0.69	0.228	0.57	0.103	0.55	0.064	0.57	0.034
1.02	0.343	0.74	0.136	0.72	0.085	0.75	0.045
		0.90	0.168	0.92	0.102	0.91	0.054
		1.04	0.185	1.06	0.121	1.05	0.063

Table A.2: Experimental equilibrium data for N_2 on Zeolite 13X at 25 °C, 50 °C, 75 °C and 120 °C.

A.3 CO_2 on TDA-AMS-19

180 °C		240 °C		300 °C	
p_{CO_2} [psia]	q_{CO_2} [mol kg^{-1}]	p_{CO_2} [psia]	q_{CO_2} [mol kg^{-1}]	p_{CO_2} [psia]	q_{CO_2} [mol kg^{-1}]
31.20	0.46	31.20	0.37	31.20	0.31
51.20	0.75	51.20	0.53	51.20	0.40
62.40	0.63	62.40	0.48	62.40	0.38
102.40	1.13	102.40	0.77	102.40	0.53
124.80	1.32	256.01	2.13	204.80	1.09
204.80	1.77			256.01	1.75
306.01	3.15				
500.00	4.28				
600.00	4.58				

Table A.3: Experimental equilibrium data for CO_2 on AMS-19 at 180 °C, 240 °C and 300 °C.